Sorption enhanced Methanation of Carbon Dioxide

Experimental research of nickel modified zeolites for sorption enhanced CO_2 methanation

By

M.H. Azad

in partial fulfilment of the requirements for the degree of

Master of Science

in Chemical Engineering

at the Delft University of Technology,

to be defended publicly on Wensday, May 6, 2020 at 03:00 PM.

Student number:	4605349
Supervisor:	L. Wei,
	Dr. W.G. Haije,
	Prof. dr. ir. W. de Jong
Thesis committee:	Prof. dr. ir. W. de Jong,
	Dr. W.G. Haije,
	Dr. M.A. van der Veen

This thesis is confidential and cannot be made public until May 6, 2020.

An electronic version of this thesis is available at http://repository.tudelft.nl/.

TU Delft

Abstract

Searching for better ways to store the excess renewable energy at large scale, the topic regarding sorption enhanced methanation of CO_2 is researched, pushing the Sabatier reaction over the theoretical equilibrium by means of different water-absorbing zeolites. Till now zeolites and catalyst were mixed separately in the reactor for sorption enhancement. In this thesis, the focus is on impregnating the catalyst on the zeolite as the support, so as to shorten the diffusion path length of water vapour. This material will be called 'the bifunctional material'. This report covers 2 subtopics:

Firstly, do bigger pore sized zeolites improve the sorption enhanced CO_2 methanation?
An appropriate zeolite is searched, resulting in just one zeolite found from the 237, namely the zeolite L. Thereafter, the zeolite L, 13X and 5A zeolites, were impregnated with nickel citrate or nickel nitrate. These bifunctional materials are characterized with the XRD, SEM/EDX and H_2-TPR. In addition, two distinct tests in a fixed bed Sabatier setup were executed: The activity and sorption enhanced methanation tests.
Overall, the results show that the nickel impregnated zeolite L activity is between impregnated 13X and the 5A activity (13X < L < 5A). The sorption enhanced test reveals that impregnated 13X and 5A did have sorption enhancement but not for impregnated zeolite L.

Secondly, how do cleaned bifunctional materials affect the activity compared to regular bifunctional material from evaporation impregnation? Here, the influence of washing on the nickel loading is examined with SEM/EDX. Thereafter, the activity test shows the effect of cleaning on the activity. Finally, the activity of various bifunctional samples (zeolite supports) are compared with reference samples (impregnated Al_2O_3 supports), based on comparable support's pore structure.
The results show the following:
Increasing the amount of washing did not have a noticeable effect on the nickel loading. Just by changing the impregnation method from evaporative impregnation method to filtered impregnation method without additional washing (1,2,3,4 or 5x) is sufficient to prepare clean bifunctional material, containing only little precipitated salt precursor material.
Furthermore, by comparing regular and cleaned bifunctional material per zeolite, reveals that the 5A is impregnated primarily on the outside surface of the zeolite followed by L and 13X (nickel on the outside surface: 13X = 51.3%, L =58.1% & 5A = 84.9%).
The activity test displays that the effective activity (conversion per gram nickel catalyst) of cleaned impregnated 13X and 5A are the highest in H_2 conversion. This makes it interesting for further research since separation enhancement of the Sabatier reaction reduces byproduct formation (CO) to a very large extent.
The activity test comparing bifunctional samples with reference samples result that, supports with similar-looking pore structures do not lead to comparable activity.

Acknowledgements

First of all, I would like to thank my supervisors. Liangyuan Wei helping me especially with the experimental section. I will never forget the struggles opening the autoclave together on the evening of the Chinese mid-autumn festival. Wim Haije for guiding me how proper research has to be carried out and having to hear the most valuable sentence which I will practice upon till in alive: ' Think, rethink if you still can't solve it then come and discuss.'

I would like to thank Wiebren de Jong to give me the opportunity to be a part of his research group and for conducting TPR measurements in the University of Groningen, a city where I normally never would visit. Also, I would give my thanks to Monique van der Veen to be a part of my thesis committee.

Finally, I would like to thank the technician and the PhD'ers/PostDocs in the Process and Energy department providing the equipment, services and advice. Having an inspiring environment with colleagues who are always open to talk stimulated me in my work.

Moreover many accompanied me through my school carrier. Firstly, my HBO-bachelor group: Haci Fatih, Mohammed, Kubilay, Floda en Botan. We really had a great time during classes and made the food places near our school and mosques temporarily wealthy.

Secondly, my friends made at TUDelft. I really enjoyed the struggling time together, particularly during the bridging program when the stakes were high.

The last group are my employers, who gave me the financial means to pay my education and provide for my family. Marcel van Heusden who employed me at Blokker and gave opportunities to grow my social skills and work ethics. Jorn van Putten, after completing my internship gave me a position at OCI. My first step as an engineer. Sowande Boksteen my current employer, even though I did not have a master degree in my pocket yet, he employed me as an engineer and guides me to make the next great leap in my career.

My family: my sisters and my mother. I would like to thank them in their support and care, especially after our father passed away a decade ago.

Finally, I would thank and praise Allah (God) for this experience once of a lifetime. Without you, I would not be here where I am today.

Hamza Azad

Delft, April 10, 2020

Contents

List of abbreviations

13X	Zeolite 13X
5A	Zeolite 5A
BM	Bifunctional Material
BOG	Boggsite
BPS-zeolite	Bigger Pore Size zeolite
BSE	BackScattered Electron
EDX	Energy-dispersive X-ray spectroscopy
EIM	Evaporative Impregnation Method
EON	ECR-1 one
FAU	Faujasite
Micro- GC	Micro Gas Chromatography
FIM	Filtered Impregnation Method
LES	Largescale Energy Storage
LTA	Linde Type A
LTL	Linde Type L
MAZ	Mazzite
MEI	ZSM-18 eighteen
MOZ	ZSM-10 One-Zero
MSE	MCM-68 Sixty-Eight
Ni-Cit	Nickel Citrate
Ni-Nit	Nickel Nitrate
OFF	Offretite
SE	Secondary Electron
SEM	Scanning Electron Microscopy
SES	Small-scale Energy Storages
SNG	Synthesized Natural Gas
TEC	Theoretical Equilibrium Conversion
TCD	Thermal Conductivity Detector
TPR	Temperature Programmed Reduction
XRD	X-Ray Diffraction
IZA	International Zeolite Association
PV	photovoltaic

List of symbols

Symbols	Description	Units
T	Temperature	°C
k	Thermal conductivity	W/°C∗m
P	Pressure	bar
H	Enthalpy	kJ/mol
U	Voltage	V
t	Time	min
λ	wavelength	Å
d	interatomic distance	Å
θ	angle	°
E	Energy	keV
v	the emitted frequency	Hz (s^{-1})
h	Planck constant	eV*s
R	Rydberg constant	m^{-1}
c	Speed of light	m/s
$\dot{V}$	Flowrate	ml/min
S	Selectivity	%
X	Conversion	%

List of Figures

List of tables

1. Introduction

On a global scale, the demand for energy has grown significantly in the last century by 8.5 times as illustrated in figure 1.1. The increase is positively correlated by exponential population growth, a higher standard of living and the progressively increasing life expectancy and so on taking place in the same time frame. These gradual changes are the consequence of better-improved health care, sanitation, quality of life and the launch of the fertilizer industry in the last century. [2][3].

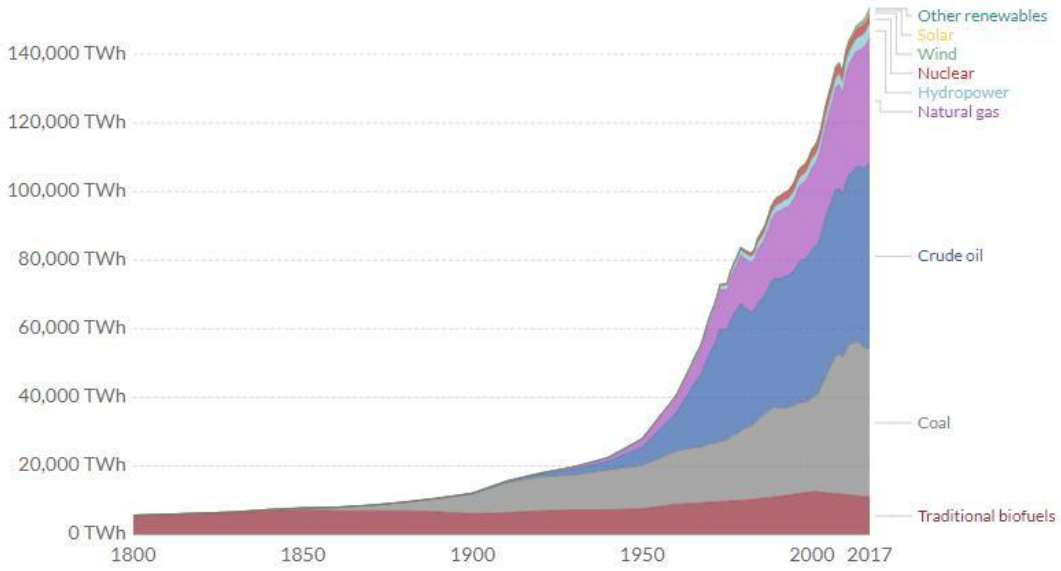

Figure 1.1: The global primary energy demand increased between 1800 and 2017[4][5][6].

In this context, it is expected that the energy demand will increase inevitable. A higher life expectancy and higher living standard will become more common within economic growth driven countries like China and India [7]. Moreover, the global population will grow further to an estimated 8.5 billion in 2030 and 9.7 billion in 2100[1]. However, the current energy supplies consisting primarily of fossil fuels are depleting and polluting. Thus, avoiding or dampening the upcoming energy crisis, investigations are done heavily within industry and academia.

1.1. Current energy supply

Since the industrial revolution, the primary energy source was fossil fuels (88.8%) as displayed in figure 1.1. Alongside fossil fuels, renewable energy supplied in smaller quantities to our societies (~10%). This energy is characterized by it continuously replenishing nature till the source (In this respect the sun) is there. Typically, it is furnished by the sun's radiation, influencing the weather (blowing wind, UV-radiation etc.) thereby forming thermal and photovoltaic (PV) solar energy which is converted in electricity by means of solar panels, wind turbines etc.[8] Unfortunately, the current energy supply relying mainly on fossil fuels is not sustainable for future societies due to their characteristic limitations.

[1] Social and natural counteracting forces, like lower fertility rates and increased natural disasters are considered within the estimations

1.1.1. Limitations to fossil fuel

Fossil fuels have 2 important drawbacks. Firstly, the fossil fuels are depleting. These fuels are the accumulation of millions of years which will be consumed in a couple of centuries by the current heavily relying societies.

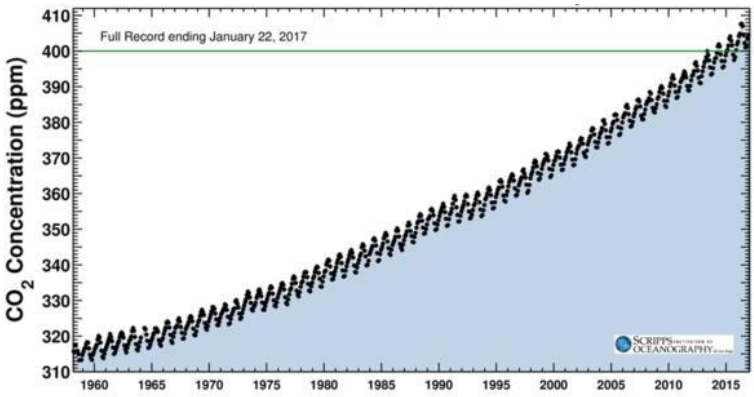

Figure 1.2: The global carbon dioxide concentration in the atmosphere has increased from 316 to 406 ppm within the past 60 years. [9]

Secondly, fossil fuels produce emissions, especially greenhouse gasses, like CO_2. Through the last decades, CO_2 has accumulated in the atmosphere up till 406 ppm as seen in figure 1.2. This causes increases flood, droughts: the so-called greenhouse effect and climate change. Moreover, as the permafrost is melting, more soil with organic material is been available to broken down by microorganisms. This facilitates in additional CO_2 emission, worsening the greenhouse effect even more. Therefore, under the Paris agreement, 196 parties agreed to reach Net-Zero Emissions[2] by 2050. To sum up, fossil fuels are unattractive to become the main energy supplier as anno 2019.

1.1.2. Limitations to renewable energy

Renewable energy has only been limited penetrated in the economy until the past decades, even though it has an advantage over fossil fuels by not producing emissions and replenishes continuously. This is caused by a *mismatch between energy supply and demand.* The industry demands approximately the same throughout the whole day whereas the domestic demand fluctuates considerably by the transitioning through day and night. On the other hand, the energy supply has a greater impact due to the intermittent nature of renewables, like solar and wind, as shown in figure 1.3 [10].

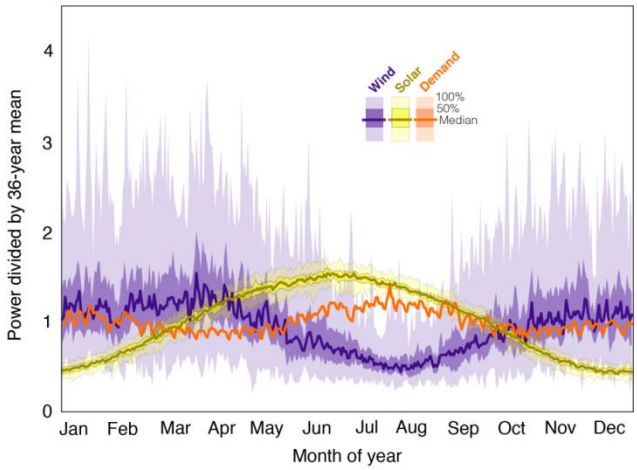

Figure 1.3:: The yearly variability of the energy demand (Red), wind (Blue) and solar energy supply (Yellow) in the United States (industrial & domestic) over a period of 36 years. [11]

The definition of the intermittent nature is:' Some periods of a day or span of months (seasonal inefficiencies), no or insufficient energy is produced to meet the dynamic demand and vice versa', also displayed seen in 1.3**Fout! Verwijzingsbron niet gevonden.** and 1.4.

It seems renewable energy to be promising due to the *short replenish period* and *no pollution advances the greenhouse effect*.

To sum up, the heavily relying fossil fuels should be replaced by sustainable renewable energy supplies by the comparison between the limitations of renewable energy and fossil fuels. This introduces a technical challenge, bridging the dynamic mismatch between energy supply and demand, namely the intermitted nature of renewables.

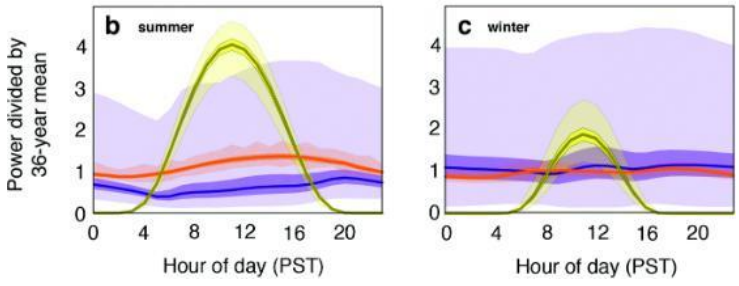

Figure 1.4: The daily variability of the energy demand (Red), wind (Blue) and solar energy supply (Yellow) in the United States (industrial & domestic) over a period of 36 years [11].

[2] Net-Zero Emissions: The produced greenhouse gas by humans is balanced by the removal of the same amounts. This is achieved by reduction as much as possible of emissions sources like transportations. The remaining is balanced by investing CO2 consumers (i.e. trees) and carbon capture

1.2. Large scale energy storage

As a solution bridging the gap regarding the intermittent nature of renewables as mentioned in section 1.1.2, is the usage of energy storage. Energy storages capture the available excess renewable energy (some mentioned in figure 1.5) for later use by converting it back to electricity when the demand exceeds the renewable energy supply. Broadly, two types of storages could be distinguished, Small-scale Energy Storages (SES) like batteries and flywheels for daily intermittencies and Large-scale Energy Storages (LES), for example, pumped storages bridging seasonal inefficiencies as displayed in figure 1.5. Given the presence of seasonal inefficiencies described in section 1.1.2. implies that LES is more suitable[10] [11].

The main requirements for the LES are: Storage at large scales to supply large inhabitants, an energy storage over a prolonged period and the ease of converting back to electricity. It is clear from figure 1.5 that chemical storages (powering 3500-3.5 mil Dutch households/yearly) are more favourable compared to non-chemically storages (max 3500 Dutch households/month) [12]. The two mentioned chemicals for storage are hydrogen and methane/Synthesized Natural Gas (SNG). Both are easily converted back to electricity through SNG combustion and in hydrogen fuel cells, as seen in equations 1.1 and 1.2.

$$CH_4 + 2\,O_2 \rightleftharpoons CO_2 + 2\,H_2O \qquad \Delta H = -889\ kJ\ mol^{-1} \quad (1.1)$$

$$2H_2 + 2\,O_2 \rightleftharpoons 2\,H_2O \qquad \Delta H = -186\ kJ\ mol^{-1} \quad (1.2)$$

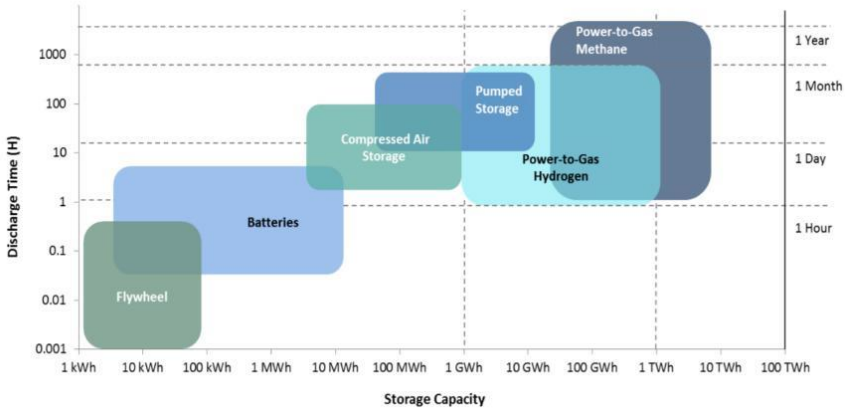

Figure 1. 5: Types of LES describing their characteristic ranges of discharge time and storage capacity [13]

Conclusively, the choice between hydrogen and SNG for the most promising (energy-dense) chemical is made based on 3 of the most important criteria:

1. **The large gravimetric energy density (specific energy)**

Overall, the gravimetric density of methane (55.6 MJ/kg) is relatively larger compared to the most conventionally used chemical like methanol and gasoline (19.7 and 46.4 MJ/kg) as shown in figure 1.6. However, hydrogen with a respectable value of 142 MJ/kg exceeds any other chemical. Hence, making hydrogen more favourable based on gravimetric density.

2. **Large volumetric energy density**

The volumetric energy densities both hydrogen and SNG, are very low by being in a gaseous phase at ambient conditions as shown in figure 1.6. Therefore, compressing and cooling is required for a large-scale store for both chemicals. Nevertheless, for feasible storage at a volumetric density of 10 MJ/L, hydrogen should be compressed to 700 bars, whereas SNG requires compression of 250 bar.

To maintain these extreme pressures for hydrogen storage, huge amounts of energy is demanded. Also, it lowers the exergy by the associated heat loss, generated by the high pressures. Thus, makes hydrogen energetically less favourable.

3. **Ease of distribution**

SNG has a big advantage compared to hydrogen regarding distribution. Since the natural gas transportation network already exists, no major new investments are needed. On the other hand, a hydrogen transportation network is still in their beginning phases

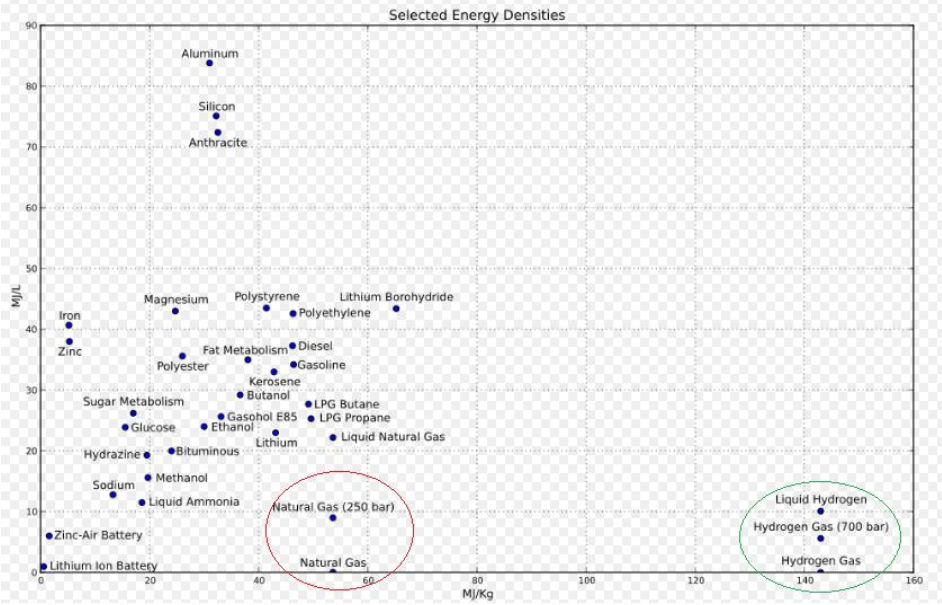

Figure 1.6: Energy-dense chemicals with their corresponding gravimetric and volumetric energy densities. The circles are the prospective chemicals as LES [13]

In other words, SNG has many favourable aspects as LES. The gravimetric energy density is relatively large, it does not require large amounts of compression to reach higher volumetric energy densities and the distinguishing advantage is the ease of distribution which potentially stimulates to be used more widely by industry and public in the well-developed gas grid and distribution of the Netherlands.

1.3. Thesis scope

To use the existing NG-infrastructure, the SNG needs to meet some strict product requirements. According to figure 1.7, a minimum methane purity of 94 mole% is required. However, the methane-producing reaction, the **Sabatier reaction (CO_2 methanation)** as seen in equation 1.3, is in equilibrium [14].

$$CO_2 + 4\,H_2 \rightleftharpoons CH_4 + 2\,H_2O \qquad \Delta H = -165\ kj\ mol^{-1} \quad (1.3)$$

This indicates that the full conversion of the reaction mixture is not reached (80% equilibrium conversion). Further gas-gas separation is needed to realize the product specification.

Component	Typical Analysis (mole %)	Range (mole %)
Methane	93.9	87.0 - 97.0
Ethane	4.2	1.5 - 9.0
Propane	0.3	0.1 - 1.5
Isobutane	0.03	0.01 - 0.3
n-Butane	0.03	0.01 - 0.3
Isopentane	0.01	trace - 0.04
n-Pentane	0.01	trace - 0.04
Hexane and higher	0.01	trace - 0.06
Nitrogen	1.0	0.2 - 5.5
Carbon Dioxide	0.5	0.05 - 1.0
Oxygen	0.01	trace - 0.1
Hydrogen	trace	trace - 0.02

Figure 1.7: The typical composition for commercial natural gas with the additional allowable ranges of impurities [15]

Since the downstream separation requires the largest amount of energy, a potentially viable way is, to use the Lé Chatelier principle which changes the equilibrium by external disturbances like, pressure, temperature or concentration [16]. This principle is applied to the Sabatier reaction by selectively removing water from the product side, thereby creating an imbalance shifting the equilibrium to the right. Thus, more methane is produced, and less byproduct (H_2O) and reactants (CO_2 & H_2) are present in the output composition[46].
In connection with the selective water removal, a water sorbent (the external disturber) is used, like silica gel, molecular sieves (zeolite), MOFs, activated alumina and activated carbon.
Granitsiotis et al concluded among the mentioned water sorbents that, zeolites possess the most favourable characteristics. These are adsorptive capacity at low partial pressures of water (low concentration), selective filtering based on kinetic diameter (water = 2.65 Å) and fast adsorption (physisorption)[22].
Simultaneously, a catalyst is used to increase the rate of the Sabatier reaction. For the CO_2 methanation, metals from the VIIb groups are examined [47]. Berg et al summarized that nickel metals are the most ideal catalyst since these are cheaper, readily available and result in high activities [14]. Thus, the presence of an appropriate zeolite and the nickel catalyst will push the reaction to reach its full conversion.
The phenomenon of simultaneously water sorption as well as catalysts in a reactor vessel is therefore called the **Sorption Enhanced Methanation**.

Earlier researcher explored this topic, providing interesting insights:
Walspurger et al. demonstrated near 100% conversions, far above the theoretical equilibrium, by mixing commercial 4A zeolites and nickel catalyst at atmospheric pressures between 250 and 350 °C. In his experiment, the zeolite and catalyst particles were separate in the reactor bed [46].
Granisiotis et al. expanded the experimental study by decreasing the distance between the catalyst and sorbent. The proximity between them played a dominant role in the process performance since activities above the equilibrium curve are reached as the proximity decreases, illustrated in figure 1.8 [22].
In this connection, Granisiotis suggests impregnating the catalyst on the zeolite as the support. This way the synergy of sorption and catalysis could be maximized[22]. The description of an impregnated zeolite is thereby called the **Bifunctional Material (BM)**.
In the follow-up paper, Wei et al. developed BM's with various nickel precursors on commercial zeolites (13X and 5A) by Evaporative Impregnation Method (EIM). It was found that the activity of impregnated 13X outperformed the activity of impregnated 5A. This has to do with the support, requiring bigger pore sizes since pore volume reduction occurs upon impregnation[18].
This study was limited to their zeolite choices. Here, a rigorous exploration for Bigger Pore Sized zeolite (BPS-zeolite) was lacking.
In addition, Berg et al, made detailed images of impregnated 13X and 5A outer surfaces, exposing inhomogeneous distribution of nickel precursor [14]. The contribution of these 'concentrated' precursors is still unclear in the current literature.

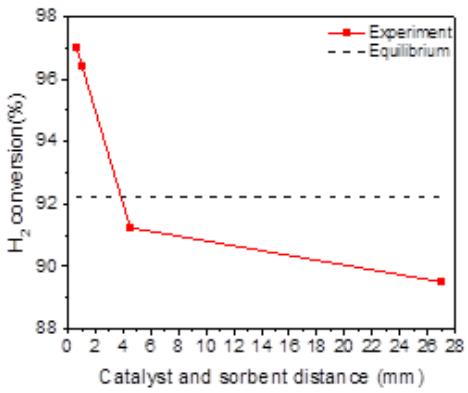

Figure 1.8: Conversion of H_2 at about 270 °C (influence of the diameter of the 4A zeolite particles on the overall H_2 conversion is shown while keeping the diameter of the Ni/Al_2O_3-γ catalyst particle constant at about 270 °C [19].

1.4. Thesis outline

Regarding the sorption enhanced CO_2 methanation, 2 topics will be covered in this thesis:

1. Do bigger pore sized zeolite improve the sorption enhanced CO_2 methanation by having a larger sorption capacity, not hampered by pore volume decrease due to impregnation?
    a. Which BPS-zeolite are easily synthesized and comparable with the 13X and 5A zeolites?
    b. What is the influence of the BPS- zeolite support in the methanation activity?
    c. Does the BPS-zeolite reach conversions higher than the theoretical equilibrium curve in the sorption enhanced experiments?
2. How do cleaned BM's affect the activity?
    a. What is the difference in nickel loading and the effect of the number of washes between cleaned and agglomerated BM?
    b. How does cleaning influence "the effective activity"?
    c. Do the activity curves of cleaned BM correspond with the reference samples based on Al_2O_3 support?

1.5. Report structure

The reports will be structured as follows:

- **Chapter 2**: The employed characterization machinery regarding their fundamental principle and instruments are elaborated.
- **Chapter 3**: The sample preparation, the BPS-zeolite synthesis and the Sabatier setup are explained in great detail in the experimental section.
- **Chapter 4**: The results of the found BPS-zeolite are discussed and compared with the 13X and 5A zeolitic supports. Also, the findings of the sorption enhanced methanation test are assimilated in this chapter.
- **Chapter 5**: The results and discussion of the cleaned BM are compared with the regular BM. Also, these BM are compared with the modified alumina-based support.
- **Chapter 6**: Finally, the findings of this thesis are summarized and recommendations for future research are enumerated.

2. Materials Characterization & Methods

This chapter covers the main equipment's used for this research which are the Sabatier setup, XRD, TPR, SEM and EDX. Per equipment, the purpose, the fundamental principles and the essential part built up are elaborated in dept.

2.1. Sabatier experimental setup

The prepared BMs are tested (activity, selectivity, stability, kinetics etc.) in an inhouse homemade fixed bed setup, called the Sabatier setup as shown in figure 2.1 this setup comprises of 3 main sections: the gas intake, reactor and gas detection.

2.1.1. Reactor section

The desired input composition to the reactor section is supplied by the gas intake section. The reactor is a fixed bed reactor, representing the last reactor in Walspurger et al, heated by an external furnace up to the highest required temperature of 450 °C [46]. The reactor is loaded with the sample between beds of silica beads, for homogenous dispersion of the incoming gasses and preventing small sample particle exiting the isothermal heating zone. Also, pressure indicators are setup before (P1) and after (P2) the reactor measuring pressure drops, a temperature indicator below the bed (T1) measuring the approximate reactor temperature and the build-in furnace temperature controller (TC) regulating the needed heating.

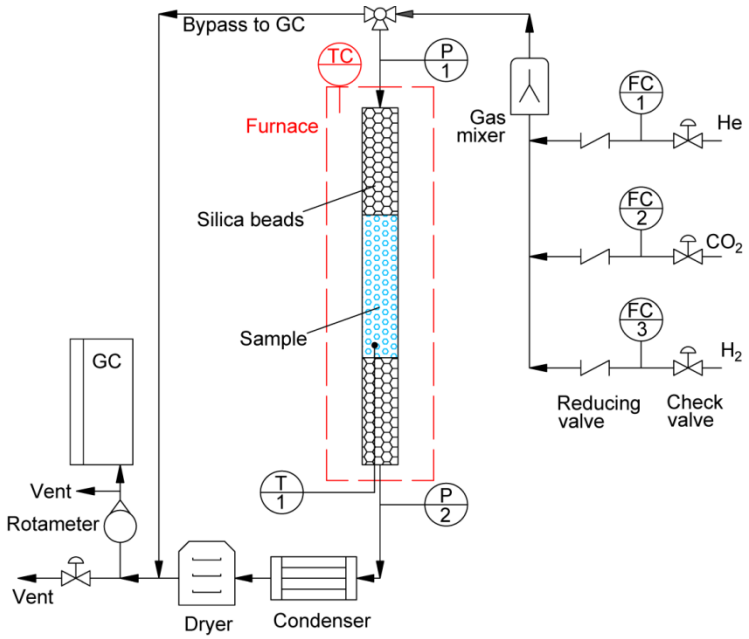

Figure 2. 1: The experimental Sabatier setup. CO_2 and H_2 are diluted in inert gas to the desired feed composition. CO and CH_4 feed streams are also available but not drawn in this specific scheme.

2.1.2. Gas intake section

The gas intake section comprises of 5 parallel positioned gas tanks filled with inert gas, CO_2, H_2, CH_4 and CO. Each is followed with check valves and thereafter a mass flow controller regulating the flowrate. Finally, the desired input gasses are mixed in the Gas mixer, ready to be supplied to the reactor section.

2.1.3. Gas detection section

The final output composition exiting the reactor section is measured by a micro Gas Chromatography (micro-GC). Unfortunately, the product mixture is to warm (>260 °C) and water is produced by the Sabatier reaction as shown in equation 1.3 which the micro-GC (Varian, CP-4900 Micro-GC) cannot handle. Therefore, the product mixture is cooled down in ice water, subsequently dried in silica gel before entering the micro-GC. The CH_4 (2.1), CO selectivity (2.2) and H_2 conversion (2.3) are defined as the following:

$$S_{CH_4} = \frac{n_{CH_{4,in}} - n_{CH_{4,out}}}{n_{CO_{2,in}} - n_{CO_{2,out}}} * 100\% \tag{2.1}$$

$$S_{CO} = \frac{n_{CO_{,in}} - n_{CO_{,out}}}{n_{CO_{2,in}} - n_{CO_{2,out}}} * 100\% \tag{2.2}$$

$$X_{H_2} = \frac{n_{H_{2,in}} - n_{H_{2,out}}}{n_{H_{2,in}}} * 100\% \tag{2.3}$$

Here, $n_{H_{2,in}}$, $n_{CO_{,in}}$, $n_{CO_{2,in}}$ and $n_{CH_{4,in}}$ are the molar flow rates of H_2, CO, CO_2 and CH_4 entering the reactor and $n_{H_{2,out}}$, $n_{CO_{,out}}$, $n_{CO_{2,out}}$ and $n_{CH_{4,out}}$ are the molar flowrates exiting the reactor calculated with the micro-GC results.

2.2. X-Ray powder Diffraction (XRD)

X-Ray Diffraction (XRD) is one of the leading characterization methods for detailed structural atomic determination in material research and development. Fundamentally, X-rays are interacted with crystalline substances, these account for 95% of all solid matter and analyze better than amorphous solids which lack molecular periodicity[20]. This interaction results in many destructive interferences, but some are reflected (diffracted) x-rays under a characteristic angle. These characteristic angles are like a fingerprint of a substance.[55] To realize this the XRD equipment (**Bruker AXS D2 phaser**) is built essentially up in 3 parts: 'The X-ray tube, sampling support and the detector'. The tube (and the detector or sampling support) rotate between 0 and 180° to find characteristic peaks (the measured diffracted x-rays) as shown in figure 2.2.

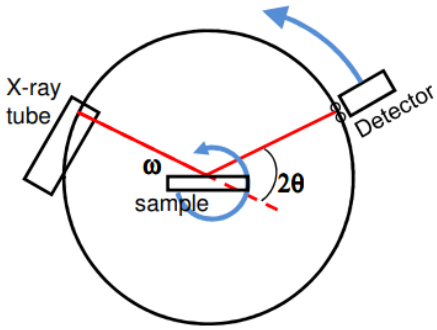

Figure 2. 2: A simplified schematic representation of the XRD. This is built up in the X-ray tube facilitating the X-ray beam, the sample and the X-ray detector.[21]

2.2.1. X-ray production

The X-ray tube, displayed in figure 2.3, produces X-rays only if 4 requirements are met:

Thermionic emission: Electrons need to be emitted by heating an electron source. This process is called thermionic emission.

Acceleration by potential difference: The emitted electrons are accelerated. It is achieved by a positively charged metal (i.e. Anode) opposing the electrons source (i.e. cathode) creating a potential difference (typically voltage 30-150 kV) within the void, exemplified in figure 2.3. The potential difference is transfers as needed to the emitted electron as kinetic energy.

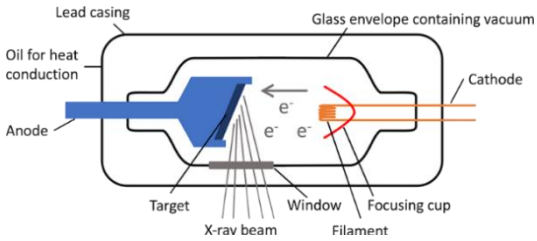

Figure 2.3: The schematic representation of the X-ray tube.[23]

Vacuum: The chamber must be under vacuum, thereby electrons travel freely (between cathode and anode) without colliding with atoms likes nitrogen, oxygen, argon etc.

Electron deacceleration: The emitted electrons put under motions are deaccelerated by striking on the anode metal. Thus, 1% of the kinetic energy is transformed into X-rays and the remaining energy produces heat. The heated anode is therefore continuously cooled.

The emitted X-rays leave the tube through a small window creating a beam illuminating the crystalline substance.

2.2.2. Sampling

The X-ray beam is illuminated on the crystalline substance. As mentioned before the incident x-rays are redirected under specific angles. This phenomenon of the redirecting electromagnetic radiation is called diffraction. Diffraction only applies if the wavelength of the incoming radiation (λ_{xray} =0.1-100 Å) is roughly the same length as a gap, slit or in this case the periodic interatomic distance of the crystalline substances (~0.5-2.5 Å). Bragg's law describes diffraction as given by:

$$n\lambda = 2dsin(\theta) \qquad (2.4)$$

λ is the wavelength (Å), *d* is the interatomic distance between crystal planes (Å), θ is the angle of the diffracted wave (degrees) and *n* is an integer known as the *order* of the diffracted beam as displayed in figure 2.4.
in addition, the sample requires to be grinded well and made flat due to the importance of the characteristic angle.

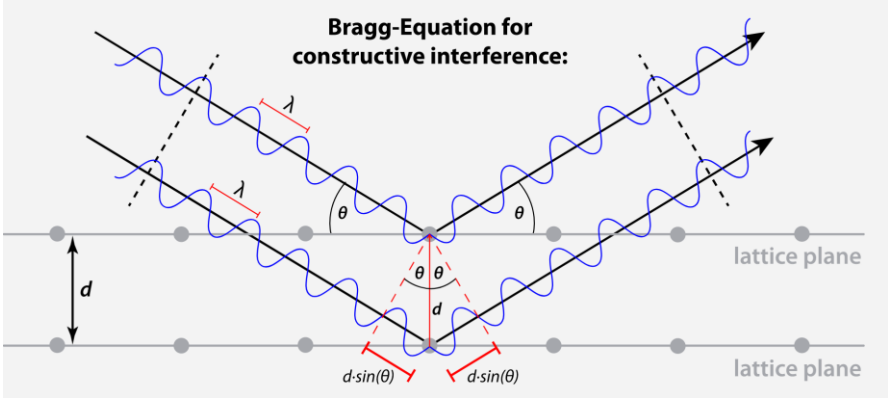

Figure 2.4: diffraction of X-rays in a crystal lattice obeying Bragg's law[44]

2.2.3. Detector

When the incident x-rays are diffracted, obeying Bragg's law, constructive interferences are detected and converted by a detector resulting in a 2θ-intensity plot. Thus, the peaks on different 2θ form the fingerprint of the sample and ready for comparison with reference XRD results for substance identification.[51][52]

2.3. Temperature Programming Reduction (TPR)

Temperature program techniques are studies in the **Micromeritics AutoChem 2910** as a function of temperature in 3 main areas: desorption, oxidation and reduction. The focus lies in reduction whereas desorption and oxidation are omitted from this research [56].
Temperature Program Reduction (TPR) is a characterization technique for finding the most efficient reduction temperatures used for optimal reactor design. This technique is particularly conducted for heterogeneous catalysts, for instance, the metal-based catalyst for ammonia synthesis, being an important backbone for the fertilizer industry.[53]
Here, the procedure is generally carried out by heating linearly under a flowing reducing gas (i.e. H_2) diluted in inert gasses (i.e. Argon) In a U-tube loaded catalyst bed. This reducing gas is consumed at certain temperatures measured by a thermal conductivity detector (TCD) [56].

In a TCD a hot filament is cooled by two separate gas streams. One is pure carrier gas (reference) and the other is column effluent diluted in a carrier gas. Since the streams have different gas compositions, a different rate of cooling is observed. These signals from both streams are compared determining the thermal conductivity [56].
Generally, the carrier gas is a high thermal conductive gas like H_2 or He, increasing the sensitivity of the measurement [45]. N_2 could be used as a carrier gas because it is less costly than He and less dangerous than H_2. But the disadvantage is the lower sensitivity [56].

2.4. Scanning Electron Microscopy (SEM)

The scanning electron microscopy is used for imaging surfaces of solid samples. The specific equipment used is the **JEOL JSM-6010LA** under 2.7 kV. The SEM is comparable with a light microscope but using a focused electron beam for higher magnification and resolution instead of a focusing light beam as shown in figure 2.5.

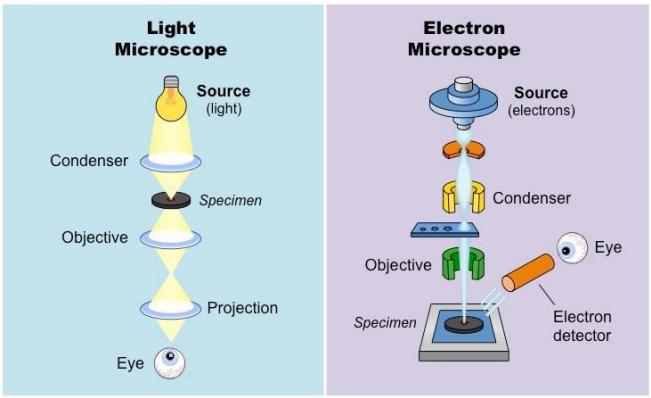

Figure 2.5: Comparison between light microscopy and electron microscopy [43].

The SEM is broken down in 2 parts [54]:

Source: Electron production occurs in the electron gun (source) by thermionic emission, as mentioned in section 2.2.1. Thereafter, the emitted electrons pass through a condenser creating an electric field focusing the electron into the desired beam to illuminate the sample. Typically the electron are accelerated (energized) between 0.2 – 40 keV [54].

Scanning: Various types of signals are emitted by high energetic electrons interacting with the sample as shown in figure 2.6. The main signals are Secondary Electrons (SE), BackScattered Electrons (BSE) and characteristic x-rays of which the latter is interesting for Energy Dispersive X-ray spectrometry (EDX) as discussed in section 2.5. The BSE and SE both display the surface morphology but interact differently with the sample presenting unique information's. For the SE-interaction, the primary electron (electron beam) emits electrons from the outer shell of atoms present on the sample's surface [54].

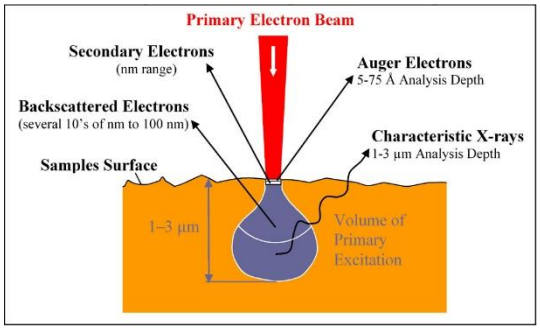

Figure 2.6: A simplified schematic of emitted signals by electron sample interactions [42].

This interaction is surface sensitive displaying images with great resolutions. On the other hand, BSE-interaction redirects the primary electron from the original direction without colliding the nucleus or electrons, making it atomic mass sensitive. Heavier atoms backscatter better leading to lighter and brighter images compared to lighter atoms[14] [41].

The schematic representation of the different interactions is presented in figure 2.7.

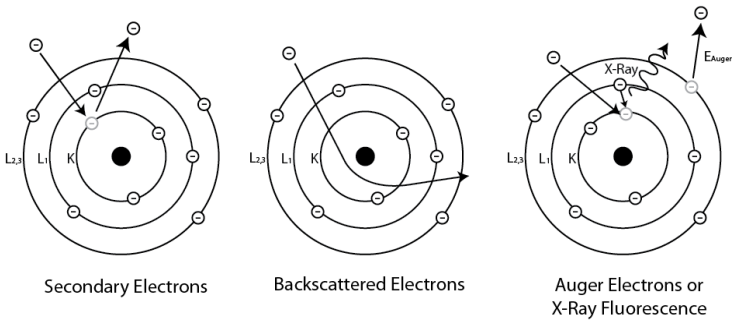

Figure 2.7: Schematic representation of the main interactions between the electron beam and the sample [40].

2.5. Electron dispersive X-ray spectroscopy (EDX)

The EDX is a characterization equipment for atomic number determination of solid material by mean of characteristic X-rays. Typically, the EDX and SEM are build up with the same 2 parts and emit the required x-rays, therefore the **JEOL JSM-6010LA** conducted for the SEM could be used as the EDX with minor adjustments of increasing the voltage up to 20 kV. The EDX measurement could be divided up in two consecutive processes:

Atom excitement: The sample is illuminated by an X-ray beam (20 kV) exciting (K, L or M) electrons from the inner shells to eject out of the atom. This electron-hole creates an instable atom [54].

X-ray generation: To stabilize the atom again, an electron from the outer high energetic shells fills up the vacancy in the lower energetic inner shell. During this, a difference in energy (eq. 2.5) is created which releases x-rays as shown in figure 2.8. ΔE is the difference in energy of the electron in the outer shell compared with inner shell (J), the h is the Planck constant (eV*s) and v is the emitted frequency (Hz =s^{-1}) [39].

$$\Delta E = hv = E_{outer,shell} - E_{innner,shell} \tag{2.5}$$

The frequency of the emitted X-rays is unique to the respective atomic number as displayed in figure 2.9. Mosely's Law derived empirically that the frequency of the emitted x-rays is directly correlated to the atomic number as shown in equation 2.6. v is the frequency of the emitted characteristic x-ray (Hz =s^{-1}), the Z atomic number (-) k_1 and k_2 are constants dependent on the type of line. For the K-alpha lines $k_1 = \sqrt{3\frac{R*c}{4}}$, k_2=1 and L-lines $k_1 = \sqrt{5\frac{R*c}{36}}$, k_2 = 7.4. Rydberg constant being the R and the speed of light the c [37].

$$\sqrt{v} = k_1 * (Z - k_2) \tag{2.6}$$

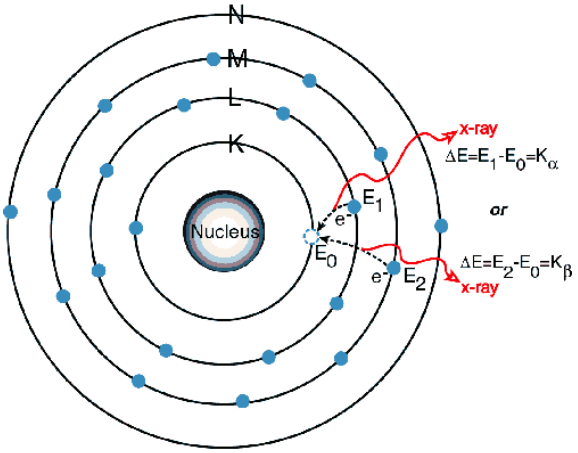

Figure 2.9: The schematic description of x-ray generation [35].

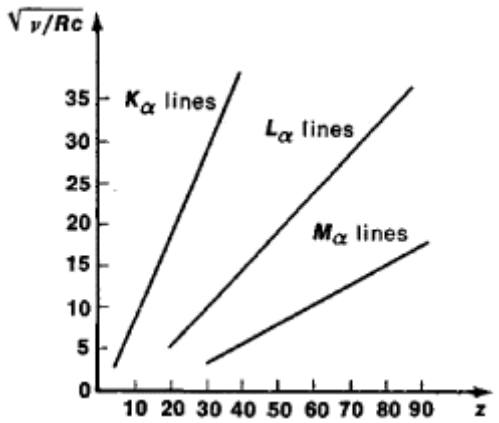

Figure 2. 8: The empirical correlation between the emitted x-ray and the atomic number [24].

3. Experimental section

The experiments carried out are devoted to this chapter. The step-by-step commercial BPS-zeolite investigation and synthesis are covered thoroughly. Thereafter the various sample preparations (zeolitic and Al_2O_3 based) are explained. These samples are tested in the Sabatier setup for which the final section is dedicated.

3.1. BPS-zeolite

For the search of the BPS-zeolite, the zeolite structures of the International Zeolite Association (IZA) is used as the collection of known zeolites. Yearly, new structures are discovered, increasing the databases size (2007=176 [25],2017=237 [26], 2019>237 zeolite structures [27]). The database up till 2019 are acquired but to simplify the search, only the structures recognized in 2017 are used due to the relatively up to date literature for zeolite synthesis and the possibility to purchase it commercially.
In this context, the Faujasite framework (FAU)[3] [4] and the Linde Type A (LTA)[5] zeolite structures are excluded from this exploration due to well-studied research regarding the sorption enhanced methanation [14] [22].

3.1.1. Criteria list & commercial BPS-zeolite inquiry

The main requirement for the new BPS-zeolite is a large limiting pore size. Moreover, the BPS zeolite should be comparable to the 13X and 5A. Therefore, important characteristics should be at least in the same order of magnitude, giving the BPS-zeolite criteria list:

1. **Limiting pore diameter > 6.7 Å**: A zeolite with a pore limiting diameter larger than the 13X is essential for higher activity. [26].
2. **Presence of Al & Si**: The LTA and the FAU frameworks consists of $[SiO_4]^{-4}$ and $[AlO_4]^{-5}$ tetrahedral which are connected by a shared oxygen atom on the sides creating pores and cavities. Hence, other deviant frameworks, like the ITG framework with a Si-Ge combination are excluded.
3. **Si/Al ratio between 1-3**: A similar Si/Al ratio will result in a similar water-zeolite and CO_2-zeolite interactions. A lower Si/Al ratio attracts water due to more negatively charged $[AlO_4]^{-5}$ [17]. Also, a lower Si/Al ratio corresponds to a low acidic material (thus high basic) which attracts the acidic CO_2 more, leading to a higher conversion (activity). The Si/Al ratio is of the 5A and 13X are between 1-3 as found in Appendix A.1.
4. **Inorganic**: The BM requires to reach temperatures up till 450 °C in the Sabatier setup. Since organic materials above 300 °C decompose slightly decreasing the zeolite synthesis yield [28], BPS-zeolites possessing organic material will be omitted from the search.
5. **Available for purchase**: If a zeolite with the before mentioned criteria is commercially available, then unnecessary, time-consuming zeolite synthesis will be prevented.

3.1.2. BPS-zeolite inquiry

The initial preferred choice was to purchase a commercial zeolite rather than a time-consuming zeolite synthesis. The IZA organization compiled a list of 66 zeolite supplying companies, which had been enquired regarding the criteria list, mentioned in section 3.1.1 [29]. However, an appropriate commercial zeolite could not be retrieved based on the abovementioned criteria.

Thus, the decision was made to synthesize a new BPS-zeolite. The IZA zeolite structure list of 2017 is used as mentioned in section 3.1.1. From the 237 zeolite structures, 8 were found which meet the BPS-zeolite criteria: **Maz**zite (MAZ), **L**inde **T**ype **L** (LTL), **Bog**gsite (BOG), **E**CR-1 **on**e (EON), ZS**M**-18, **ei**ghteen (MEI), ZS**M**-10 **O**ne-**Z**ero (MOZ), **M**CM-68 **S**ixty-**E**ight (MSE) and **Off**retite (OFF).
From these options, the MOZ and the LTL were less time-consuming and required fewer stages for synthesis compared to the other structures. Unfortunately, the MOZ produces Diquat 1 which is a hazardous intermediate material. Consequently, the MOZ is deemed to be unsuitable for this study [30] [31].

[3] for instance, material with these frameworks are zeolite X and zeolite Y series
[4] Some material with this framework is Zeolite A series and ZK-4, ZK-21 and ZK-22
[5] Zeolite 5A from this zeolite structure

Finally, the zeolite L synthesis with the LTL framework meets the criteria of the BPS-zeolite [32]. Further characteristics of the LTL structure can be found in Appendix A.1.

3.1.3. Generalized zeolite synthesis

Zeolites are formed in volcanic and sedimentary rocks but are also synthesized in laboratories, both following a typical hydrothermal reaction. Hydrothermal synthesis is a crystallization method dissolving strong salt solutions with a low solubility at 100 °C (i.e. Ge, Si, Al & Ga) in a base environment, at elevated temperatures (170-270 °C) with the presence of water [33][34].
Generally, a hydrothermal synthesis is divided into 3 subsequent steps as shown in figure 3.1.

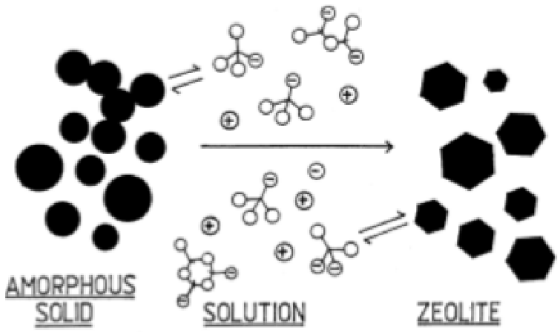

Figure 3.1: The process from amorphous insoluble reactants to the desired zeolite crystal with an intermediate stage being a solution (gel) [34].

First, a gel is formed by dissolving in water amorphous solids, alumina and silica, which are the building blocks of a zeolite:

- Product A: An alumina solution is prepared by dissolving $Al(OH)_3$-powder ($Al(OH)_3$, >99%, Sigma Aldrich) in water in a reflux setup as shown in figure 3.2. The poorly soluble $Al(OH)_3$-powder (solubility (@100 °C) = 0.0001 g/100ml) is forcefully dissolved in a base environment to deprotonate into a potent dissolvable form as shown in equation 3.1.

$$Al(OH)_3\ (s) + 3\ OH^-(aq) \Rightarrow\rightarrow AlO_3{}^-(aq) + 3H_2O\ (l) \qquad (3.1)$$

- Product B: On the contrary, the silica solution was unfeasible to prepare because of the lack of a specialized high-speed mixer (18000 rpm) [32]. Therefore, a commercial silica solution (SiO_2, 40%, Sigma Aldrich) is purchased with a fixed water content.

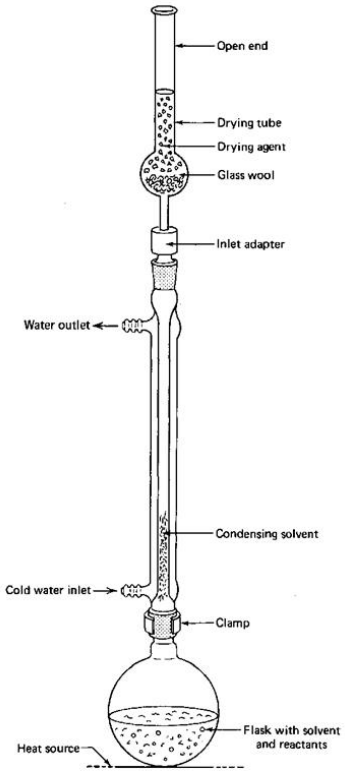

Figure 3.2: Schematic representation of the reflux setup.

Continuing, this gel is transferred into an autoclave (closed vessel reactor) to raising the temperature under pressure above the interested induction temperature. The amorphous materials are converted into the desired crystalline zeolite. Specifically, the zeolite L reaction is as follow in equation 3.2.

$$27\ K_2SiO_4{}^{-2} + 9\ KAlO_4{}^{-4} + 93\ H_2O \rightleftharpoons 54\ K^+ + 144\ OH^- + |K_9{}^+(H_2O)_{21}|[Al_9Si_{27}O_{72}]\text{-LTL} \qquad (3.2)$$

Finally, the zeolite crystals are recovered by filtering, washing and drying [34]. The comprehensive explanation of the hydrothermal zeolite synthesis specific to the zeolite L can be found in Appendix A.2.

3.2. Preparation of Bifunctional Materials (BM)

The all the BM are prepared by impregnating a nickel precursor(1) on a zeolite (2) by a specific impregnation method (3). Here, three variables are given which are altered to produce all the various samples required in this thesis. Moreover, reference samples are made using various non-adsorbing Al_2O_3-based support instead of a zeolite.

3.2.1. General impregnation procedure

The support is grinded in the Retsch ZM 200 at 6000 rpm and sieved out targeting the mesh fraction between 0.212 and 0.500 mm. This procedure is repeated between 8-10 times until 40-55 wt. % of the support with the desired fraction is recovered.
Thereafter this 'sieved out support' is impregnated for 24h with an equivalent of 5 wt.% Ni (w.r.t. the zeolite mass) in the rotary evaporator Vacuum box Hei-VAP from Heidolph or with a mechanical stirrer, depending on the availability. Afterwards, it is dried (depending on the impregnation method if an intermediate step is present as explained in section 3.2.2.1.) overnight in an oven at 100 °C, then calcined into a muffle furnace 3 h at 400 °C with a ramp-up of 2.53 °C/min.

3.2.2. The variables: Supports, precursors and impregnation method

3.2.2.1. Impregnation methods

Evaporative Impregnation Method (EIM): The support is placed in a nickel solution (0.17M) for impregnation, for 24 h at low rotation speed (20 rpm) and room temperature in a rotavapor. Thereafter, the remaining nickel in the solution is precipitated on the support in a rotavapor by evaporating the nickel solution at 50 °C und 100 mbar [33]. Resulting in a support with impregnated and precipitated nickel precursor which agglomerates on the support. **This method is used for all samples except when mentioned otherwise.**

Filtered Impregnation Method (FIM): The support is placed in a nickel solution (0.17M) for impregnation, for 24 h at low rotation speed (20rpm) and room temperature in a rotavapor. Thereafter, the impregnated support is separated from the remaining nickel solution in a Buchner filter. Also, the impregnated support is *washed off with approximate 17 ml deionized water*. Resulting in a support **only** with the dispersed nickel precursor on the surface support.

3.2.2.2. Supports

Al_2O_3-support: Al_2O_3 supports eliminates water sorption from the activity results since it does not contribute as a catalyst nor as a sorbent.
Two types of Al_2O_3-supports are used: commercial Al_2O_3-ɣ (Alpha Aesar, total pore volume = 0.8-1.2 cc/g, surface area = 220-280 m^2/g) and Al_2O_3-α support (Alpha Aesar, total pore volume = 0.54 cc/g, surface area = 0.82 m^2/g).
The main differentiation between these is, that Al_2O_3-ɣ support is porous while the Al_2O_3-α support is non-porous.

Zeolite-support: 2 commercial molecular sieves - zeolite 5A (~2 mm, Sigma Aldrich) and zeolite 13X (1.68-2.38 mm, Sigma Aldrich) - and the synthesized zeolite L with respectively limiting pore sizes of 4.9 Å, 6.7 Å and 8.1 Å, were used in preparing for various BMs by the EIM and FIM impregnation methods. Other characteristics are found in Appendix A.1. all 3 These were grinded to a mesh size = 0.212-0. 500 mm
Furthermore, the zeolite L is produced as a powder which required to have a mesh size between 212-500 mm. Therefore, the zeolite L powder is pelletized as explained in Appendix B.2.2.

3.2.2.3. Precursors

Nickel citrate (Ni-Cit): Nickel Citrate ($Ni(C_6H_5O_7)_2 \cdot .9.8H_2O$, 98%, Sigma Aldrich)

Nickel nitrate (Ni-Nit): Nickel Nitrate ($Ni(NO_3)_2 \cdot .6H_2O$, 99%, Sigma Aldrich)

3.2.3. Multiple washing affecting nickel loading

To observed the relationship between the number of washes and the nickel loading, the BM preparation with the FIM impregnation followed in section 3.2.2.1 is adjusted. Here, multiple washes are introduced before transfer to the Buchner filter.

A wash is conducted in 3 steps in a test tube filled with the BM: 25 ml deionized water is added (1). The filled tube is agitated (20-30 sec) increasing collisions with the agglomerated nickel on the zeolite surface(2). Finally, the excess water is removed (3). These series of steps are repeated up till 5 times, creating 6 samples for the 13X and 5A as shown in table 3.1.

The zeolite L only has one cleaned BM sample (4x washed), due to lack of synthesized material and time constraint. Furthermore, per sample 1 BM following the EIM impregnation is done for comparison. Finally, other possible precursors were excluded since the Ni-Cit is been proven until now to have the highest activity [14].

Support	Precursor	wt% Nickel	impregnation method	times washed (x)					
13X	Ni-Cit	5	EIM	0	-	-	-	-	-
13X	Ni-Cit	5	FIM	0	1	2	3	4	5
5A	Ni-Cit	5	EIM	0	-	-	-	-	-
5A	Ni-Cit	5	FIM	0	1	2	3	4	5
L	Ni-Cit	5	EIM	0	-	-	-	-	-
L	Ni-Cit	5	FIM	-	-	-	-	4	-

Table 3.1: Samples list from incremental washed BM with various supports and impregnation methods.

3.2.4. Al_2O_3 and zeolitic based support

Bifunctional samples (support = zeolite) are compared with reference samples (support= Al_2O_3) ***to observe if similar pore structured supports reproduce similar activities***.

Therefore, the 5 currently researched BM's are paired with various impregnated Al_2O_3 supports, as given in table 3.2:

1st pair: After impregnating the 5A, it is found that the Ni-Cit complex is larger than the openings of the pores, so most of it precipitates on the 5A outer layer. Here, the Al_2O_3-α support has a suitable pore structure, thereby precipitates similarly on the outer surface layer. Both will be treated with EIM.

2nd and 3rd pairs: The Ni-Cit complex has a similar size as the pore openings of the 13X and L. This allows the complex to diffuse into the zeolite structure. The Al_2O_3- ɣ support has a similar pore structure as it is porous. Both will be treated with EIM.

4th and 5th: The support choice is the same as the 2nd and 3rd pair, except for the impregnation method which will be FIM.

All sample preparation follow the general procedure as explained in section 3.2.1.

Pair (#)	Bifunctional samples (zeolite)	Reference samples (Al_2O_3)
1	5%Ni/5A/Cit/EIM	5%Ni/Al_2O_3-α/Cit/EIM
2	5%Ni/13X/Cit/EIM	5%Ni/ Al_2O_3-ɣ/Cit/EIM
3	5%Ni/L/Cit/EIM	
4	5%Ni/13X/Cit/FIM	5%Ni/ Al_2O_3-ɣ/Cit/FIM
5	5%Ni/L/Cit/FIM	

Table 3. 2: The expected comparable pore structured support between bifunctional and reference samples.

3.3. Sabatier setup

For the Sabatier setup, 4 types of tests could be conducted: The activity, kinetic, stability tests and the sorption enhanced methanation. The kinetic and the stability tests are omitted due to time constraint and well research report by D. Berg.

Activity Test: The activity tests are conducted at atmospheric pressure on 0.9 grams of impregnated support placed between 2 beds of silica beads (height=4cm). The nickel oxides on the support are reduced by a total feed flow of 160 ml/min consisting of 6.25% H_2 and 93.75% N_2 at 450 °C for 2h. Subsequently, the CO_2, H_2, CH_4 and CO concentrations of the reaction product were the average value base on GC-measurements for 10 samplings per temperature. The measuring temperatures were at 450,400, 360, 320 and 280 °C and the total feed flow was 200 ml/min consisting of 20% H_2, 5% CO_2, 75% N_2.

Sorption enhanced methanation test: The sorption enhanced methanation reaction are conducted at atmospheric pressure with BM placed between 2 beds of silica beads (height=4 cm). The BM is around 8.4 g which is two times more than mentioned in Walspurger et al[46]. The reason behind this is to extend the water breakthrough measure enough GC-samples during sorption enhancement.
The operation is due to the following: The nickel oxides on the support is **reduced** by a 100 ml/min H_2 for 2h. Thereafter, the BM is cooled down also under 100 ml/min H_2 till the sampling temperature 320, 300, 280 and 260 °C. At the sampling temperature, a feed composition is introduced identical to the final composition of the second reactor mentioned in Walspurger et al (9.9% H_2, 2.5% CO_2, 81.6% CH_4, 6.0% N_2) with a total flowrate of 100 ml/min [46]. The concentration of the reaction product (CO_2, H_2, CH_4 and CO) were measured by a micro-GC with 15 samples per sampling temperature. In between the sampling temperatures, the water in the BM is desorbed by raising the temperature back to 450 °C under 100 ml/min H_2 flow for 2h. The detailed stepwise program is found in Appendix G (figure G.1 and table G.1).

For comparison, the same samples underwent an activity test with similar feed composition and flowrate. The sampling temperature, during the sorption enhanced methanation test, is an average value base of 10 GC-measurements.

4. Results and discussion - BPS-zeolite

The progression of the sorption enhanced methanation research lacked exploration to a Bigger pore sized zeolite, as mentioned in section 1.3. This was found (zeolite L) and synthesized as described in section 3.1.

This chapter proceeds by, confirming 'if' a successful zeolite synthesis has taken place, with various characterizations. Then, the impregnated zeolite L samples are compared with impregnated 13X and 5A through characterizations and distinct tests in the Sabatier setup.

4.1. Characterization Zeolite L

The characterization of the zeolite L is divided up in 4 sections, each using different characterization equipment. The first two parts, the XRD and SEM-analysis, validate the successful synthesis of the zeolite L. Afterwards the EDX-analysis compares the nickel content per zeolite after EIM. Finally, the reduction behaviours of the BM are examined by the TPR-analysis.

4.1.1. XRD analysis

To verify the success of the zeolite L synthesis, the crystalline structure was determined by an in-house XRD. Typically, 4 main peaks at 2θ = 5.5 ^{o}, 19.4^{o}, 22.7^{o}, 28^{o}, 29^{o} and 30.7^{o} are characterized by the zeolite L [36]. These peaks (colour code = blue) are superposition over the XRD pattern result of fresh zeolite L as displayed in figure 4.1.

The results show the presence of all main peaks of the crystalline structure of the zeolite L. Additionally, the main peaks of the reactants, SiO_2 (Yellow) and $Al(OH)_3$ (Red) are examined and it appears to lack some peaks.

In other words, the successful synthesis is confirmed by the presence of the 4 main zeolite L peaks and that the sample has a high purity by the lack of some main reactants peaks.

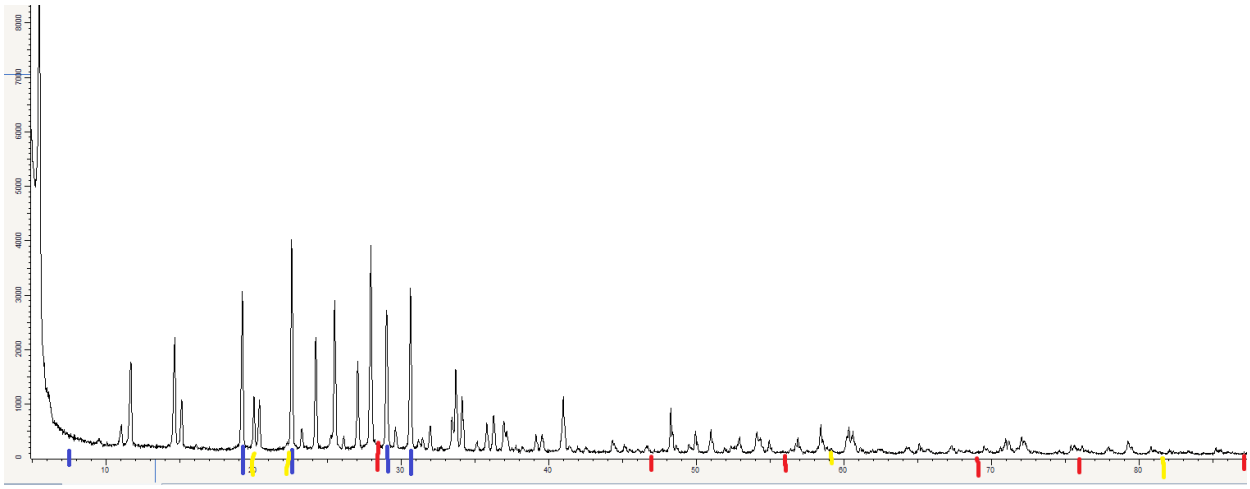

Figure 4.1: The XRD diffractogram of zeolite L, colour-coded 2θ peaks - zeolite L = blue, $Al(OH)_3$ = Yellow, SiO_2 = red. Voltage = 30 kV, Current = 10 mA.

4.1.2. SEM analysis

Zeolite L crystals with a cylindrical shape were observed in the JEOL JSM-6010LA under 2.7 kV as displayed in figures 4.2a-c. This morphology agrees with literature for the given starting gel composition mentioned in Appendix A.2 [32].
The nickel precursor impregnated on the zeolite (before calcination) is noticeable as stains (figure 4.2B-C) compared with the freshly unimpregnated zeolite L (figure 4.2A). Furthermore, no visual difference is noticed by varying the precursor by comparing figures 4.2B and 4.2C. This is expected due to the similar impregnation method, which is the EIM.

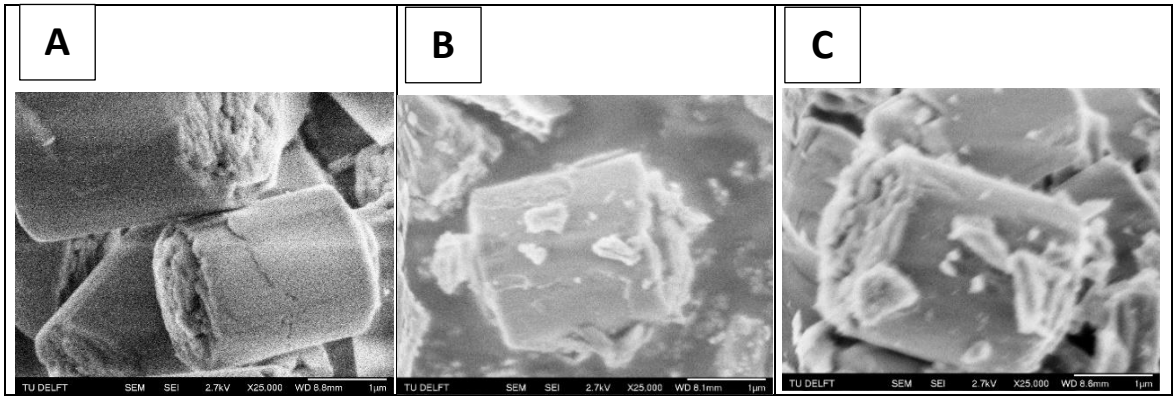

Figure 4.2: SEM images of fresh zeolite L (A), 5%Ni/L/Cit/EIM (B) and 5%Ni/L/Nit/EIM (C)

4.1.3. EDX analysis

Per sample 5 points/area measuring the nickel wt.% in the JEOL JSM-6010LA under an electron beam of 20 kV are averaged before reduction. One representation of one EDX result is shown in figure E.1.
The results for zeolite 5A, 13X and L are shown in Table E.1 (precursor Ni-Nit) and E.2 (precursor Ni-Cit). By comparing 5%Ni/L/Nit/EIM with 5%Ni/L/Cit/EIM similar Ni wt.% are measured.
However, it seems that the precursor choice influences the nickel loading for the 13X and 5A and surprisingly some exceed the 5 wt.% target.
These deviations may be due to inhomogeneous distribution of nickel over the support, having some highly concentrated nickel spot caused during the BM preparation (i.e. varying impregnation times, mass nickel precursor etc.). Also, The EDX examines only the loading on the other surface, disregarding the loading within the zeolite structures.

4.1.4. TPR analysis

For the reduction behaviour of various BM, the TPR is used for characterization. The results of the TPR-profiles of BM per zeolite are shown in figure 4.3. Each BM displays a peak in the range of 300-350 °C. The second peak is at higher temperatures for the 5A and 13X as found between 450-550 °C. This indicates that nickel oxides formation is location dependent[18]. The lower peak range could be corresponding to catalyst reduction outside the pores whereas the peak range at higher temperatures is associated with reduction inside the pores[48, 49, 50].
The second peak of the zeolite L is very small at 420 °C as found in the scaled figure in Appendix F.3. It suggests that most of the precursor is located outside the zeolite L pores, even though the limiting pore diameter is larger than the 5A as found in Appendix A.1. This could indicate that the pores are blocked by the precursor and may inhibit the water adsorption in sorption enhancement experiments.

Moreover, It appears that the thermal conductivity of zeolite L over the whole temperature range is far lower compared to 13X and 5A (fig. 4.3) indicating a small formation of nickel oxides. Figure 4.2b shows the large stain on the L representing large nickel particles. It could be that the inner part of these agglomerated nickel is not reduced, so returning a weaker signal to the TCD.

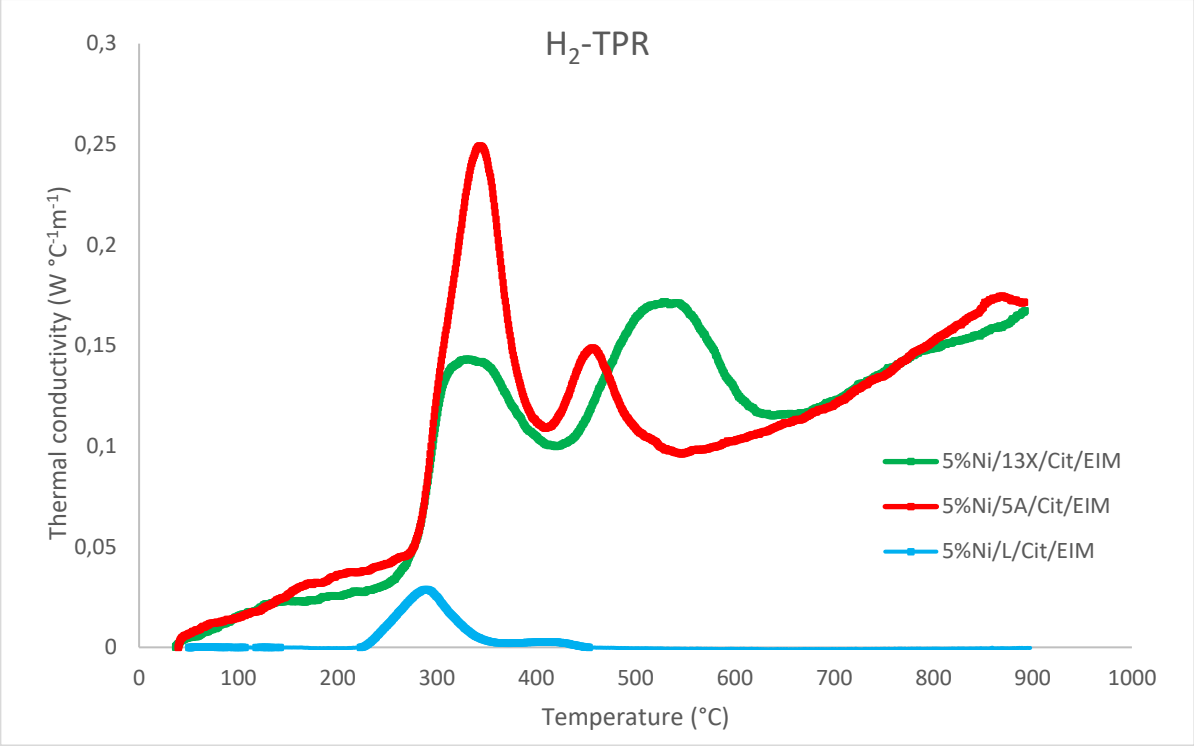

Figure 4.3: H_2-TPR profiles of BM with varying support: 13X (green), 5A (red) & L (blue). Fixed: Impregnation method. Fixed: precursor. Total mass: 0.5 gram. The significantly smaller zeolite L peak is observed. Large stains of nickel particles on the zeolite L are observed from SEM pictures (fig 4.2b), indicating that the inner parts are not reduced.

4.2. Sample performance: Activity and sorption enhanced methanation tests

In the Sabatier setup, two distinct tests are executed to measure the performances. The first is the activity test, measuring only the catalyst activity on different supports. The second is the sorption enhanced experiment measuring the activity of catalysis and sorption simultaneously. Both experiments are described in section 3.3.

4.2.1. Activity test

The activity tests for the zeolite 13X, 5A and L impregnated with varying precursors are carried out in the Sabatier setup. Since these samples are already saturated with water, the sorption enhancement is excluded. Also, a mass balance is provided in Appendix I.

From figure 4.4 the Theoretical Equilibrium Conversion (TEC) line of the ideal ratio 4:1 H_2/CO_2 and real input values (retrieved from bypass experiment) are shown. The TEC-line generation method is found in Appendix B.1. The lower actual conversion could be due to a too short residence time or that some NiO were not reduced, or just low activity of the catalyst at low temperature.

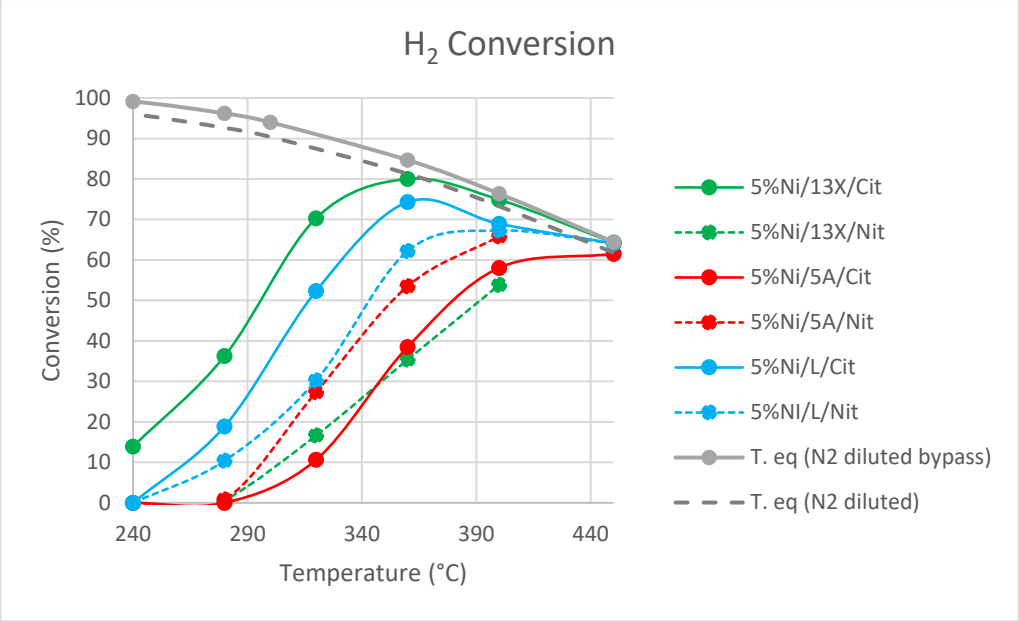

Figure 4.4: H_2 conversion as a function of temperature on varying combinations of supports and precursors. Fixed impregnation methods =EIM. Temperature and the conversion error bars are not larger than the dots itself.

Overall, the order of the activity curves is 5%Ni/13X/Cit > 5%Ni/L/Cit > 5%Ni/L/Nit > 5%Ni/5A/Nit > 5%Ni/5A/Cit > 5%Ni/13X/Nit.
Interestingly, the zeolite L activity is between the 5A and 13X (specifically the Ni-Cit precursor). It was expected to be equal or even higher than the 13X, because of the larger pore size (and the higher amount of cation as found in Appendix A.1). the lower than expected activity could be caused by the high Si/Al ratio of the impregnated zeolite L which repels more CO_2. Unfortunately, no impregnated zeolite L NH_3-TPR is executed within this thesis explaining the role of the BM-CO_2 interaction.
Additionally, figure 4.4 shows that the precursor choice influences the activity in *different ways*. Overall the Ni-Cit represents a higher activity compared to the Ni-Nit may be associated with the support acidity. Weak acidity sites, more present in Ni-Cit than the Ni-Nit BM, favours CO_2 interaction leading to higher activities [18].

The exception is for the 5A. Here, the Ni-Nit performs slightly better than Ni-Cit. It may be due to the location dependency of the available sites for nickel to bind. Ni-Cit is only found outside the surface because the complex size is larger than the 5A pores. Therefore, during calcination (citrate is burned out), the nickel accesses a limited amount of sites which are on the outer 5A surface. In comparison, the smaller Ni-Nit complex has a larger zeolite surface coverage by entering the zeolite pores, as well on the outer surface of the 5A. This location dependency of available sites and the relationship between the precursor and pore size affected probably the nickel content leading to higher conversions for 5%Ni/5A/Nit compared to 5%Ni/5A/Cit.

Another point to be noted is the difference in activity between the Ni-Cit and Ni-Nit per zeolite.
The difference for the L and 5A is relatively small (17% and 20% difference @320 °C) compared with the 13X (54% difference @320 °C). The large difference in 13X activity may be caused by the acidity of the BM. From Wei et al it was found that 5%Ni/13X/Cit possesses higher concentration weak acidic sites (and lower concentration strong acidity sites) compared to 5%Ni/13X/Nit, as shown in table 4.1. This could imply that the 5%Ni/13X/Nit repels CO_2 (acidic) more than 5%Ni13X/Cit due to the larger amount of strong acidic sites. In this context, the acidic concentration between the 5%Ni/5A/Cit and 5%Ni/5A/Nit are compared. Here, the acidity composition as well the total acidity are similar so a less dramatic difference in activity is expected which is correct according to figure 4.4.

Finally, it could be concluded that zeolite 13X and Ni-Cit as the support-precursor set, form the combination for the highest activity possible[6].

	5%Ni/13X/Cit	5%Ni/13X/Nit	5%Ni/5A/Cit	5%Ni/5A/Nit
Total Acidity (μmol/g)	100	120	140	140
Weak (%)	90	58	79	75
Medium (%)	0	12	15	0
Strong (%)	10	30	6	25

Table 4. 1: Acidity concentrations divided in weak, medium and strong acidic per BM. [18].

[6] This statement excludes the variation in impregnation methods, usage of promoters etc.

In this respect, the corresponding selectivity's are shown in figures 4.5 and 4.6. Overall, up till 360 °C the CH_4 selectivity increases as the CO selectivity decrease irrespective of zeolite and precursor choice. For higher temperatures (T>360 °C) the selectivity's stabilizes. However, it was expected at higher temperatures the selectivity would favour the CO due to the endothermic reaction of the Reverse Water Gas Shift (RWGS) as found in equation 4.1. This could indicate that the Ni catalyst decreases the activation energy at higher temperatures for the Sabatier reaction or increases for the RWGS, or both are occurring.

$$CO_2(g) + H_2(g) \rightleftharpoons \mathrm{CO\ (g)} + H_2O\ (g) \qquad \Delta\mathrm{H} = 41\ kJ\ mol^{-1} \quad (4.1)$$

Furthermore, the selectivity also displays that the 5A and 13X have a very high CH_4 selectivity in the 280-360 °C range compared to the zeolite L. The low selectivity at low temperatures of the zeolite L could be caused by the small amount of reduced Ni as shown in the H_2-TPR (fig 4.3).
The comparison between the precursors results that the Ni-Nit has lower CH_4 selectivity (and higher CO selectivity) compared to the Ni-Cit BM. This may be associated with a larger amount of strong acidity for the Ni-Nit which repels the acidic CO_2.

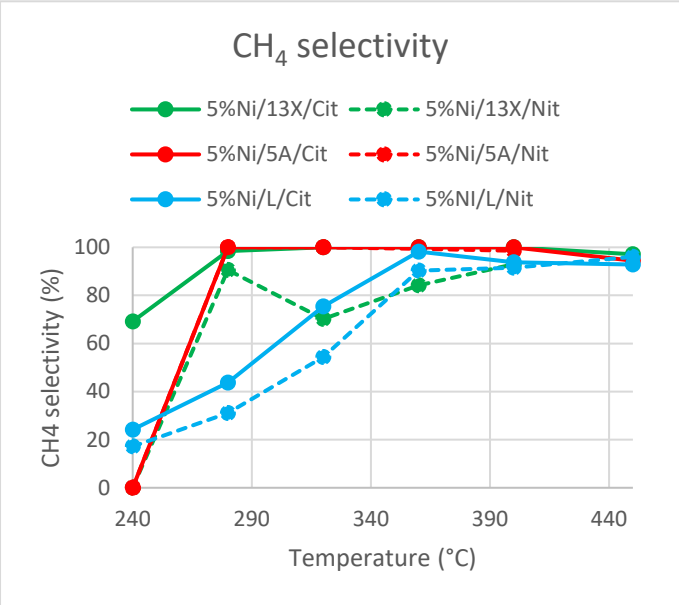

Figure 4. 6: CH_4 selectivity as a function of temperature on varying combinations of supports and precursors, impregnation methods =EIM. Temperature and the selectivity error bars are not larger than the dots itself.

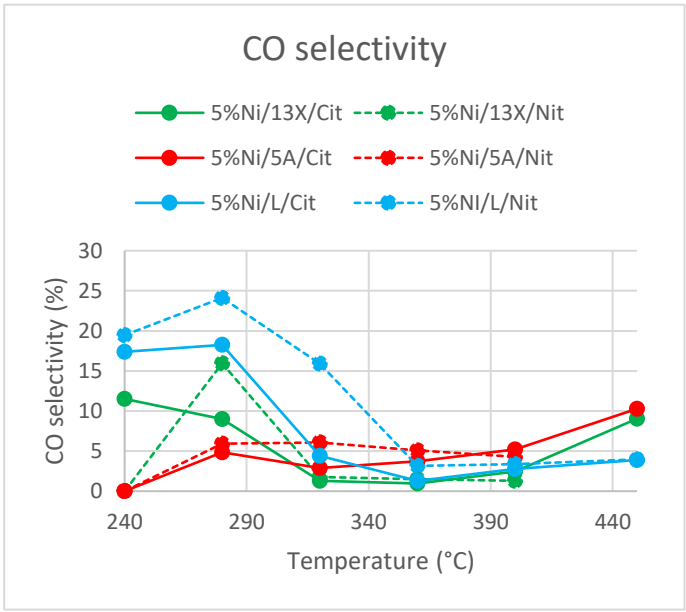

Figure 4. 5: CO selectivity as a function of temperature on varying combinations of supports and precursors, impregnation methods =EIM. Temperature and the selectivity error bars are not larger than the dots itself.

4.2.2. Sorption enhanced methanation test

The activity (conversion) and the selectivity of the sorption enhanced with the corresponding activity test (no water sorption) are found in figures 4.7-9.
Overall, sorption enhancement was observed for the 13X and 5A with approximately 90% H_2 conversion as found in figure 4.7. Surprisingly, zeolite L does not show sorption enhancement, as observing similar H_2 conversions with and without sorption enhancement. Maybe the water particle pressure is below the zeolite L equilibrium pressure, so water could not be adsorbed (water-zeolite interaction).
Furthermore, for the 13X and 5A, it was anticipated that the H_2 conversion would be near 100% due to impregnation as found in figure 1.8. By conducting the bypass measurements, an excess of H_2 input was found (H_2/CO_2=4.52 mol ratio). Hence, the micro-GC portrays that there is too much hydrogen since CO_2 is zero.

figure 4.7 shows a significant increase in activity between the activity test and sorption enhancement test (>60%) compared to the 13X activity difference (±23%). Unfortunately, the current literature does not explain the reason for this phenomena.
The CO_2 activity, presented in figure 4.8, display a similar trend as the H_2 expect for the sorption enhanced test results. Here, 100% conversion is reached, even for the zeolite L which did not undergo sorption enhancement. This may indicate that co-adsorption is taking place in all the zeolites.
Next in figure 4.9, the CH_4 selectivity displays for the input composition exiting the second reactor, as mentioned in Walspurger et al. nearly 100% selectivity irrespective of sorption enhancement or pure catalysis is occurring [46]. Thus, there is no measurable CO formation during sorption enhancement.

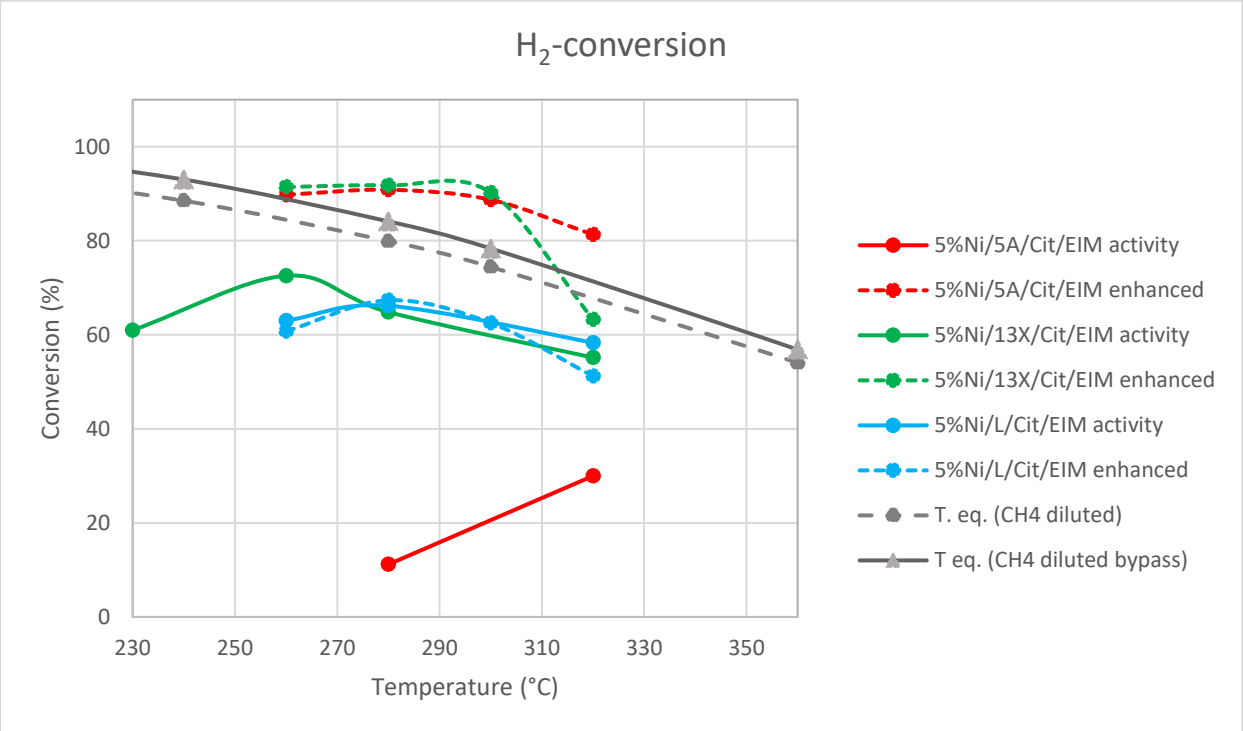

Figure 4. 7: H_2 conversion for the sorption enhanced methanation and activity tests for varying supports. Fixed impregnation methods =EIM & Precursor = Ni-Cit. Temperature and the conversion error bars are not larger than the dots itself.

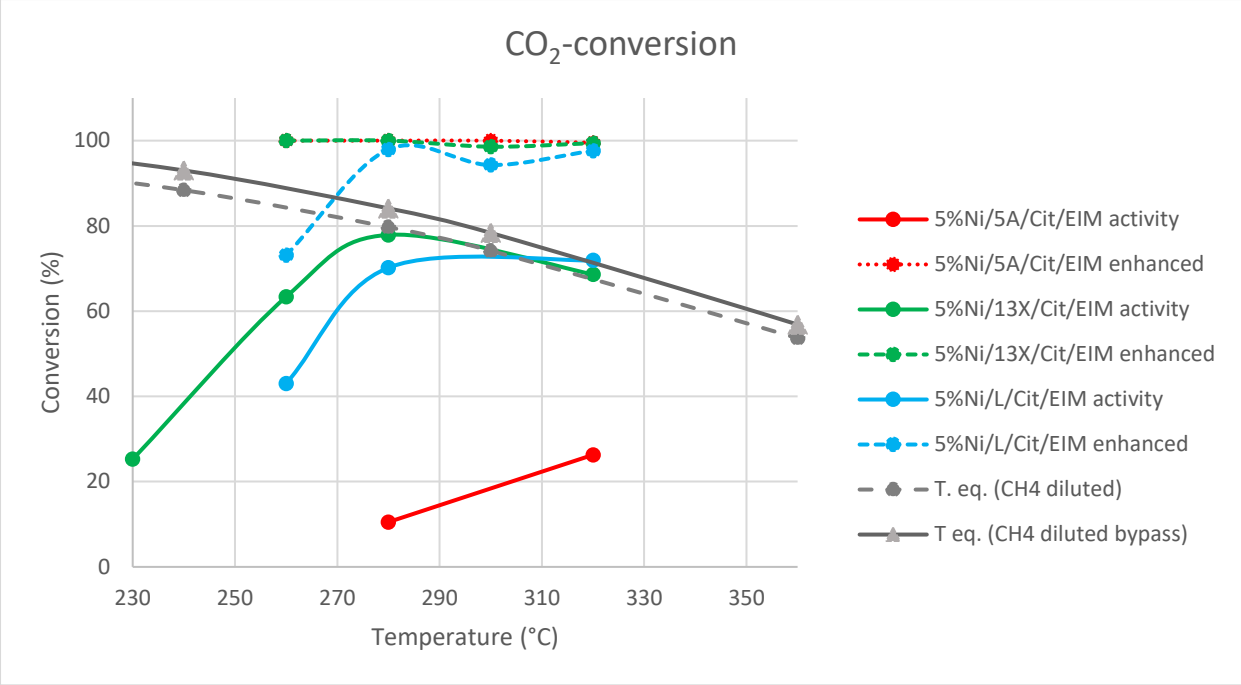

Figure 4. 8: CO_2 conversion for the sorption enhanced methanation and activity tests for varying supports. Fixed impregnation methods =EIM & Precursor = Ni-Cit. Temperature and the conversion error bars are not larger than the dots itself.

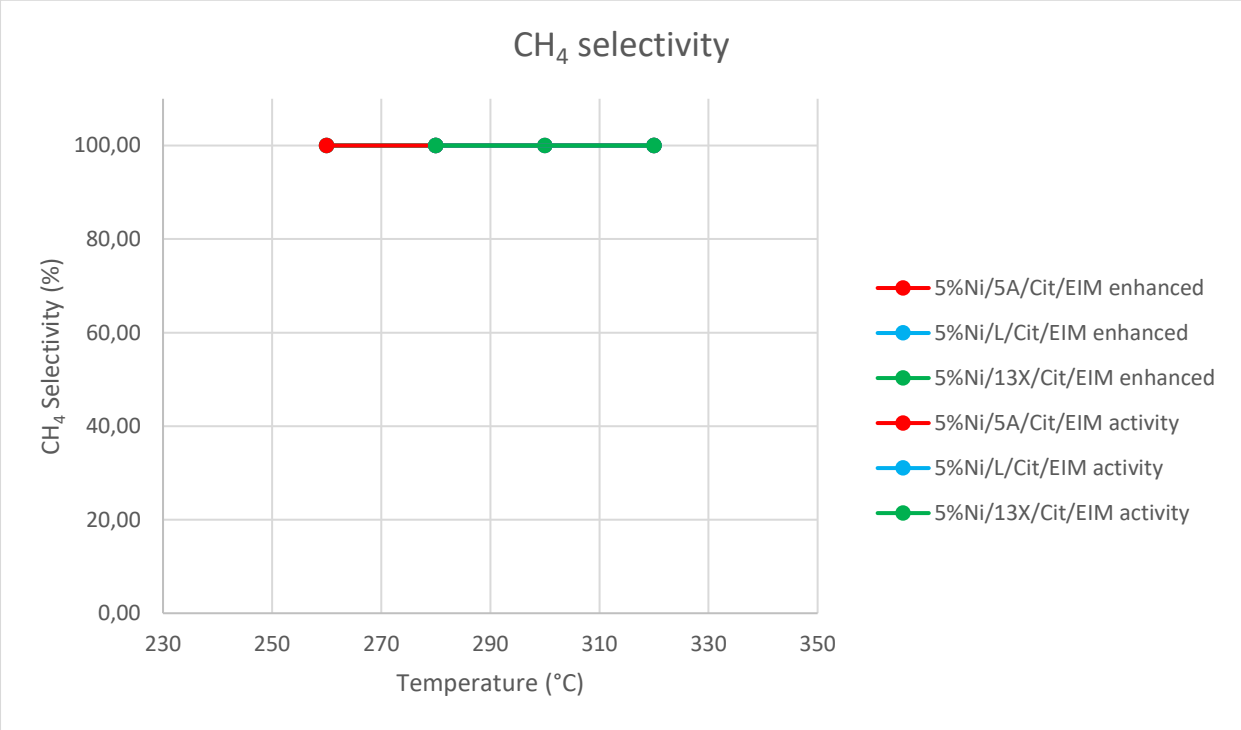

Figure 4. 9: The CH_4 selectivity for the sorption enhanced methanation and activity tests for varying supports. Fixed impregnation methods =EIM & Precursor = Ni-Cit. Due to a near 100% selectivity for every sample, Temperature and the selectivity error bars are not larger than the dots itself. No measurable CO formation in the sorption enhancement since CH_4 selectivity approaches 100%.

The breakthrough curve explains the absorption capacity of the BM during the pre-breakthrough time. These breakthrough curves per sampling temperature are found in Appendix H.1 (13X), H.2 (L) and H.3 (5A). Figure 4.10 displays the curve of 5Ni%/13X/Cit/EIM as a basis in figure 4.10 (also found in Appendix as H.1.1).

Sorption enhancement lasts for around 15.2 min (start time =19 min). This is observed by the micro-GC as CH_4 reaches mass concentrations as high as CH_4 94% and as low as 1.5% H_2, till the CH_4-concentration plummeted to 91%, H_2-concentration increased to 3.8% (end time = 34.2 min). In reality, excess H_2 flow is put through, found from the bypass experiment, and 6% concentration inert N_2 used as a basis of calculating the mass balance. By taking these considerations into account, then the corrected output concentration are CH_4 = 98.6% and H_2 = 1.36%.
A CO_2 breakthrough was observed for the 5A and L (Appendix H.2 and H.3) while it is nonexistent in figure 4.10. This has to do with the CO_2 concentration which is below the lower limit (<1%) of the micro-GC to measure.

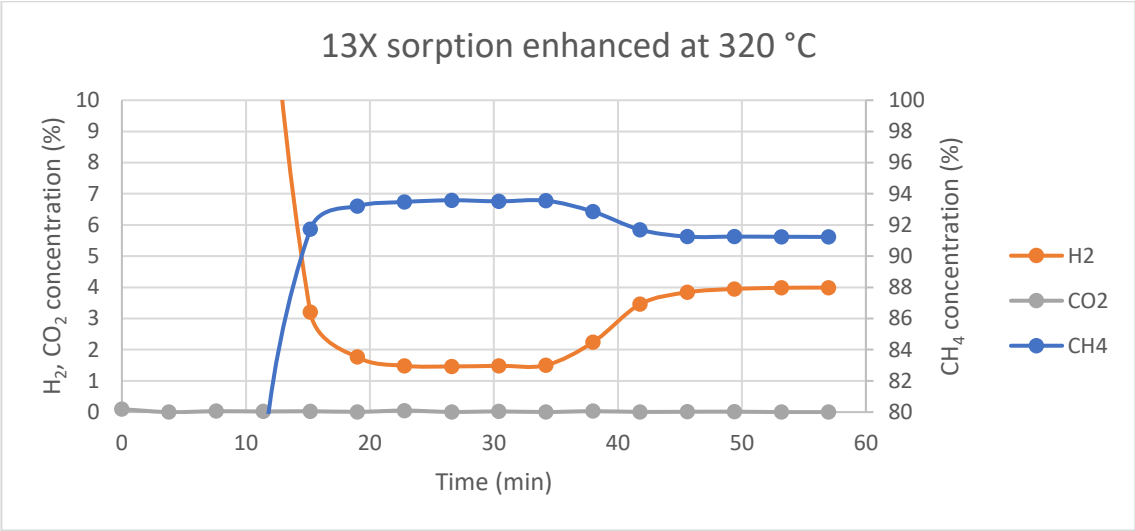

Figure 4. 10: Sorption enhanced methanation illustrating the breakthrough curve by the GC-measurements. Adsorption condition: 320 °C, atmospheric pressure, total material mass: 8.4 gram, Support = 13X, precursor= Ni-Cit, Impregnation= EIM

	liquid water adsorbed (cm3/g)		
T (°C)	5%Ni/13X/Cit/EIM	5%Ni/5A/Cit/EIM	4A
260	-	0.001	0.007
280	0.014	0.002	
300	0.010	0.003	0.005
320	0.006	0.005	
350	-	-	0.004

Table 4. 2: The total water absorbed by the zeolites during sorption enhancement at different temperatures.

The H_2 breakthrough time per temperature for 13X, 5A and 4A (provided from Walspurger et al. [46]) are compared with each other in figure 4.11[46]. The 5A and 13X breakthrough time are derived from the individual breakthrough curves from Appendix H.1 (13X) and H.3 (5A).
Overall, the 5A and 13X display a steeper curve than the 4A sample as the temperature increases. This could be caused by the difference in preparation since 4A is mixed separately from the catalyst in a reactor vessel, while for the other 2 cases the catalyst is impregnated into the zeolite.
Also, the trend shows when raising the temperature the H_2 breakthrough tends to occur earlier (and decreased amount of water adsorption) as expected. The exception is for 5A which could be explained by two phenomena's, the total pore volume (1) and the interaction strength between water and zeolite (2).

Total pore volume: The specific surface area decreases as the total volume increases for 13X and 5A upon impregnation (table 4.3). This is due to the bonding of the catalyst and support, forming additional pores in between the catalyst-catalyst and catalyst-support.
The larger volume upon impregnation suggests, it can hold on more water in its pores, thus increasing the sorption enhancement period, compared to the separately mixed catalyst and zeolite in a reactor vessel, represented by the 4A.
In figure 4.11 it is shown that 13X has a significantly longer breakthrough time, indicating that the pore volume is correlated to the 13X sorption enhancement.
On the other hand, the 5A breakthrough time occurs earlier than the 4A at temperatures lower than 310 °C while it pore size increases upon impregnation. This indicated that the total pore volume does not have a significant effect on the breakthrough time.
In addition, the total volume is given in table 4.3. are larger than the total liquid water adsorbed by the BM during sorption enhancement, as found in table 4.2. This difference could be due to volume determination in table 4.2 is by H_2O and in table 4.3 by N_2 or by the varying of the used precursor.
Water-zeolite interaction strength: Regarding the 5A, it may after 2h regeneration the water did not fully desorb at 1 bar operating pressure (or too low regeneration temperature). To validate this prediction, isostere graphs (out of thesis scope) should be generated as the relationship between temperature and water partial pressure may explain the 5A deviated H_2 breakthrough time.

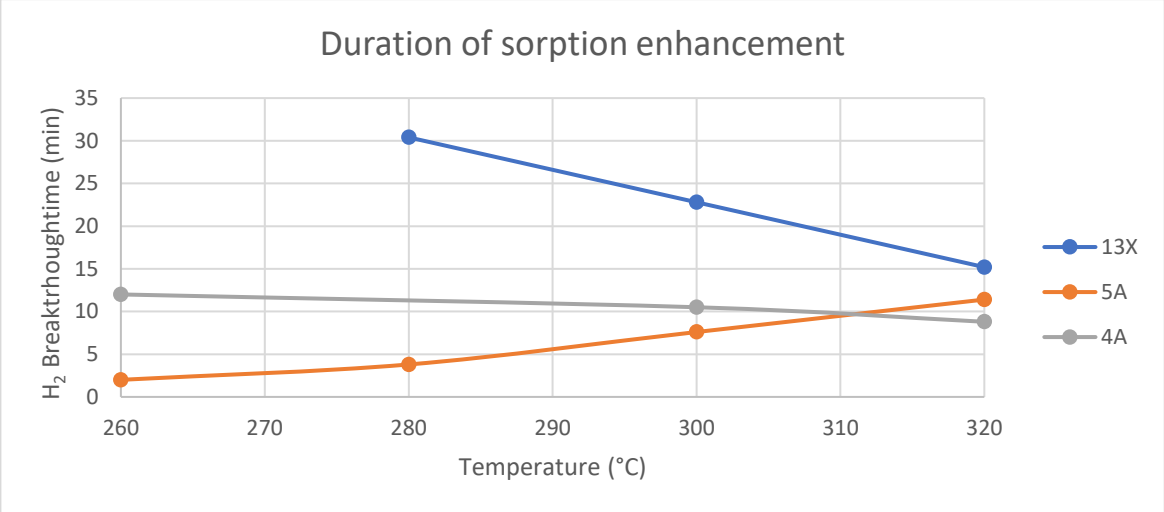

Figure 4. 11: Breakthrough time of H_2. The sorption enhancement of the 4A zeolite is from Walspurger et al. [46] The Temperature and H_2 Breakthrough error bars are not larger than the dots itself.

Sample	Specific surface area (m^2/g)	Tot_{volume} (cm^3/g)
Fresh 13X	654.78	0.27
5%Ni/13X/Nit/EIM	361.49	0.89
Fresh 5A	592.52	0.25
5%Ni/5A/Nit/EIM	454.14	1.01

Table 4. 3: N_2 physisorption of fresh and impregnated zeolites displaying the specific surface area and pore volume [18]

5. Results and discussion - Cleaned BM

The primary focus in this chapter is to compares cleaned BM (impregnation method = FIM) with regular BM[7] (impregnation method = EIM) from the previous chapter. Here, the influence on the nickel loading is examined with the SEM and EDX. Thereafter, the activity peaks are investigated with the TPR and conversion (and selectivity) in the activity test. Finally, the pore structure of the cleaned and the regular BM are compared with non-interacting Al_2O_3-support impregnated with catalyst.

5.1. SEM analysis

The SEM analysis is divided up in two. The first part compares between regular and cleaned BM with altering precursor and impregnation method per zeolite. The second part compares the impregnated Al_2O_3 and zeolite-based support.

5.1.1. Comparison between regular and cleaned BM

Zeolite 5A: The 5A SEM pictures are found in Appendix C.1. Overall, by comparing the fresh zeolite 5A (C.1-1) with 5A impregnated with various combination of precursors and impregnation methods (C.1-2 till C.1-5), it can be observed that every impregnation was successfully conducted.
The difference lies in the concentration of observed precursors. As expected, by washing the BM (FIM) less catalyst was observed on the surface by comparing it with regular BM (EIM) as shown in figure 5.1. This implies that most catalyst was impregnated outside the pores, irrespective of precursors type, which made washing agglomerated catalyst on the 5A zeolite relatively effortless.
By altering the precursor, it seemed that the Ni-Cit (C.1-2) has precipitated more than the Ni-Nit (C.1-4). The Ni-Nit molecule is smaller in size than the 5A pores, so it may be that a large amount is present into the zeolite structure, which was not visible on the SEM pictures.

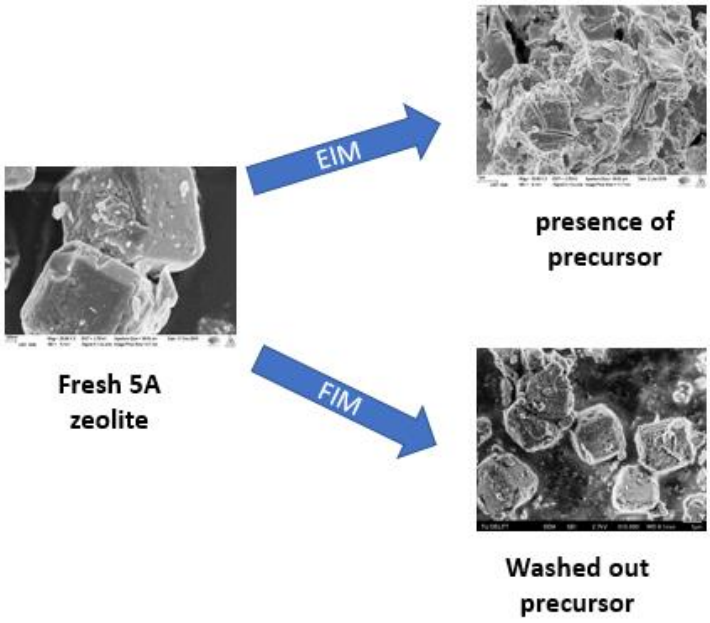

Figure 5. 1: SEM backscattered picture of impregnated Ni-Cit visualizing the difference between EIM and FIM method

Zeolite L: The relevant zeolite L pictures are located in Appendix C.2. By comparing the fresh zeolite L (C.2-1) with the EIM impregnation (C.2-2 & C.1-4), clumps/spots of Ni-Cit and Ni-Nit are noticed on the surface of the zeolite. Furthermore, the cleaned BMs (C.2-3 & C.2-5) have less agglomerated precursor on the surface. Thus, most of the precursor is present on the outer surface layer of the L which was unexpected due to the larger pore size for entering into the zeolite structure. It may be that the surface within the structure of the zeolite L is saturated with precursor, so the excess must bound to the outer surface of the zeolite which is sensitive to washes. From IZA it is found that the accessible area within the zeolite L, 13X and 5A structure are 694.6, 1211.42 and 1204.87 m^2/g respectively, which may substantiate the hypothesized oversaturated zeolite L. Regarding, the comparison between the Ni-Cit (C.2-2) and Ni-Nit (C.2-5), there is no noticeable difference found.
Zeolite 13X: The backscattered 13X SEM pictures are displayed in Appendix C.3. Here, the difference between fresh, cleaned or regular impregnated with Ni-Cit or Ni-Nit is not obviously visible by the SEM pictures. This indicates that the nickel loading is not affected by the cleaning method (FIM) on the 13X compared to the 5A and L washes. It may be caused by the preference of precursors to reside into the zeolite structure due to large pore sizes for easy entrance. Just a small amount of precursor, sensitivity

[7] Only the BM impregnated with NI-Citrate as it results in the highest activity overall

for washes, are present on the outside zeolite surface, making the visible comparison between EIM and FIM for the 13X difficult.

5.1.2. Comparison between Al_2O_3 and zeolitic support

The SEM pictures between the paired up modified zeolite and Al_2O_3 support according to table 3.2 are found in Appendix D. Here, pore structure between the 5%Ni/13X/Cit/EIM (D.1.2) and 5%Ni/Al_2O_3-ɣ /Cit/EIM (D.1.3) look similar, whereas the 5%Ni/L/Cit/EIM (D.1.1) have sharp cylindrical shapes which may affect the activity and nickel loading.
The beforementioned observations are similar for the washed version namely, 5%Ni/L/Cit/FIM (D.1.6), 5%Ni/13X/Cit/FIM (D.1.7) and 5%Ni/Al_2O_3- ɣ /Cit/FIM (D.1.8)
Next, the 5%Ni/5A/Cit/EIM (D.1.4) and 5%Ni/Al_2O_3- α/Cit/EIM (D.1.5) are visually comparable. The 5A is cubicle formed and has significantly more Ni-Cit present than the asymmetrically formed Al_2O_3- α indicating higher activity.

5.2. EDX-analysis: Relationship between nickel loading & washing

The determination of the nickel loading by washing is conducted following the experimental setup as explained in section 3.2.3. As concluded from Section 4.2.1, the 5%Ni/13X/Cit had the highest activity, so the zeolite L, 5A and all zeolites impregnated with Ni-Nit were omitted for this experiment.

The EDX results for the nickel content are shown in figure 5.1. Overall, the order of the Ni content is 5%Ni/L/Cit/EIM > 5%Ni/13X/Cit/EIM > 5%Ni/5A/Cit/EIM > 5%Ni/13X/Cit/FIM > 5%Ni/L/Cit/FIM > 5%Ni/L/Cit/FIM. Clearly, the regular BM irrespective of the support contains significantly higher nickel content. This was anticipated, because the remaining nickel in the solution, after 24h impregnation, is omitted from the FIM preparation whereas the EIM precipitates this nickel amount on the zeolite as described in section 3.2.3.
Also, increasing the amount of washing the BM did not have a noticeable effect on the nickel loading as shown in figure 5.2. Changing the impregnation method to FIM without additional washing (1,2,3,4 or 5x) is sufficient enough preparing cleaned BM. Thus, from now on forth the cleaned BM will be represented with the 4 times washed FIM sample (5%Ni/13X/Cit/FIM/4x. 5%Ni/5A/Cit/FIM/4x. 5%Ni/L/Cit/FIM/4x).
By comparing between cleaned and regular BM per zeolite, the 5A and L lost most catalyst by altering the impregnation method in comparison to zeolite 13X. These results quantify the discussion in section 5.1. (nickel loss 13X = 51.3%, L =58.1% & 5A = 84.9%)

- 84.9% of all catalyst impregnated on the 5A is located on the outside surface as expected illustrated in figure 5.1.
- 58.1% of the catalyst is impregnated on the outside surface of the zeolite L, which may be caused by the oversaturated inner surface of the L by precursor as shown in Appendix A.1.
- Even though the nickel was not visible on the surface of the 13X, 51.3% of the precursor is probably washed out. This could imply that the SEM was not adjusted correctly, producing fuzzy pictures, so differentiating between 13X/EIM and 13X/FIM was not clear. Also, it could be that some parts of the zeolite structure washed out a significant amount of Ni-Cit.

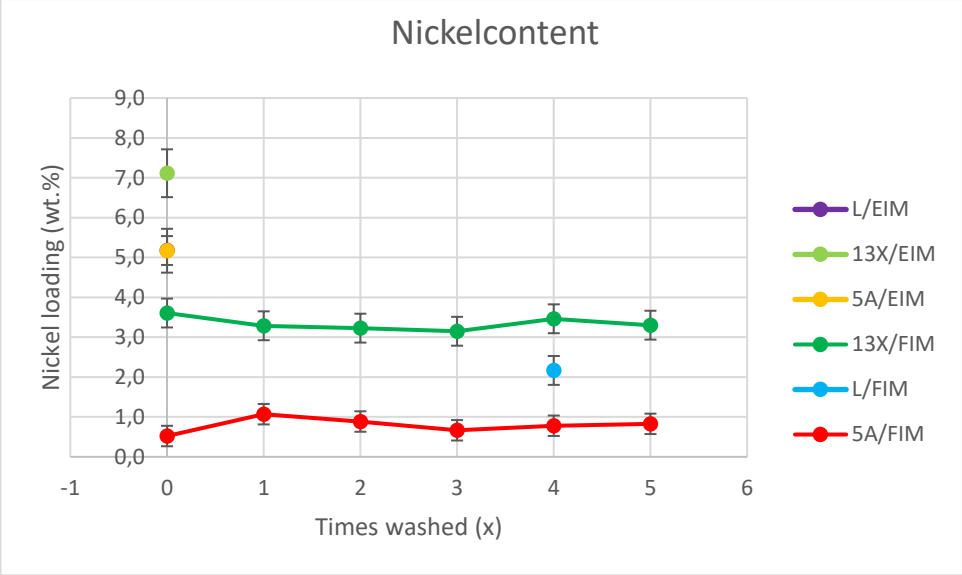

Figure 5.2: The EDX nickel loading varying impregnation methods on zeolite 13X, 5A and L, fixed precursor: Ni-Cit. The L/EIM value overlays the 13X/EIM (green dot) since its nickel loading is approximately the same.

The nickel content of cleaned and regular bifunctional materials are compared with impregnated Al_2O_3 support based on the comparable support's pore structure as displayed in table 5.3. The justification for making these pairs are explained in section 3.2.4.

Overall as expected the nickel loading supports impregnated with the EIM preparation is higher than the FIM prepared. Due to similar support's pore structure, the nickel loadings per pair are within 2wt.% absolute difference except for the 2nd and 5th pair.

No significant difference in nickel loading is found comparing Al_2O_3-ɣ and Al_2O_3-α, even though the impregnation method was altered.

Pair (#)	Bifunctional samples (zeolite)	Reference samples (Al_2O_3)
1	5%Ni/5A/Cit/EIM	5%Ni/Al_2O_3-α/Cit/EIM
2	5%Ni/13X/Cit/EIM	5%Ni/ Al_2O_3-ɣ/Cit/EIM
3	5%Ni/L/Cit/EIM	
4	5%Ni/13X/Cit/FIM	5%Ni/ Al_2O_3-ɣ/Cit/FIM
5	5%Ni/L/Cit/FIM	

Figure 5. 3: The expected comparable nickel loading between the impregnated zeolitic and Al_2O_3 support

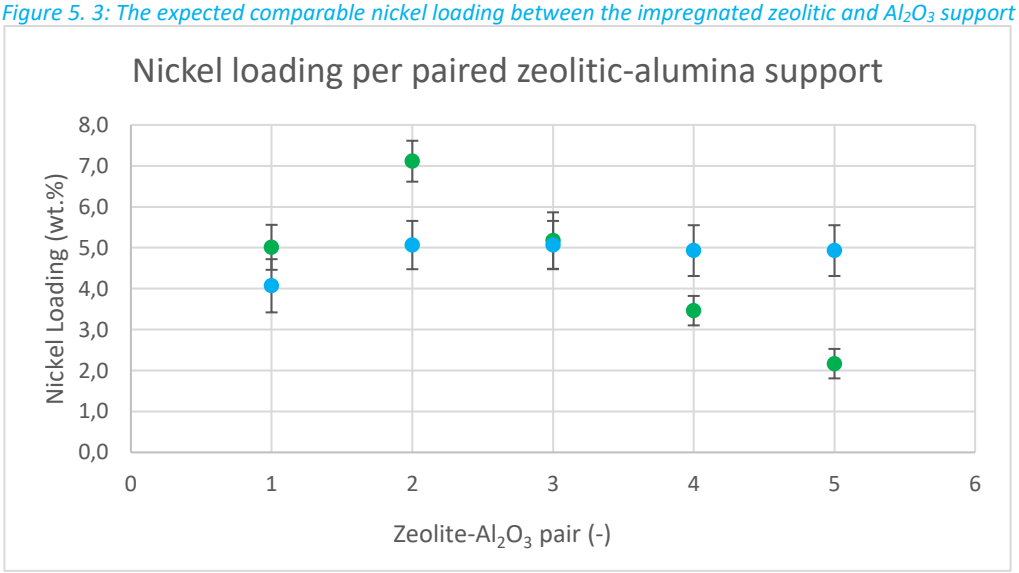

Figure 5. 4: EDX nickel loading comparison between impregnated zeolite(green dots) and impregnated Al_2O_3 support (Blue dots).

5.3. TPR analysis

It can be observed in figure 5.5. that all EIM sample's reduction peaks are more intense than the FIM samples. The difference per zeolite is more clear in Appendix E.1-3. Even though the nickel content of FIM samples are between 20-50% wrt. EIM samples depending on the zeolite (fig 5.2), just a small fraction of that amount of nickel oxide is activated. Suggesting a different reduction mechanism is governing at lower loaded Ni-catalyst on the zeolite.

Furthermore, the minor FIM sample's peaks were analyzed in Appendix F.4. Only one peak per zeolite is observed between 400-500 °C. as predicted, these peaks correspond to nickel precursor present within the zeolite structure as mentioned in section 4.1.4. The peak in the 300-350 °C range corresponding to catalyst presence on the zeolite surface outside, is missing which was also expected as mentioned in section 5.1. Also, the TPR measures negative values, which could be caused by the detector operating at its lower limit resulting in the error.

Surprisingly, the FIM samples (fig F.4.) displays an broader peak (13X/FIM = 540 °C, L/FIM= 260 °C, 5A/FIM = 100 °C) compared to the narrow EIM peaks (13X/EIM = 200 °C, L/EIM= 80 ° C, 5A/EIM = 80 °C). Thus, the reduction at 450 °C from section 3.2.1. may not reduce all the nickel precursor leading to lower conversions for FIM samples in the activity test.

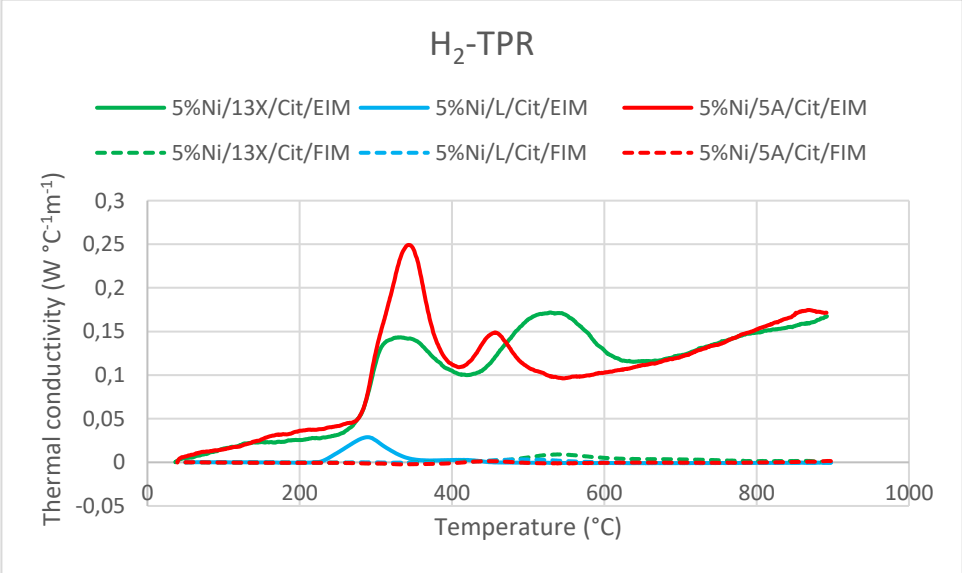

Figure 5. 5: H_2-TPR of various zeolites and impregnation methods, fixed precursor = Ni-Cit. Total mass: 0.5 gram. The 5%Ni/L/EIM seems to have similar thermal conductivity as the FIM samples. Large stains of nickel particles on the zeolite L are observed from SEM pictures (fig 4.2b), indicating that the inner parts are not reduced which lead to low thermal conductivity.

5.4. Activity results

The activity tests for the zeolite 13X, 5A and L impregnated with varying precursors and impregnation methods are carried out in the Sabatier setup as described in section 3.3. From figure 5.6, all H_2 activity curves are below the bypass determined TEC-line. This is since the samples are already saturated with water, so excluding the sorption enhancement. TEC-line generation methods are found in Appendix B.1. The lower actual conversion could be due to too short residence time or that some NiO was not reduced, or just low activity of the catalysts at low temperature.

Overall, the order of the activity curves is 5%Ni/13X/Cit/EIM > 5%Ni/L/Cit/EIM > 5%Ni/5A/Cit/EIM ~ 5%Ni/13X/FIM > 5%Ni/5A/Cit/FIM ~ 5%Ni/L/Cit/FIM. As anticipated, the EIM samples performed better than the FIM samples by a significantly higher nickel content as shown in figure 5.2.
Specifically for the 13X/FIM and L/FIM, their reduction peaks (E.4) occur at temperatures higher than the used reduction temperature (450 °C). This implies that higher activities could be reached. Unfortunately, the zeolites deteriorate from 500 °C onwards which is highly undesirable and unfeasible for future sorption enhanced experiments as the water absorptivity decreases by increasing temperatures [19].
Figure 5.6 also displays that the activity of 5%Ni/5A/Cit/FIM and 5%Ni/L/Cit/FIM are comparable. This was expected because of comparable nickel loading within the 1.5 wt.% range (fig 5.2). The unpredictable part is the lacking activity optimum ranging between 240-450 °C. In fact, it could be anticipated that the peak occurs at temperatures above 450 °C since it trends upwards as the temperature increases. However, the zeolite deteriorates and water absorptivity decreases with rising temperatures [19].
Surprisingly from the FIM samples, the 13X competes with 5A/EIM while the nickel content is lower. Figure 5.7 displays the conversion per gram nickel catalyst per sample. Here, most samples are below the 250% H_2 conversion per gram nickel, exceptions for the 5%Ni13X/Cit/FIM. The other unexpected sample with high catalyst effectively is the 5%Ni5A/Cit/FIM. Even though the 5A has a low H_2 conversion (fig 5.6), it proves to have a high conversion per gram catalyst and the maximum effectivity is not observed within the given temperature range. The reasoning for this is unclear and not found in the current literature.

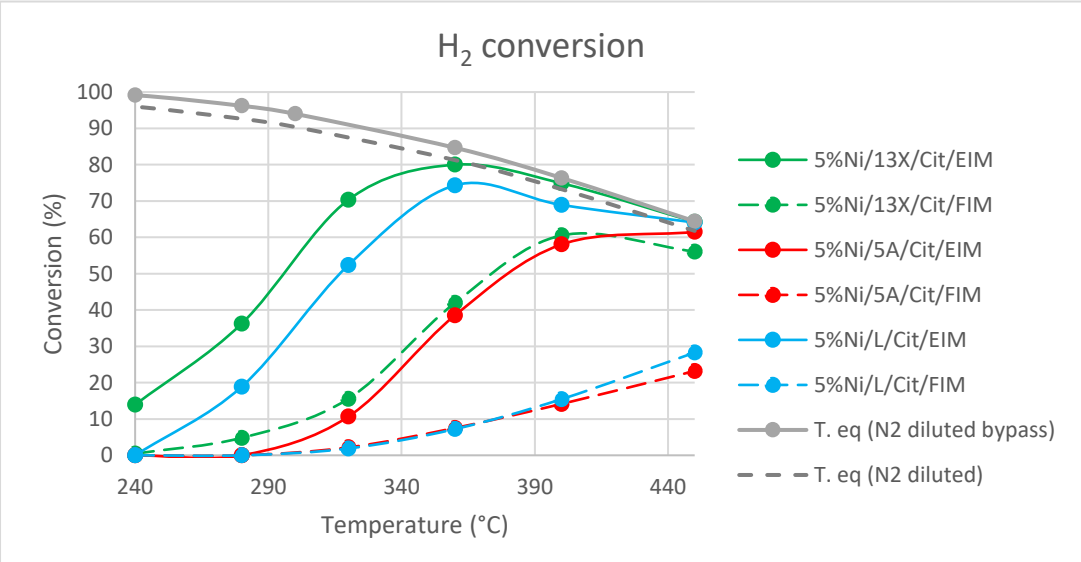

Figure 5. 6: H_2 conversion as a function of temperature on varying combinations of supports and impregnation methods, fixed precursor = Ni-Cit. Temperature and the selectivity error bars are not larger than the dots itself.

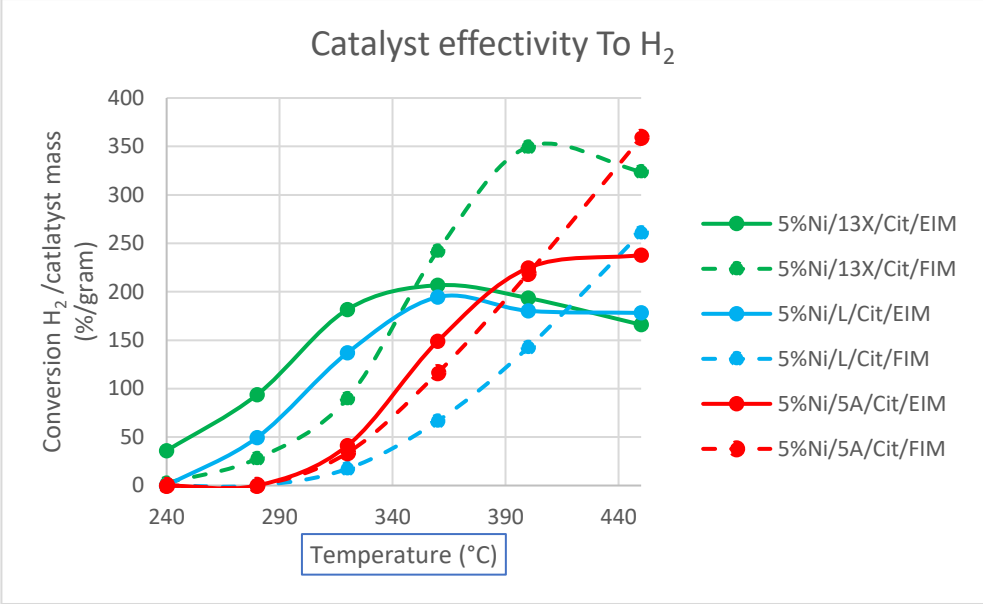

Figure 5. 7: Catalyst effectivity to H_2 in conversion per gram Nickel. Temperature and the conversion error bars are not larger than the dots itself.

Additionally, the selectivity's (CO & CH_4) of these samples are compared in figures 5.8 and 5.9. Generally, It is observed that EIM samples produce more CH_4, especially for the 5A and 13X for almost the whole temperature range. On the other hand, FIM samples are more selective to CO (fig 5.8) as the temperature rises, for instance, the 5%NiL/Cit/FIM at 400 °C with a CO selectivity up to 62%.
These phenomena are explained by Chen et al. proposing that poorly loaded nickel catalyst (representing FIM samples) have smaller H_2 coverage resulting in rapid CO production. In comparison with a highly loaded catalyst (representing EIM samples) possessing more active H_2 sites leading to higher coverage thus favouring CH_4 production [38].
Also, an order of CH_4 selectivity for FIM samples are identified which are the inverse order for the CO selectivity as expected. It may be that the 13X support is an active material during Sabatier reaction and the L for CO RWGS while the 5A is between them for CH_4 and CO selectivity [1].

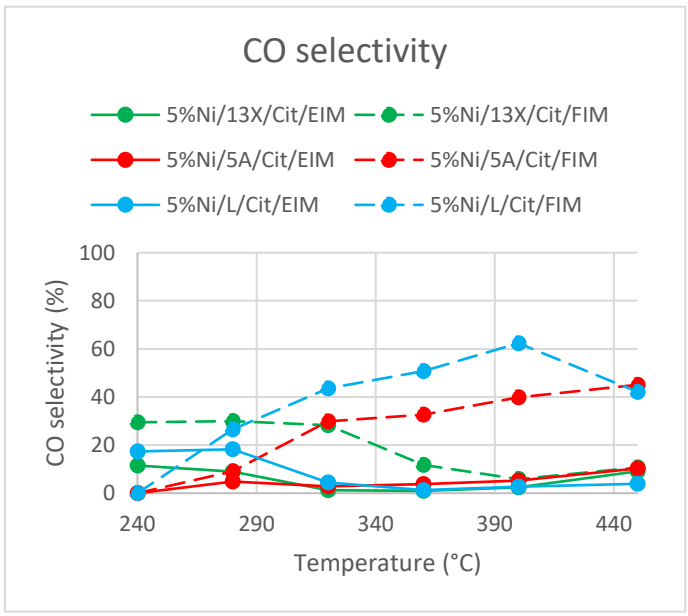

Figure 5. 8: CO selectivity as a function of temperature on varying combinations of supports and impregnation methods, fixed precursor = Ni-Cit. Temperature and the selectivity error bars are not larger than the dots itself.

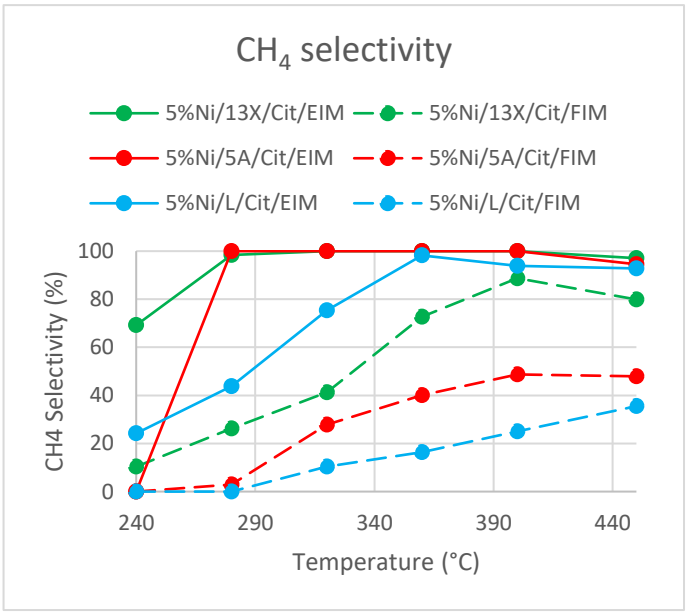

Figure 5. 9: CH_4 selectivity as a function of temperature on varying combinations of supports and impregnation methods, fixed precursor = Ni-Cit. Temperature and the selectivity error bars are not larger than the dots itself.

Lastly, the activity curves between the (regular and cleaned) BM and the reference samples are compared. Figure 5.10 superpositions the Al_2O_3 support over figure 5.6. Table 5.1 summarizes the expectations from section 3.2.5. and the real comparable activities between the two distinct samples.
Overall, similar-looking pore structures between the zeolite and Al_2O_3 support do not lead to comparable activity. From them only 5%Ni/13X/Cit/EIM is represented by the correct Al_2O_3 support and the 5%Ni/L/Cit/EIM for T <320 °C.

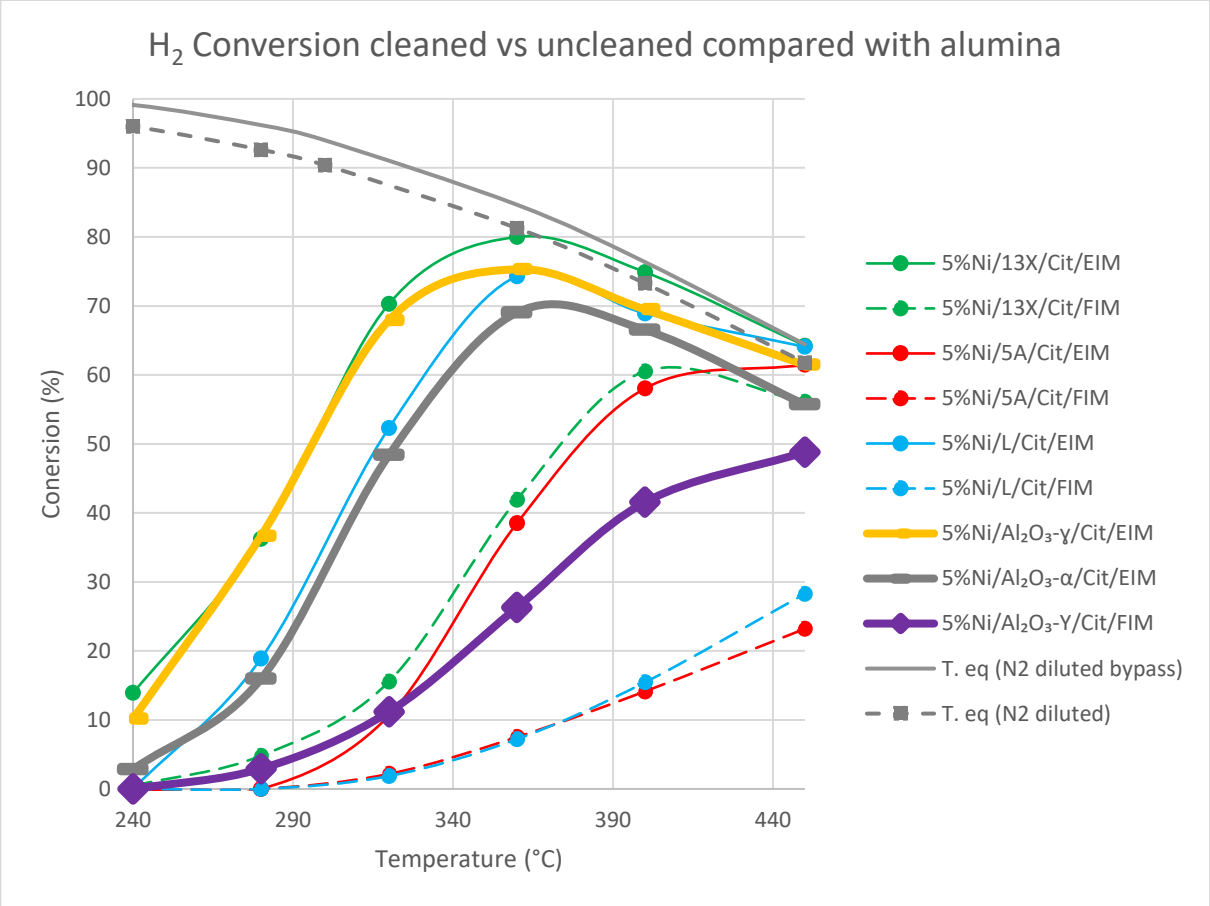

Figure 5. 10: H_2 conversion comparison between zeolitic and Al_2O_3 based support. Temperature and the conversion error bars are not larger than the dots itself.

Pair (#)	$A_{zeolite}$	Expected A_{Al2O3}	Comparable Activity
1	5%Ni/5A/Cit/EIM	5%Ni/Al_2O_3-α/Cit/EIM	$A_{Zeolite}<A_{Al2O3}$
2	5%Ni/13X/Cit/EIM	5%Ni/ Al_2O_3-ɣ/Cit/EIM	$A_{Zeolite}\sim A_{Al2O3}$
3	5%Ni/L/Cit/EIM		$A_{Zeolite}\sim A_{Al2O3}$ (<320 °C)
4	5%Ni/13X/Cit/FIM	5%Ni/ Al_2O_3-ɣ/Cit/FIM	$A_{Zeolite}>A_{Al2O3}$
5	5%Ni/L/Cit/FIM		$A_{Zeolite}<A_{Al2O3}$

Table 5. 1: The expected and observed activities by comparable pore structure between the impregnated zeolitic and Al_2O_3 support.

6. Conclusions and recommendations

6.1. Conclusions

The broad goals of this thesis are: Do BPS zeolites improve the sorption enhanced CO_2 methanation (1) and how do cleaned BM affect the activity (2)?

The general results could be summarized in:

1. The BPS zeolite, which is the zeolite L, did result in high activities. Unfortunately, no sorption enhanced methanation occurred, whereas it did for the impregnated 13X and 5A.
2. The cleaned BM reduced the activity significantly but the BM became more selective to CO production as it is undesired. However, the effective activity of cleaned BM, especially for the 13X and 5A are higher than regular BM.

6.1.1. Regarding the Sorption enhanced CO_2 methanation by the BPS zeolite

Initially, a commercial BPS zeolite was investigated. However, appropriate commercial zeolite could not be retrieved based on the required criteria. Thus, from the 237 zeolites, zeolite L is found to be suitable (bigger pore sized and similar characteristics as the 13X and 5A), and thereby synthesized. The following results were found from various characterization:

XRD/SEM/EDX: Validating zeolite L synthesis and catalyst impregnation

- Reactants: Some main peaks of the reactants, SiO_2 and $Al(OH)_3$, appear to lack in the XRD results. This indicates that the starting mixture did undergo some reaction.
- Product: All four main peaks representing the crystalline structure of the zeolite L were present in the XRD result of the synthesized sample, confirming a successful zeolite synthesis.
- Morphology: The synthesized zeolite L crystals were observed as cylindrical shapes in the SEM pictures. This morphology agrees with the literature[32] for the used starting gel composition in the experiment, confirming the successful zeolite L synthesis.
- Impregnation: The nickel precursor (Ni-Nit or Ni-Cit) impregnated on the zeolite are only noticeable as stains compared with freshly unimpregnated zeolite L in the SEM pictures. Also, the EDX examined a Ni-loading on the zeolite L comparable to the impregnated 13X and 5A zeolites. This shows that impregnation does appear on the zeolite L.

H_2- TPR: Locating impregnated catalyst by reduction peaks

- 13X and 5A: The 13X and 5A have 2 peaks indicating that nickel oxides formation is location dependent. The lower peak range (300-350 °C) could be corresponding to catalyst reduction outside the pores whereas the peak range at higher temperatures (450-550 °C) is associated with reduction inside the pores.
- Zeolite L: The two peak ranges are nearer each other (300-350 °C and 420 °C) suggesting that most of the precursor is located outside the zeolite L pores.
- Thermal conductivity: It appears that the thermal conductivity (intensity) of the zeolite L over the whole temperature range is far lower compared to 13X and 5A. SEM pictures show large stain on the L representing large nickel particles. It could be that the inner part of these agglomerated nickel is not reduced, so returning a weaker signal to the TCD.

After the characterizations, two distinct tests were executed in the Sabatier setup to compare CO_2 methanation performances between different BM. Tables 6.1. and 6.2. give a summarized overview of the results.

1. Activity Test:

- Overall activity: The order of the activity curves is 5%Ni/13X/Cit > 5%Ni/L/Cit > 5%Ni/L/Nit > 5%Ni/5A/Nit > 5%Ni/5A/Cit > 5%Ni/13X/Nit. **This shows that the zeolite L did not outperform the 5%Ni/13X/Cit. Making the 13X and Ni-Cit the support-precursor combination achieving the highest activity possible.**
- Support influence: The zeolite L activity is between the 5A and 13X. It was expected to be equal or even higher than the 13X, because of the larger pore size (and the higher amount of cation). The lower than expected activity could be caused by the zeolite L Si/Al ratio which is higher than the 13X (higher SI/Al = Repels more CO_2).
- Precursor influence: The precursor choice influences the activity in *different ways*. Overall, Ni-Cit represents a higher activity compared to the Ni-Nit which may be associated with the support acidity favouring CO_2 interaction leading to higher activities.
  The exception is for 5A where Ni-Nit (small complex) performs slightly better than Ni-Cit (large complex). It may be that the nickel content is lower for the Ni-Cit as its complex size is larger than the 5A pore, thus not reaching the available sites of the inner zeolite structures.
- Selectivity:
  - Overall selectivity: **The 5A (irrespective of precursor) and the 5%Ni/13/Cit result the near 100% CH_4 selectivity over the whole temperature range.**
  - Support influence: The 5A and 13X have a very high CH_4 selectivity in the 280-360 °C range compared to the zeolite L. The low selectivity at low temperatures of the zeolite L could be caused by the small amount of reduced Ni.
  - Precursor influence: The generally, the Ni-Nit BM have lower CH_4 selectivity (and higher CO selectivity) compared to the Ni-Cit BM. This may be associated with a larger amount of strong acidity for the Ni-Nit which repels the acidic CO_2 leading to lower activity.
  - Byproducts: In the 240-360 °C range the CH_4 selectivity increases as the CO selectivity decrease irrespective of zeolite and precursor choice. For every BM at higher temperatures (T>360 °C,) stabilizes as the CH_4 selectivity reaches 100%, and the CO drop to near 0%.

Sample	Activity	CH_4 selectivity (<360 °C)
5%Ni/13X/Cit	++	++
5%Ni/L/Cit	+	+-
5%Ni/5A/Cit	+-	++
5%Ni/13X/Nit	-	+-
5%Ni/L/Nit	+-	-
5%Ni/5A/Nit	-	++

Table 6. 1: Overview samples with inflow composition (20 v/v% H_2, 5 v/v% CO_2, 75 v/v% N_2)

2. Sorption enhanced methanation test:

- Overall results: **5%Ni/L/Cit does not undergo sorption enhancement whereas 5Ni/13X/Cit and 5%Ni/5A/Cit did result activities above the theoretical equilibrium. Maybe the water particle pressure is below the zeolite L equilibrium pressure, so water could not be adsorbed.**
- Selectivity: Nearly 100% CH_4 selectivity is reached irrespective of the support. No CO byproducts were measured.
- Activity: The 13X and L activity (without sorption) for the given input composition as found in table 6.2. are very high. However, the 5A activity low without a good explanation from literature.
- Breakthrough time/water adsorption: Overall, the trend is as the temperature decreases the time to break through extends, and the amount of water adsorption increases. Here, 13X follows this trend. The exception is for 5A following an inverse trend. This could be caused by:
    - Total pore volume: the 5A available volume increases upon impregnation suggesting it can hold on more water. Yet, the 5A sorption time is shorter than the 4A (reference sample) indicated that the total pore volume does not have a significant effect on the breakthrough time it.
    - Water-zeolite interaction strength: It may after regeneration that, the water did not fully desorb at 1 bar operating pressure (or too low regeneration temperature) because of the strong water-zeolite strength.

sample	Sorption enhancement	CH_4 Selectivity (of sorption enhancement)	Activity	Breakthrough time	Amount Water sorption
5%Ni/13X/Cit	+	+	+	++	++
5%Ni/L/Cit	-	N.A.	+	N.A.	-
5%Ni/5A/Cit	+	+	-	-	+-
4A (Walspurger et al. [46])	+	+	N.A.	-	+

Table 6. 2: results overview samples with inflow composition (9.9 v/v % H_2, 2.5 v/v % CO_2, 81.6 v/v % CH_4, 6.0 v/v % N_2)

6.1.2. Regarding the effect of cleaned BM on the activity

The regular BM (impregnation method =EIM) and cleaned BM (impregnation method =FIM) were compared. Various characterizations were used as follows:

SEM/EDX: Identifying nickel presence + nickel content

- Overall nickel content: The order of the Ni content is 5%Ni/L/Cit/EIM > 5%Ni/13X/Cit/EIM > 5%Ni/5A/Cit/EIM > 5%Ni/13X/Cit/FIM > 5%Ni/L/Cit/FIM > 5%Ni/L/Cit/FIM found from the EDX. Clearly, regular BM irrespective of the support contains significantly higher nickel content. This is because the remaining nickel in the solution, after 24h impregnation, is omitted from the FIM preparation whereas the EIM precipitates this nickel amount on the zeolite.
- Overall relation nickel content and washing: Increasing the amount of washing the BM did not have a noticeable effect on the nickel loading. Changing only the type of impregnation method from EIM to FIM without additional washing (1,2,3,4 or 5x) is sufficient enough preparing cleaned BM.
- Support influence: The 13X compared to the 5A and L is relatively unaffected by washing (FIM) because most catalyst resides into the zeolite structure due to large pore sizes for easy entrance (5A lacks) and the sufficient available sites (L lacks). (nickel outside surface 13X = 51.3%, L =58.1% & 5A = 84.9%).
- Comparison nickel content - Al_2O_3 and zeolitic support: For clarity, the comparison between the supports are found in table 6.3. The pore structure of pair 1,2,4 look similar in the SEM pictures. On the contrary pairs 3 and 5, look different due to the zeolite L sharp cylindrical shapes which may result in different activity and nickel loadings.

- Generally, supports impregnated by EIM have higher nickel loading. Due to similar pore structures, the nickel loadings per pair are within 2wt.% absolute difference (EDX) except for the 2nd and 5th pair.
- No significant difference in nickel loading is found comparing Al_2O_3-ɣ and Al_2O_3-α, even though the impregnation method was altered.

Pair (#)	$A_{zeolite}$	Expected A_{Al2O3}	Comparable Activity
1	5%Ni/5A/Cit/EIM	5%Ni/Al_2O_3-α/Cit/EIM	$A_{Zeolite}<A_{Al2O3}$
2	5%Ni/13X/Cit/EIM	5%Ni/ Al_2O_3-ɣ/Cit/EIM	$A_{Zeolite}\sim A_{Al2O3}$
3	5%Ni/L/Cit/EIM		$A_{Zeolite}\sim A_{Al2O3}$ (<320 °C)
4	5%Ni/13X/Cit/FIM	5%Ni/ Al_2O_3-ɣ/Cit/FIM	$A_{Zeolite}>A_{Al2O3}$
5	5%Ni/L/Cit/FIM		$A_{Zeolite}<A_{Al2O3}$

Table 6. 3: The expected comparable pore structure between the impregnated zeolitic and Al_2O_3 supports.

TPR: Identifying catalyst location by reduction peaks

- Peak Intensity: All EIM sample's reduction peaks are more intense than the FIM samples. Even though the drop in FIM nickel content was smaller (20-50% wrt. EIM samples). It suggests a different reduction mechanism is governing at lower loaded Ni-catalyst on the zeolite. It may also be that the nickel present inside the zeolite structure is difficulty reached by H_2.
- Location dependent peaks: FIM samples only have one minor peak corresponding to catalyst present within the zeolite structure while the EIM samples have two major peaks corresponding to catalyst present outside and inside the zeolite structure.

In the Sabatier setup, the activities between regular and cleaned BM were compared, by the distinct activity test.

Activity Test:

- Overall activity: The order of the activity curves is 5%Ni/13X/Cit/EIM > 5%Ni/L/Cit/EIM > 5%Ni/5A/Cit/EIM ~ 5%Ni/13X/FIM > 5%Ni/5A/Cit/FIM ~ 5%Ni/L/Cit/FIM. Here, the EIM samples performed better than the FIM samples by a significantly higher nickel content.
- Effective activity: From all samples, only the 5%Ni13X/Cit/FIM and 5%Ni5A/Cit/FIM have a high conversion per gram catalyst. These make it interesting for higher target loading zeolites for future research.

Selectivity

- Overall selectivity: Generally, It is observed that EIM samples are more selective to CH_4. On the other hand, FIM samples are more selective to CO as the temperature rises. It is proposed that FIM samples have smaller H_2 coverage resulting in rapid CO production. In comparison with EIM samples possessing more active H_2 sites leading to higher coverage thus favouring CH_4 production.
- Order of selectivity: Also, an order of CH_4 selectivity for FIM samples are identified which are the inverse order for the CO selectivity as expected. It may be that the 13X support is an active material during Sabatier reaction and the L for CO RWGS while the 5A is between them for CH_4 and CO selectivity [1].

Activity comparison based on pore structure: Overall, similar-looking pore structures between the zeolite and Al_2O_3 support do not lead to comparable activity. From them only 5%Ni/13X/Cit/EIM is represented by the correct Al_2O_3 support and the 5%Ni/L/Cit/EIM for T <320 °C.

6.2. Recommendation

For future research some recommendations are found throughout this thesis:

Additional zeolite L characterization:

- The zeolite L had an activity between the 13X and 5A in the activity test which could not be explained properly. To understand this observation better, an NH_3-TPR should be carried out for fresh and impregnated zeolite L explaining the BM-CO_2 interaction. When high amounts of acidity is observed, like the 5A, then the placement of L between 13X and 5A are justified.
- The N_2 physisorption was lacking for the zeolite L displaying the volume reduction upon impregnation.
- All samples were at reduced at 400 °C while the H_2-TPR displayed peaks at higher temperatures (400-500 °C). So, calcining at these peaks, with the condition of being below the zeolite deterioration temperature, may produce more nickel oxides leading to higher activities.

Cleaned BM sorption enhanced methanation test:

The cleaned BM did not undergo the sorption enhanced methanation test within this thesis due to time constraint. These samples seem promising as it effective activity (conversion/mass catalyst) were high indicating to reach high activities, especially for 5%Ni/13X/Cit/FIM and 5%Ni/5A/Cit/FIM at lower temperatures (At higher temperatures CH_4 selectivity decreases).
This could be interesting if, for instance, the catalyst is loaded higher before treated with FIM, so a nickel loading of 5wt% is achieved, ready for comparison with the EIM samples.

Further analysis regarding sorption enhanced methanation tests:

- Generally, as the temperature is raised during the sorption enhanced methanation test, the H_2 breakthrough decreases. However, the 5A trends inversely, showing a longer H_2 breakthrough at higher temperatures. This may be caused by not fully desorbing water after 2h regeneration at 1 bar operating pressure which is too high (or too low regeneration temperature). To validate the water-zeolite interaction strength, isostere graphs should be generated as the relationship between temperature and water partial pressure may explain this phenomenon.
- The zeolite L did not undergo sorption enhancement. It may be that the water particle pressure is below the zeolite L equilibrium pressure, so water could not be adsorbed. Also for this zeolite, isostere graphs should be generated.
- The regeneration temperature was set for 450 °C, but it has not been empirically determined. Therefore, the thermogravimetric analysis could be conducted to find the best regeneration temperature at a fixed pressure.

Bibliography

[1] Y.A. Daza and J.N. Kuhn, CO_2 conversion by reverse water gas shift catalysis: comparison of catalyst mechanisms and their consequences for CO_2 conversion to liquid fuels. The Royal Society of Chemistry 2016.

[2] H. Ritchie M. Roser and E. Ortiz-Ospina. World population growth. https:// ourworldindata.org/world-population-growth, 2013. [Online; accessed 2019-0730].

[3] S. Bilgen. Structure and environmental impact of global energy consumption. Renewable and Sustainable Energy Reviews, 33:890, 2014.

[4] bp. Bp statistical review of world energy. https://www.bp.com/en/global/ corporate/energy-economics/statistical-review-of-world-energy.html, 2017. [Online; accessed 2019-08-13].

[5] Vaclav Smil. Energy transitions: Global and national perspectives, 2017.

[6] H. Ritchie M. Roser. Energy production changing energy sources. https: //ourworldindata.org/energy-production-and-changing-energy-sources, 2017. [Online; accessed 2019-07-30].

[7] United Nation. World population projected to reach 9.7 billion by 2050. www.un. org/en/development/desa/news/population/2015-report.html, 2015. [Online; accessed 2019-07-30].

[8] D. Ciolkosz. What is renewable energy? https://extension.psu.edu/ what-is-renewable-energy, 2009. [Online; accessed 2019-07-30].

[9] INSTITUTION OF OCEANOGRAPHY. Institution of Oceanography, 2015.

[10] D. Kariuki. Barriers to renewable energy technologies development. https://www.energytoday.net/economics-policy/ barriers-renewable-energy-technologies-development/, 2018. [Online; accessed 2019-08-12].

[11] M.r Shaner et al. Geophysical constraints on the reliability of solar and wind power in the united states. Energy and Environmental Science pages 914–925, 2018.

[12] CBS. Energieverbruik particuliere woningen; woningtype en regio's. https: //opendata.cbs.nl/statline/#/CBS/nl/dataset/81528NED/table?fromstatweb/, 2019. [Online; accessed 2019-08-13].

[13] California Hydrogen Business Council. Power-to-gas: The case for hydrogen white paper, 2015.

[14] D.Berg et al. Breaking the balance, 2018.

[15] Uniongas. Chemical composition of natural gas. https://www.uniongas.com/ about-us/about-natural-gas/Chemical-Composition-of-Natural-Gas., 2018. [Online; accessed 2019-08-13].

[16] L.D. Schmidt. The engineering of chemical reactions, 1997.

[17] M.C. Bacariza, I.Graca, J.M. Lopes & C. Henriques, Enhanced activity of CO2 hydrogenation to CH4 over Ni-based zeolites through the optimization of the Si/Al ratio. Microporous and mesoporous materials 267 (2018) 9-19

[18] L. Wei, W. Haije, N. Kumar, J. Peltonen, M. Peurla, H. Grenman & W. de Jong, The influence of nickel precursors on the properties and performance of Ni impregnated zeolite 5A and 13X supported catalysts in CO2 methanation, submitted manuscript, 2019.

[19] L. Wei. personal communication. 2019.

[20] S.T. Misture & R.L.Snyder. Encyclopedia of Materials: Science and Technology,Second Edition, Pages 9799-9808, 2001.

[21] Scott A Speakman, PhD Massachusetts Institute of Technology. Introduction to X-ray Powder Diffraction Data.
analysishttp://prism.mit.edu/xray/introduction%20to%20xrpd%20data%20analysis.pdf, 2019.

[22] G. Granitsiotis. Methanation of carbon dioxide. 2017.

[23]frcrphysicsnotes. Production of X-rays.
https://sites.google.com/site/frcrphysicsnotes/production-of-x-rays, 2020. [Online; accessed 2020-03-18].

[24] A. V. Kolpakov, Mosleys Law. https://encyclopedia2.thefreedictionary.com/Moseley%27s+Law, 2020. [Online; accessed 2020-02-27]

[25] D.H. Olson CH.Baerlocher, L.B.McCusker. Atlas of zeolite framework types. page 1, 2007. [Online; accessed 2019-08-27].

[26] Structure Commission of the International Zeolite Association. Database of zeolite structures. https://europe.iza-structure.org/IZASC/ftctable.php, 2017. [Online; accessed 2019-08-27]

[27] IZA Structure Commission. News from the structure commission. http://www.izastructure.org/, 2019. [Online; accessed 2019-08-30].

[28] F.Zhang G.R.North, J.C.Pyle. Encyclopedia of atmospheric sciences, 2015.

[29] V. Valtchev. Companies that use, produce or characterize zeolites.
http://www.izaonline.org/ZeoliteComp.htm. [Online; accessed 2019-08-30].

[30] J.B.Higgens K.D. Schmitt. Zsm-10: synthesis and tetrahedral framework structure. 1996.

[31] W. Haije. personal communication. 2019.

[32] T. Ban G. Calzaferri A.Z Ruiz, D. Br˜A¼hwiler. Synthesis of zeolite l. tuning size and morphology. 2004.

[33] CRC handbook of chemistry and physics 85th edition, 2005.

[34] P.A. Cox C.S. Cundy. The hydrothermal synthesis of zeolites: Precursor, intermediate and reaction mechanism. Microporous and mesoporous materials 82, 1-7, page 10.

[35] X-ray fluorescence spectroscopy (XRF). http://www.bedwani.ch/xrf/xrf_1/xrf.htm, 2020.

[36] K.Rangsriwatananon & W.Insuwan. Morphology-controlled synthesis of zeolite L and physicochemical properties. Engineering journal.

[37] J.Singh & S. Chaturvedi. IIT JEE Physics. https://www.concepts-of-physics.com/modern/moseleys-law.php, 2020. [Online; accessed 2020-03-28].

[38] H. C. Wu, Y. C. Chang, J. H. Wu, J. H. Lin, I. K. Linc and C. S. Chen, Methanation of CO2 and reverse water gas shift reactions on Ni/SiO2 catalysts: the influence of particle size on selectivity and reaction pathway

[39] Chemistry libretexts.
https://chem.libretexts.org/Courses/Franklin_and_Marshall_College/Introduction_to_Materials_Characterization_-_CHM_412_Collaborative_Text/Spectroscopy/Energy-Dispersive_X-ray_Spectroscopy_(EDS), 2020. [Online; accessed 2020-03-28].

[40] Scanning Electron Microscopy (SEM/EDS). http://blog.sina.com.cn/s/blog_4a9e8f1e0102wuc3.html ,2020. [Online; accessed 2020-03-28].

[41] Anderson Materials Evaluation, Inc http://www.andersonmaterials.com/sem/sem-secondary-backscatter-images.html ,2020. [Online; accessed 2020-03-28].

[42] Vrije Universiteit Brussel, Electrochemical and surface engineering. https://www.surfgroup.be/semedx, 2020. [Online; accessed 2020-03-28].

[43] Light versus Electron Microscopes. https://ib.bioninja.com.au/standard-level/topic-1-cell-biology/11-introduction-to-cells/microscopes.html, 2020. [Online; accessed 2020-03-28].

[44] Ludwig Maximilian University of Munich. Faculty for physics. Condition for the constructive interference of waves from a crystal film. https://www.didaktik.physik.uni-muenchen.de/elektronenbahnen/en/elektronenbeugung/einfuehrung/bragg-bedingung.php ,2019. [Online; accessed 2019-08-30].

[45]Linde gas, Thermal conductivity detector. http://hiq.lindegas.com/en/analytical_methods/gas_chromatography/thermal_conductivity_detector.html,2019. [Online; accessed 2019-08-30].

[46] S. Walspurger, G.D. Elzinga, J. W. Dijkstra, M. Saric & W.G. Haije, Sorption enhanced methanation for substitute natural gas production: Experimental results and thermodynamic considerations. Chemical Engineering Journal 242, 379-386, 2014

[47] K. Ghaib, K. Nitz, and F.-Z. Ben-Fares, Chemical methanation of CO_2: a review, Chem BioEng Reviews 3, 266 (2016)

[48] I. Graça, L.V. González, M.C. Bacariza, A. Fernandes, C. Henriques, J.M. Lopes, M.F. Ribeiro, CO2 hydrogenation into CH_4 on NiHNaUSY zeolites, Applied Catalysis B: Environmental, 147 (2014) 101-110.

[49] A. Luengnaruemitchai, A. Kaengsilalai, Activity of different zeolite-supported Ni catalysts for methane reforming with carbon dioxide, Chem Eng J, 144 (2008) 96-102

[50] M. Suzuki, K. Tsutsumi, H. Takahashi, Characterization and catalytic activity of nickel-zeolite catalysts. I. Reduction properties of nickel ions in zeolites, Zeolites, 2 (1982) 51-58.

[51] Bob B. He. Two-Dimensional X-Ray Diffraction. Wiley. 2009

[52] B.L. Dutrow & C.M. Clark. X-ray Powder Diffraction (XRD). https://serc.carleton.edu/research_education/geochemsheets/techniques/XRD.html, 2019. [Online; accessed 2019-08-30].

[53] HiddenAnalytics. https://www.hidenanalytical.com/what-is-tpr/ ,2019. [Online; accessed 2019-08-30].

[54] SEM department P&E, TUDelft. personal communication. 2019.

[55] F. Ibis, Responsible for XRD equipment, TUDelft. personal communication. 2019.

[56] L. Rohrbach, Responsible for the TPR, Rijksuniversiteit Groningen. personal communication. 2019.

Appendices

A.1 Zeolite Table

Zeolite framework [26]	FAU	LTA	LTL
Zeolite material	13X	4A/5A	L
Molecule formula	$\|(Ca^{2+},Mg^{2+},Na_2^{+})_{29}(H_2O)_{240}\|[Al_{58}Si_{134}O_{384}]$	$\|Na_{12}^{+}(H_2O)_{27}\|_8[Al_{12}Si_{12}O_{48}]_8$	$\|K_9^{+}(H_2O)_{21}\|[Al_9Si_{27}O_{72}]$
Total cation charge	174	96	189
Pore limiting diameter (Å)	6,7	4.1/4,9	8,1
Si/Al ratio	2.3	1	3
Accessible area (m^2/g)	1211.42	1204.87	694.6
Accessible volume (%)	27.42	21.43	15.37
organic/inorganic	Inorganic	Inorganic	Inorganic
Acidity and basicity	Basic	Acidic	Acidic

Table A. 1: Zeolite comparison table

A.2 Experiment: Detailed description of zeolite L synthesis

A.2.1. General zeolite synthesis

For the syntheses of zeolite L two products are prepared separately, an aluminium oxide containing product namely A and silicon oxide (silica) containing product named B. Afterwards these 2 products are mixed for the actual zeolite synthesis under higher pressures see figure A.1 below.

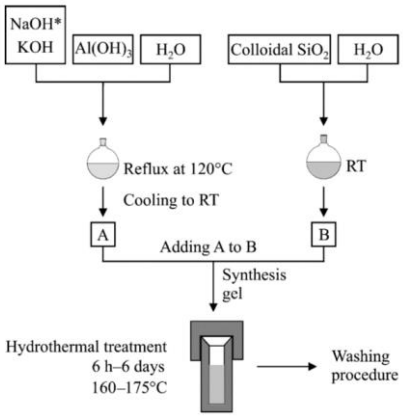

Figure A.1: The general scheme of the zeolite L synthesis procedure [32]

For **24 to 32 grams of zeolite L crystals,** a **gel of 140 ml** is needed, which **fills almost half the autoclave (293 ml)** present at the P&E lab. The required molar gel composition derived from K.Rangsriwatananon et al. is found in table A.2 below [36].

Starting gel composition in oxides scaled ½ volume autoclave					
Chemical	K_2O	Al_2O_3	SiO_2	H_2O (L) (to be added)	total
N (mol)	0.12	0.05	0.45	7.20	-
m (gram)	11.11	4.59	27.04	129.71	172.44

Table A. 2: The starting gel composition expressed in oxides, scaled for the autoclave.

A.2.2. Correction for available reactants

As in table A.2, the compounds are expressed in oxides. But Ban et al. 'translates' compounds in easier available chemicals as solid potassium hydroxide (KOH, Sigma Aldrich, Purity >99%), solid aluminium hydroxide ($Al(OH)_3$, >99%, Sigma Aldrich) and a colloidal suspension of silica (SiO_2, 40 wt% suspension H_2O, Sigma Aldrich). Due to these changes' corrections are made regarding the water content originating from the new starting compounds which will be subtracted from the *'total water to be added'* in the coming paragraphs. (found in the third column in table A.2).

1.1. K_2O translating in KOH

Instead of potassium oxides, KOH powder is used in the recipe. KOH decomposed into K_2O and water see equation A.1.

Results in adding **13.23 grams of KOH** and **subtracting 2.12 ml water** from 'the total water added' per **6.62 grams of K_2O** see table A.3 below.

$$2\ KOH(s) \rightarrow K_2O + H_2O\ (l) \qquad (A.1)$$

Chemical	2 KOH (s)	-->	1 K_2O	+	1 H_2O (L)
N (mol)	0.24	-	0.12	-	0.12
m (gram)	13.23	-	6.62	-	2.12

Table A. 3:Calculation of the amounts of KOH and water per stochiometric required potassium oxide.

1.2. Al_2O_3 translating in $Al(OH)_3$

Instead of aluminium oxides, $Al(OH)_3$ powder is used in the recipe. $Al(OH)_3$ decomposed into Al_2O_3 and 3 water molecules see equation A.2 below.

These adjustments result in adding **7.02 grams of $Al(OH)_3$** and **subtracting 2.43 ml water** from 'the total water added' per **4.59 grams of Al_2O_3** see table A.4 below.

$$2\ Al(OH)_3\ (s) \rightarrow Al_2O_3 + 3\ H_2O\ (l) \qquad (A.2)$$

Chemical	2 $Al(OH)_3$ (s)	-->	1 Al_2O_3	+	3 H_2O (L)
N (mol)	0.09	-	0.05	-	0.14
m (gram)	7.02	-	4.59	-	2.43

Table A. 4: Calculation of the amounts of $Al(OH)_3$ and water per stochiometric required aluminium oxide.

1.3. Purity correction SiO_2 into AS-30

Due to a lack of a mixer with an rpm of 18000 min-1, solid SiO_2 could not be used. Therefore, pretreated SiO_2 dissolved in water named 'AS-30 Colloidal Silica' is purchased. For the prescribed **27.04 g of SiO_2** from table 1 and a 30wt.% purity, **90.12 ml AS-30** (or 74.48 grams, density = 1.21 g/ml) is needed for the experiment. Moreover, **63.08 ml water is subtracted** for 'the total water added' see table A.5 below.

AS-30 colloidal Silica			
	wt.%	m (g)	V (ml)
SiO2	30%	27.04	-
water	70%	63.08	63.08
AS-30	100%	90.12	74.48

Table A. 5:Calculation of the amounts of AS-300 and water per stochiometric required silica oxide.

1.4. Corrected starting gel composition

All the oxides expressed chemicals K_2O, Al_2O_3 and SiO_2 in table 1 are translated into KOH, $Al(OH)_3$ and AS-30. These corrections are found in tables 2,3 &4 and incorporated into table 1 resulting table 5 below. *Table A.6 will be used for the Zeolite L synthesis.*

Starting gel composition in usable chemicals scaled ½ volume autoclave					
Chemical	KOH (s)	Al(OH)3 (s)	AS-30(L)	H2O (L) to be added	total
N (mol)	0.24	0.09	-	5.26	-
m (gram)	13.23	7.02	90.12	62.07	172.44
V (ml)	-	-	74.48	62.07	141.11

Table A. 6: The corrected starting gel composition expressed in non-oxides that is used for the zeolite L synthesis.

A.2.3. Recipe

Step 1: Dissolving aluminium in water (Product A)

Overall: $Al(OH)_3$ is dissolved in deionized water in a reflux setup (higher temperatures → higher solubility). To promote dissolving a basic environment is created by KOH.

1. Weight on a measuring paper **15.56 g KOH powder/pellets** (13.23 *g pure KOH).*
    - KOH is used to create a basic environment for **deprotonation** of $Al(OH)_3$ into Al_2O_3**.** The deprotonation is found in equation A.3 below.

$$Al(OH)_3\,(s) + 3\,OH^-(aq) \rightarrow {AlO_3}^{-3} + 3\,H_2O(l) \qquad (A.3)$$

2. Weight on a measuring paper **7.09 g $Al(OH)_3$ powder** *(7.02 g pure $Al(OH)_3$).*
3. Fill a graduated cylinder (maatcilinder) with **30.52 ml deionized water**
4. Put a 200 ml beaker with a magnetic stirrer on a scale (weegschaal) and set it to zero.
5. Fill the 200 ml beaker with the measured deionized water (from step 3).
6. **Put KOH powder** into **the 200 ml beaker filled with deionized water** while magnetically stirring.
    - Prevent salts from sticking on the glass by putting small amounts of powder in the beaker.
    - The dissolution reaction is found in equation A.4 below [33]:

$$KOH(s) \rightarrow K^+(aq) + OH^-(aq) \qquad \Delta H_{sol} = -57.61\frac{\text{kJ}}{\text{mol}} \qquad (A.4)$$

7. Stir it till a clear solution is visible (solubility KOH = 53.2 g/100 ml at 20 °C) [33]
8. **Put $Al(OH)_3$ powder** into the **200 ml beaker with the dissolved KOH in deionized water** while magnetically stirring.
    - Prevent salts from sticking on the glass by putting small amounts of powder in the beaker.
    - $Al(OH)_3$ dissolves very little at room temperature in demi water (0.0001 g/100 ml) **but in a basic environment, aluminium hydroxide reacts to aluminate ions which will aggregate with water, K^+ and OH^-.** So, an opaque mixture is observed. [33]
9. Weight on the calibrated scale (Step 4) how much water is evaporated due to the KOH dissolution. **Theoretically, 3.8 ml water is evaporated** so **expected is to measure 103.26 g**.
    - This step is after putting all the salts in order to flush the salt still sticking on the walls.
10. Add the measured water difference into the beaker filled with the opaque mixture.
11. Put the opaque mixture into a 1000 ml round bottom flask and heat the mixture under atmospheric pressures till boiling point (approaching 120 °C is ideal). The volume of **product A** is estimated to be around **36 ml.**

12. keep it for 3 hours to forcefully dissolving the $Al(OH)_3$ in the basic environment. The following energy input in equation A.5 and reaction in equation A.6 will take place:

$$2.026\ \frac{bara}{s} * \frac{10^5 Pa}{1\ bara} * \frac{N}{m^2 * Pa} * \frac{J}{N * m} * 0.3L * \frac{1\ m^3}{1000\ L} * \frac{s * W}{J} = 60.78\ W \qquad (A.5)$$

$$60.78\ W + Al(OH)_3\ (s) + 3\ OH^-(aq) \rightarrow {AlO_3}^{-3} + 3\ H_2O(l) \qquad (A.6)$$

13. Cool the clear basics solution to room temperature. (if a clear solution is observed, the purpose of product A synthesis is reached)
14. Check the acidity is (should be pH>7)

Step 2: SiO_2 suspension (Product B)

Overall: Stir the silica source

1. Pour the 74.48 ml of AS-30 in a graduated cylinder (maatcilinder)
2. Pour the AS-30 in a 200 ml beaker
3. Magnetically stir it for 10 min *before starting 'mix A+B'.*

Step 3: Mix A +B

Overall: Mix the aluminium-source (A) and silica source (B) before zeolite crystallization.

1. Put the 300 mL liner of the autoclave on a magnetic stirring machine.
2. Pour product A including the Teflon stirrer (Teflon decomposes at 320 °C) in the 300 ml Liner.
3. Add product B and **25.94 ml remaining deionized water** to the 300 ml Liner filled with product A under **vigorous stirring**.
4. Continue stirring till a homogeneous opaque (ondoorzichtig) gel is observed. The purpose is to uniformly distribute the particles, so you can't see the different phases.

Step 4: Crystallization of gel

Overall: The gel with silica and aluminium are formed into the desired zeolite

1. Use fat on the threads of the autoclave so it will not be damaged during closing and opening.
2. Put the liner into the autoclave and close it (ask someone for help during closing).
3. Heat the autoclave to **T=180 °C** (using steam tables = **6.2 bara) with steps of 1 °C/min**[8].
4. Keep the **temperature of 180 °C for 48h without agitation** in order to form the interested zeolite. See equation A.7 below for the reaction.

$$27\ {K_2SiO_4}^{-2} + 9\ {KAlO_4}^{-4} + 93\ H_2O \rightleftharpoons 54\ K^+ + 144\ OH^- + |{K_9}^+(H_2O)_{21}|[Al_9Si_{27}O_{72}] - LTL \qquad (A.7)$$

Step 5: After crystallization (separation the crystals)

Overall: Wet zeolite is dried, and ion exchange will take place

1. Cool the pressure vessel/autoclave in water before opening. → (relieving the pressure)
2. Wash the product with distilled water till it is near pH = 7 in a Buchner funnel vacuum filter.
3. Dry the crystals for **overnight at T= 80 °C**. Eventually yielding theoretically between **24 to 34 grams of the product**
4. Dry crystals in the stove for **16h at T=80 °C**

[8] Maximum allowable heating rate is 5 °C/min

B.1 Calculation Chemical Equilibrium Conversion

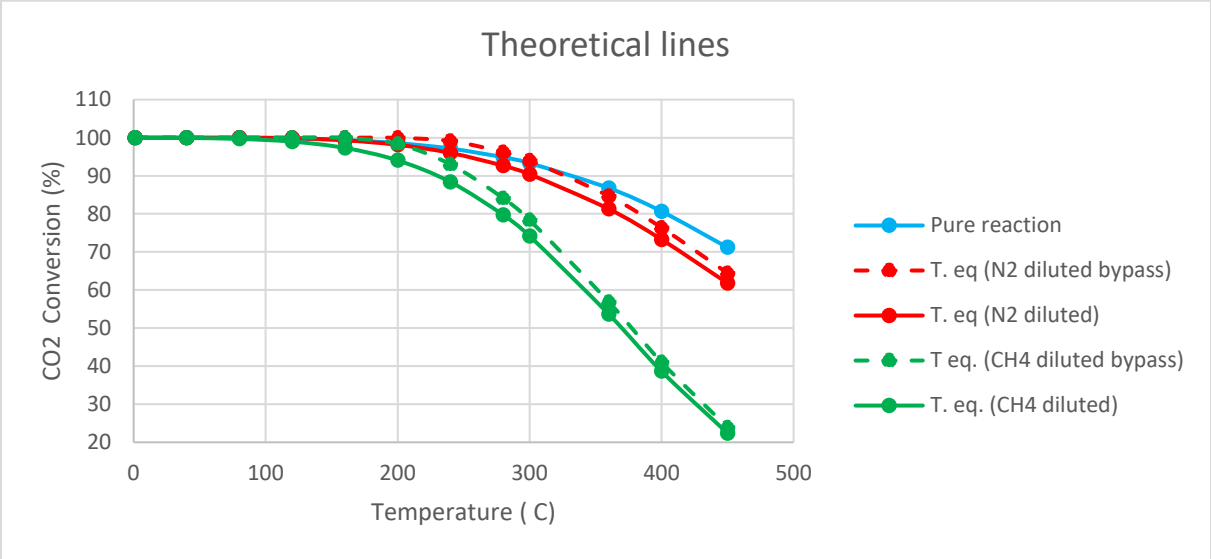

Figure B. 1: All the various theoretical equilibrium lines are plotted. Generally, the more diluted the feed mixture, the lower the T.eq conversion. Due to circumstances in Q1/2020, no bypass experiment was carried out for 'N_2 diluted'. Therefore, a correction factor is used between "CH_4 diluted" and "CH_4 diluted bypass" resulting in an undesired slight overshoot above the pure reaction (200-300 °C).

B.1.1. Sabatier reaction: Pure reaction

	CO_2	4 H_2	⇌	CH_4	2 H_2O	Total
Initial	1	4	-	0	0	-
Change	-x	-4x	-	+x	+2x	-
Final	1-x	4-4x	-	+x	+2x	**5-2x**

Table B.1: The stochiometric table of the Sabatier reaction (pure reaction

$$K_{eq} = \frac{y_{CH_4}\, y^2{}_{H_2O}}{y_{CO_2}\, y^4{}_{H_2}} * \left(\frac{P_{tot}}{P_{ref}}\right)^{-2} = \frac{\frac{x}{5-2x}\left(\frac{2x}{5-2x}\right)^2}{\frac{1-x}{5-2x}\left(\frac{4-4x}{5-2x}\right)^4} * \left(\frac{P_{tot}}{P_{ref}}\right)^{-2}$$

Equation B.1: The general equilibrium equation of the Sabatier reaction

Sabatier reaction: Diluted in N_2

	CO_2	4 H_2	⇌	CH_4	2 H_2O	N_2	Total
Initial	1	4.0162	-	0	0	14.5041	-
Change	-x	-4x	-	+x	+2x	-	-
Final	1-x	4.0162-4x	-	+x	+2x	14.5041	**19.5203-2x**

Table B. 2: The stochiometric table of the Sabatier reaction diluted in N_2

$$K_{eq} = \frac{y_{CH_4}\, y^2{}_{H_2O}}{y_{CO_2}\, y^4{}_{H_2}} * \left(\frac{P_{tot}}{P_{ref}}\right)^{-2} = \frac{\frac{x}{19.5203-2x}\left(\frac{2x}{19.5203-2x}\right)^2}{\frac{1-x}{19.5203-2x}\left(\frac{4.0162-4x}{19.5203-2x}\right)^4} * \left(\frac{P_{tot}}{P_{ref}}\right)^{-2}$$

Equation B 2: The equilibrium equation of the Sabatier reaction taking the N_2 dilution into account

Sabatier reaction: Diluted in N_2 - Corrected by the bypass

	CO_2	4 H_2	⇌	CH_4	2 H_2O	N_2	Total
Initial	1	4.2340	-	0	0	15.1272	-
Change	-x	-4x	-	+x	+2x	-	-
Final	1-x	4.2340 -4x	-	+x	+2x	15.1272	**20.3613-2x**

Table B. 3: The stochiometric table of the Sabatier reaction diluted in N_2 and corrected by the bypass (derived correction factor between 'CH_4 diluted' and 'CH_4 diluted bypass')

$$K_{eq} = \frac{y_{CH_4}\, y^2{}_{H_2O}}{y_{CO_2}\, y^4{}_{H_2}} * \left(\frac{P_{tot}}{P_{ref}}\right)^{-2} = \frac{\frac{x}{20.3613-2x}\left(\frac{2x}{20.3613-2x}\right)^2}{\frac{1-x}{20.3613-2x}\left(\frac{4.2340\ -4x}{20.3613-2x}\right)^4} * \left(\frac{P_{tot}}{P_{ref}}\right)^{-2}$$

Equation B 3: The equilibrium equation of the Sabatier reaction taking the N_2 dilution and bypass into account

Sabatier reaction: Diluted in CH_4

	CO_2	4 H_2	⇌	CH_4	2 H_2O	N_2	Total
Initial	1	4.0587	-	32.8374	0	2.3053	-
Change	-x	-4x	-	+x	+2x	-	-
Final	1-x	4.0587-4x	-	32.8374+x	2x	2.3053	**40.1427-2x**

Table B. 4: The equilibrium equation of the Sabatier reaction taking the CH_4 dilution into account

$$K_{eq} = \frac{y_{CH_4}\, y^2{}_{H_2O}}{y_{CO_2}\, y^4{}_{H_2}} * \left(\frac{P_{tot}}{P_{ref}}\right)^{-2} = \frac{\frac{32.8374+x}{40.1427-2x}\left(\frac{2x}{40.1427-2x}\right)^2}{\frac{1-x}{40.1427-2x}\left(\frac{4.0587-4x}{40.1427-2x}\right)^4} * \left(\frac{P_{tot}}{P_{ref}}\right)^{-2}$$

Equation B 4: The equilibrium equation of the Sabatier reaction taking the CH_4 dilution into account

Sabatier reaction: Diluted in CH_4 – corrected by bypass

	CO_2	4 H_2	⇌	CH_4	2 H_2O	N_2	Total
Initial	1	4.2788	-	34.1747	0	2.4203	-
Change	-x	-4x	-	+x	+2x	-	-
Final	1-x	4.2788-4x	-	34.1747+x	2x	2.4203	**41.8739-2x**

Table B. 5: The equilibrium equation of the Sabatier reaction taking the CH_4 dilution and bypass into account.

$$K_{eq} = \frac{y_{CH_4}\, y^2{}_{H_2O}}{y_{CO_2}\, y^4{}_{H_2}} * \left(\frac{P_{tot}}{P_{ref}}\right)^{-2} = \frac{\frac{34.1747+x}{41.8739-2x}\left(\frac{2x}{41.8739-2x}\right)^2}{\frac{1-x}{41.8739-2xx}\left(\frac{4.2788-4x}{41.8739-2x}\right)^4} * \left(\frac{P_{tot}}{P_{ref}}\right)^{-2}$$

Equation B 5: The equilibrium equation of the Sabatier reaction taking the CH_4 dilution and bypass into account

B.2 Zeolite L synthesis: Encountered problems

B.2.1. Dissolving poorly soluble alumina sources

Initially, the recipe of G. Calzaferri et al, referred from IZA, for the zeolite L synthesis was conducted [32]. However, the total water distribution was unspecified over the alumina and silica solutions. So, the alumina source was attempted to dissolve in water, which is the difference in the total required water and the water content present in the commercial silica solution. Unfortunately, leading to undissolved $Al(OH)_3$-powder because of low basicity.

Thus, other zeolite L recipes, from C.S. Cundy et al and W.Insuwan et al, were consulted providing the exact water distribution over the 2 solutions [34,36]. The required pH for the alumina solution was respectively 7.7 and 9.3 resulting in the succession of dissolving the $Al(OH)_3$-powder. The remaining water was added during the mixing process of the (already dissolved) alumina and silica solutions.

B.2.2. Pelletizing zeolite L powder

After the filtering and washing the zeolite L powder was acquired. However, this is undesirable for the following reasons:

1. Smaller sized support increases the pressure drop while the setup only operates at atmospheric conditions and unable to form a plug flow.
2. Be comparable with the 13X and 5A zeolites with a sieve fraction ranging between 212-500 mm

Thus, the zeolite L powder where pelletized to a size many times larger than the desired sieve fraction (~20mm). subsequently, the large pellets were crushed till a decent amount (40-55% recovery) with the given sieve fraction were obtained. Both the pelletizing and crushing were successfully executed. The palletization required significantly more effort compared to the crushing step due to the fact, of the fully manual operation of the inhouse pelletizer. Moreover, approximately 60 grams zeolite L powder had to be pressed in batches of ~1 g which made the process also labour-intensive.

C. SEM pictures: Cleaned and regular BM

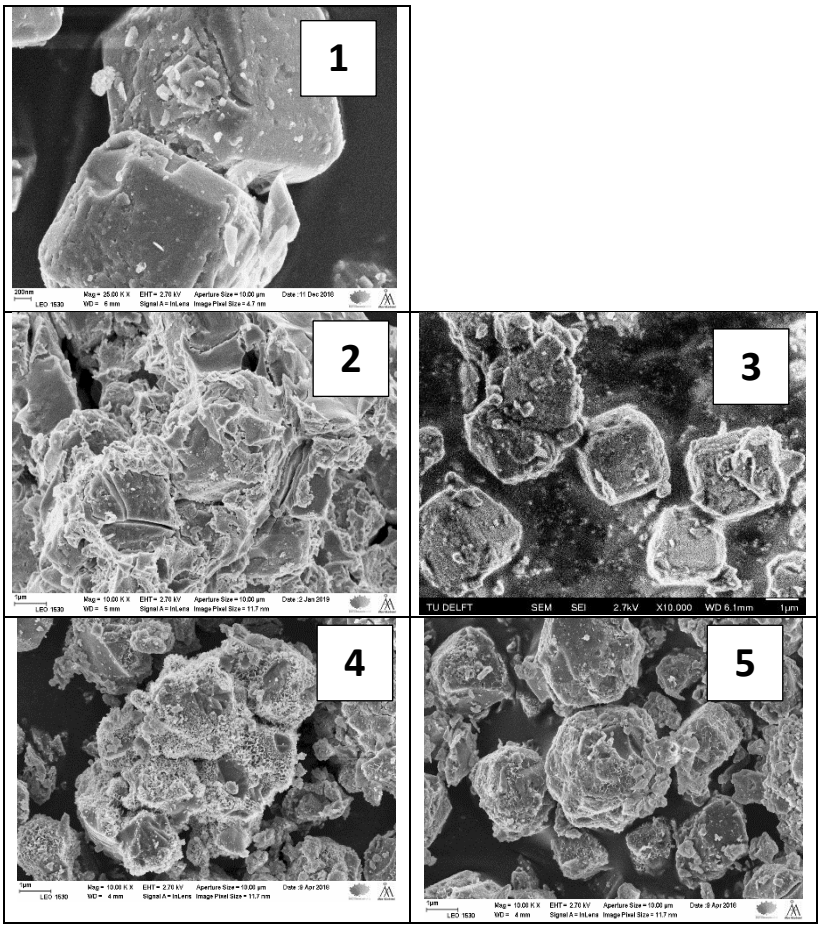

Figure C.1: The SEM pictures of zeolite 5A – Fresh 5A (1) – 5%Ni5A/Cit/EIM (2) -5%Ni5A/Cit/FIM (3) – 5%Ni5A/Nit/EIM (4) - 5%Ni5A/Nit/FIM (5)

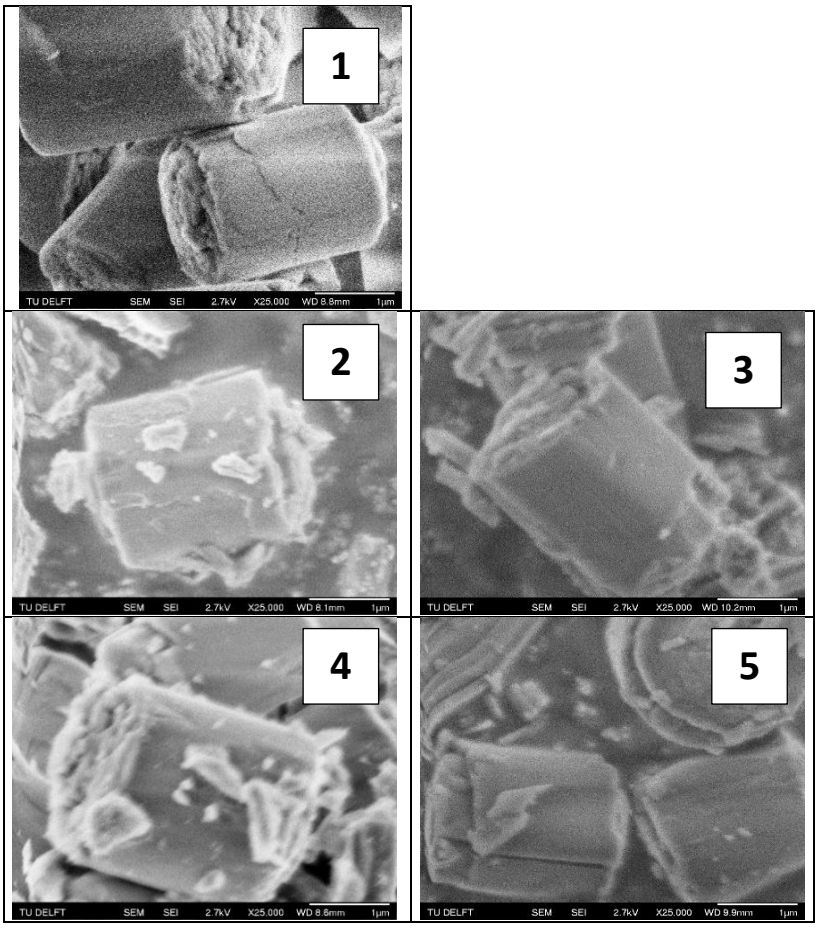

Figure C.2: The SEM pictures of zeolite L – Fresh L (1) – 5%NiL/Cit/EIM (2) -5%NiL/Cit/FIM (3) – 5%NiL/Nit/EIM (4) - 5%NiL/Nit/FIM (5)

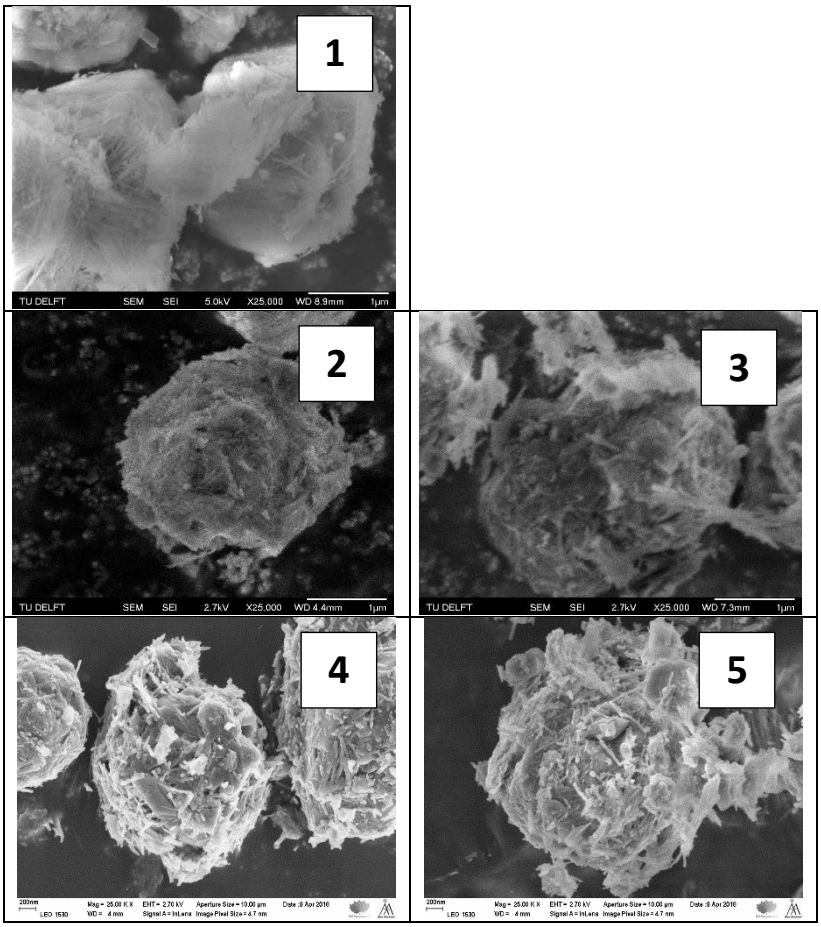

Figure C.3: The SEM pictures of zeolite 13X – Fresh 13X (1) – 5%Ni13X/Cit/EIM (2) -5%Ni13X/Cit/FIM (3) – 5%Ni13X/Nit/EIM (4) - 5%Ni13X/Nit/FIM (5)

D. SEM pictures: zeolitic and Al_2O_3 based support

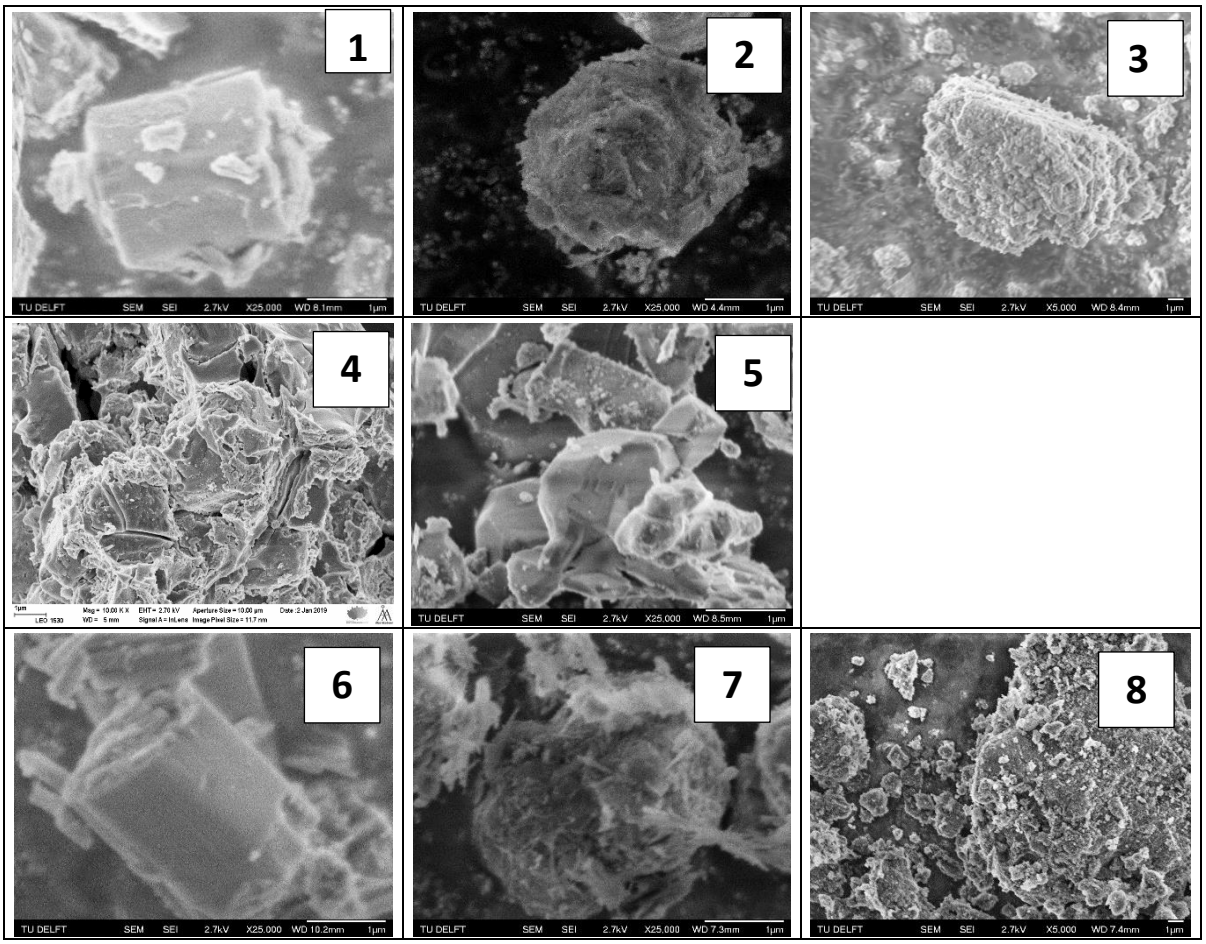

Figure D. 1: The SEM pictures of zeolitic and alumina based support – 5%Ni/L/Cit/EIM (1) – 5%Ni/13X/Cit/EIM (2) - 5%Ni/Al_2O_3-ɣ /Cit/EIM (3) – 5%Ni/5A/Cit/EIM (4)- 5%Ni/Al_2O_3- α/Cit/EIM (5)- 5%Ni/L/Cit/FIM (6) – 5%Ni/13X/Cit/FIM (7) – 5%Ni/Al_2O_3- ɣ /Cit/FIM (8)

E. EDX results

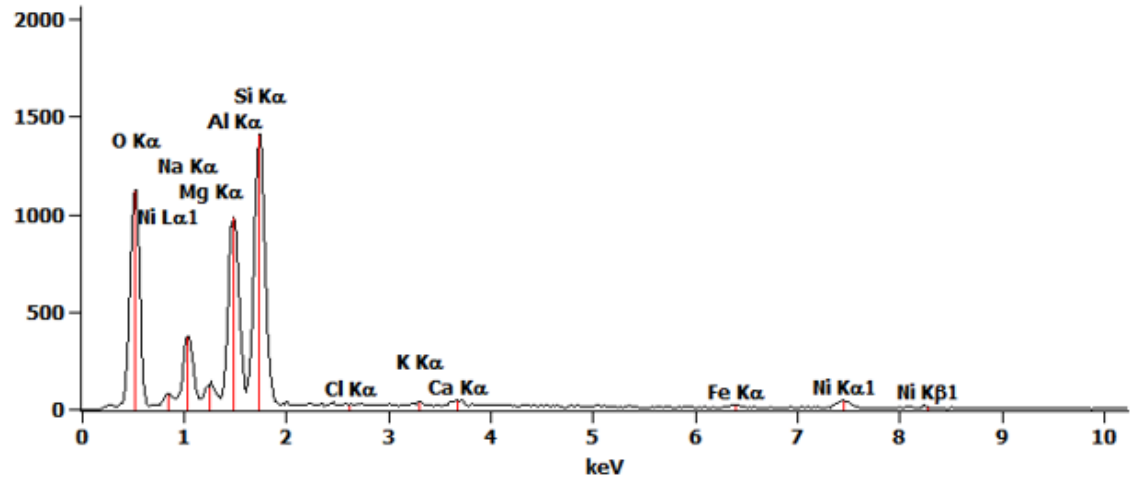

Figure E. 1:One sample of 5%Ni/13X/Cit EDX spectrum.

SAMPLING POINTS #	5%NI/L/NIT/EIM	5%NI/5A/NIT/EIM	5%NI/13X/NIT/EIM
1	5.1 ± 0.63	3.93 ± 0.18	3.16 ± 0.21
2	6.02 ± 0.71	-	-
3	6.33 ± 0.76	-	-
4	6.23 ±0.70	-	-
5	-	-	-
AVERAGE NI WT.% (%)	5.92 ± 0.70	3.93 ± 0.18	3.16 ± 0.21
AVERAGE NI MASS (G)	0.30 ± 0.04	0.20 ± 0.01	0.16 ± 0.01

Table E. 1: EDX results of varying zeolite. Fixed precursor: Ni-Nit. Fixed Impregnation method: EIM.

SAMPLING POINTS #	5%NI/L/CIT/EIM	5%NI/5A/CIT/EIM	5%NI/13X/CIT/EIM
1	5.52 ± 0.53	5.17 ± 0.55	7.37 ± 0.46
2	4.83 ± 0.43	-	6.74 ± 0.77
3	-	-	7.23 ± 0.57
4	-	-	-
5	-	-	-
AVERAGE NI WT.% (%)	5.12 ± 0.48	5.17 ± 0.55	7.11 ± 0.60
AVERAGE NI MASS (G)	0.25 ± 0.02	0.26 ± 0.03	0.36 ± 0.03

Table E. 2:EDX results of varying zeolite. Fixed precursor: Ni-Cit. Fixed Impregnation method: EIM.

F. Individual H_2-TPR results

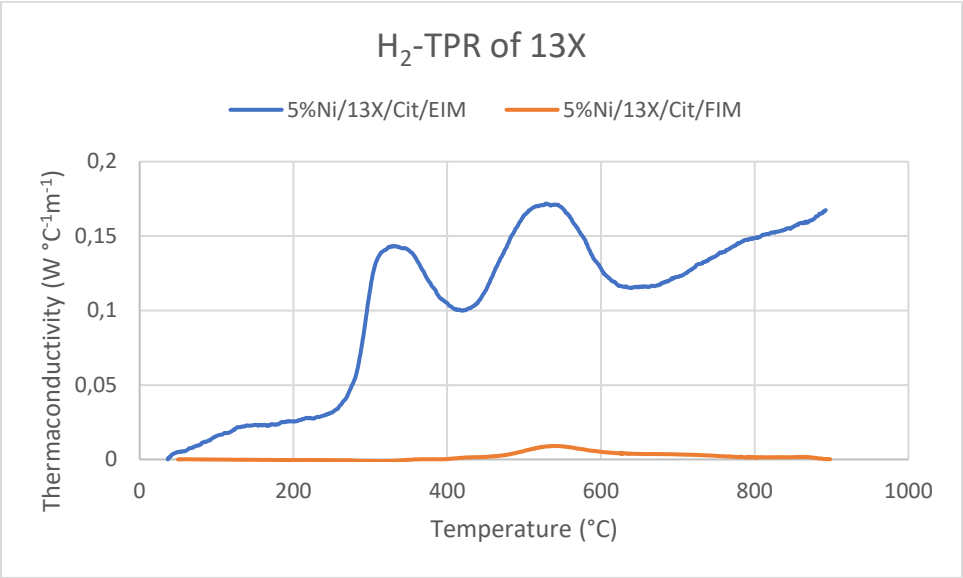

Figure F. 1:H_2-TPR comparison between 13X/EIM and 13X/FIM

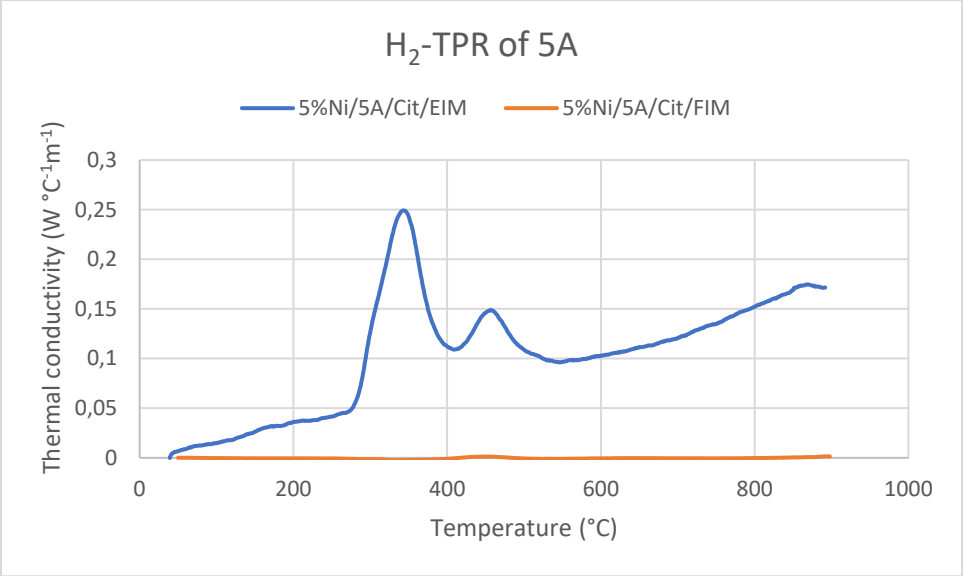

Figure F.2: H_2-TPR comparison between 5A/EIM and 5A/FIM

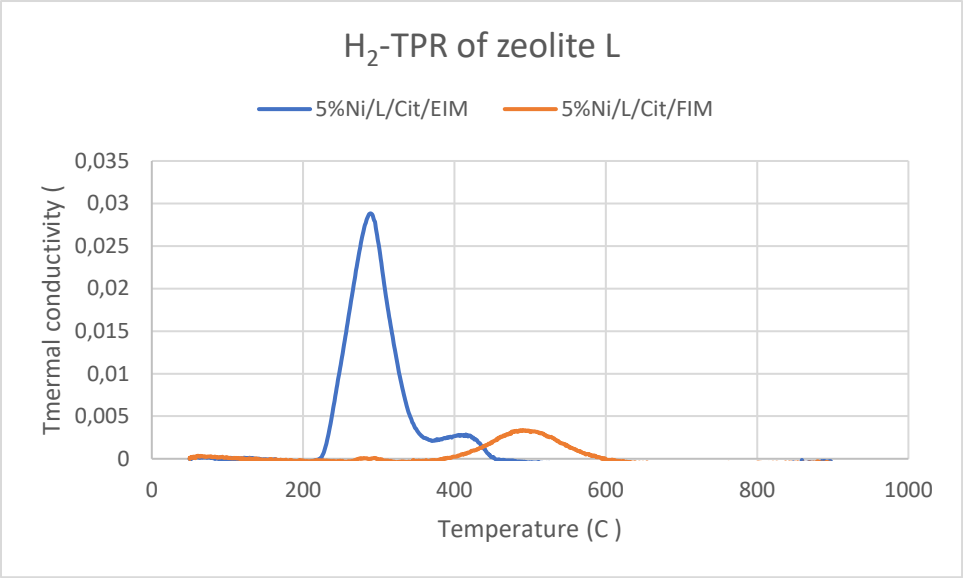

Figure F. 3:H_2-TPR comparison between L/EIM and L/FIM

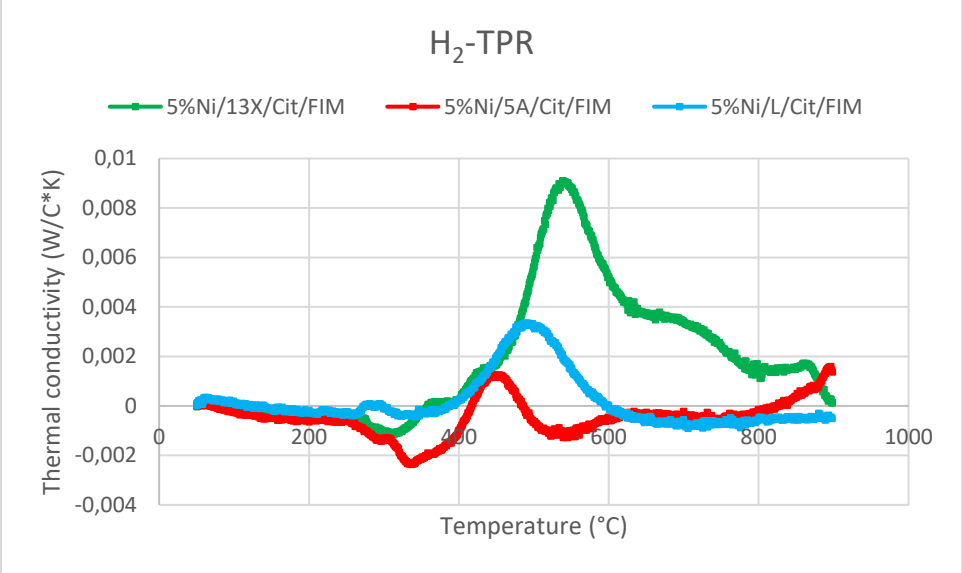

Figure F. 4:H_2-TPR comparison between 13X/FIM, 5A/FIM and L/FIM. The TPR measures negative values, which could be caused by the detector operating at its lower limit resulting in the error.

G. Sorption enhanced experiment detailed program

Sorption enhanced experiment								
Temperature (°C)	Time (min)	N_2	CO_2	H_2	CH_4	CO	heating speed (°C/min) dwelling (min)	
100	0	0	0	100	0	0	5	ramp
450	70	0	0	100	0	0	120	dwelling for reduction 2h
450	190	0	0	100	0	0	5	Ramp
320	216	6	2.5	10	81.5	0	57.0	dwelling for sampling
320	273	90	0	10	0	0	5	Ramp
450	299	90	0	10	0	0	120	dwelling regen1/reduc/regen2
450	419	90	0	10	0	0	5	ramp
300	449	6	2.5	10	81.5	0	57	dwelling for sampling
300	506	90	0	10	0	0	5	ramp
450	536	90	0	10	0	0	120	dwelling regen1/reduc/regen2
450	656	90	0	10	0	0	5	Ramp
280	690	6	2.5	10	81.5	0	57	dwelling for sampling
280	747	90	0	10	0	0	5	Ramp
450	781	90	0	10	0	0	120	dwelling regen1/reduc/regen2
450	901	90	0	10	0	0	5	Ramp
260	939	6	2.5	10	81.5	0	120	dwelling for sampling
260	1059	6	2.5	10	81.5	0	5	Ramp
100	1079	0	0	0	0	0		

Table G. 1: Program/settings Sabatier setup: The furnace controller and mass flow controller.

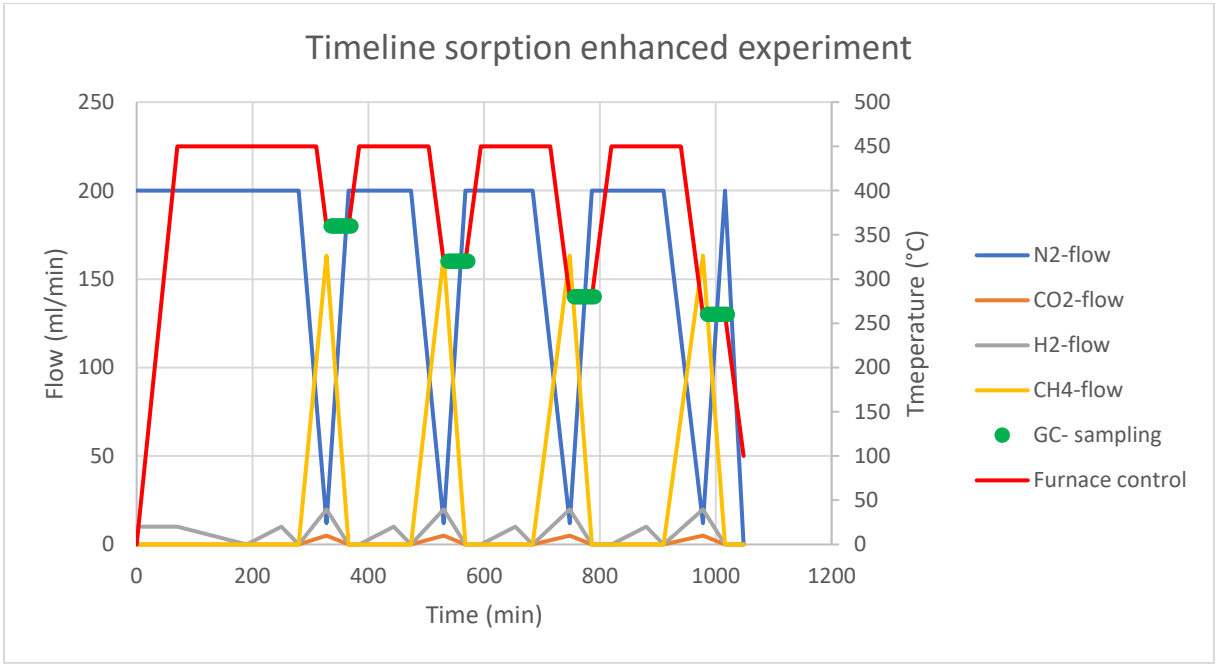

Figure G. 1:Program/settings of the Sabatier setup: GC-sampling, flow - and furnace controller

H. Sorption enhanced methanation GC-results

H.1. Zeolite 13X

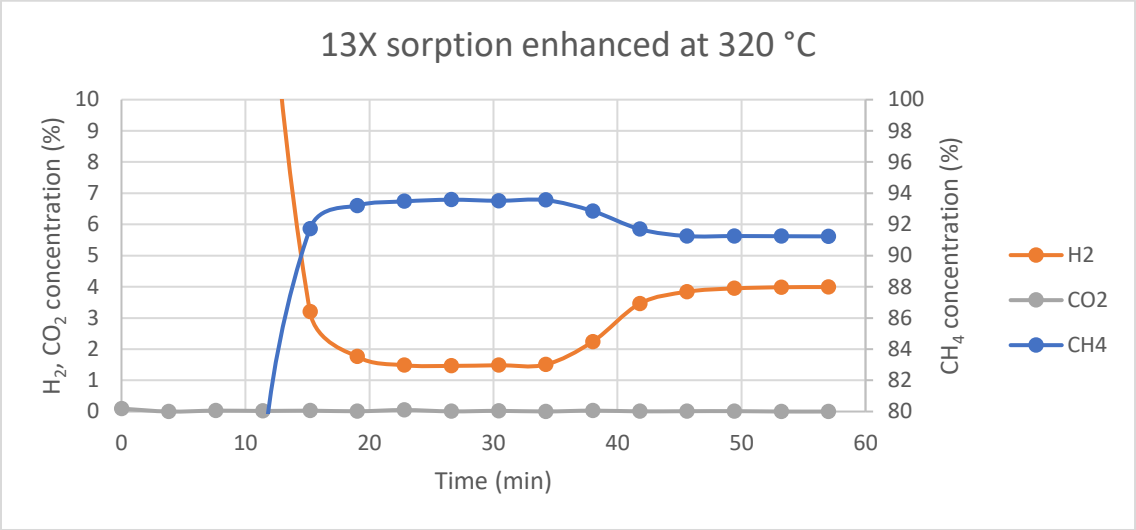

H.1. 1:Sorption enhanced methanation illustrating the breakthrough curve by the GC-measurements. Adsorption condition: 320 °C, atmospheric pressure, total material mass: 8.4 gram, Support = 13X, precursor= Ni-Cit, Impregnation= EIM.

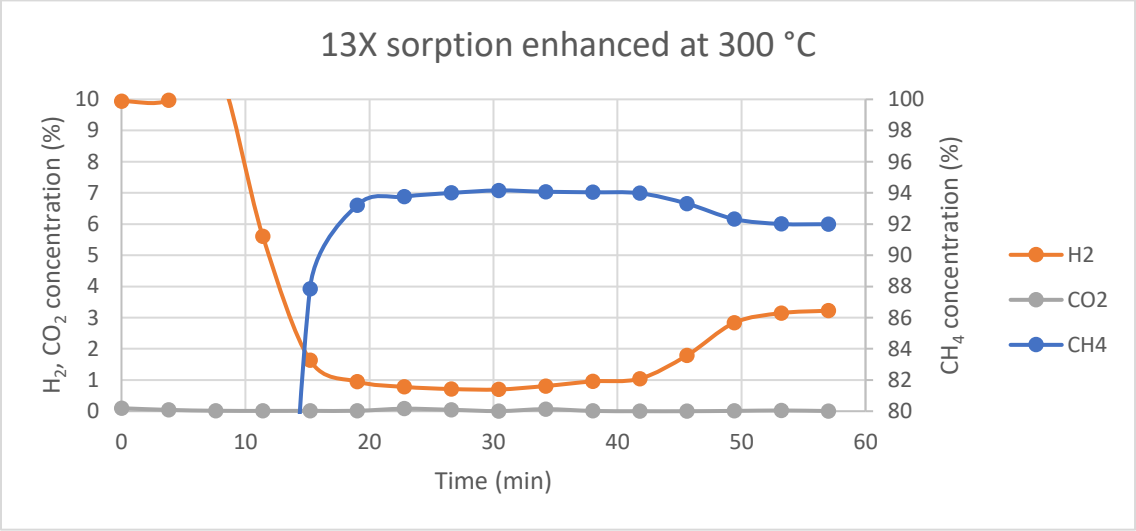

H.1. 2: Sorption enhanced methanation illustrating the breakthrough curve by the GC-measurements. Adsorption condition: 300 °C, atmospheric pressure, total material mass: 8.4 gram, Support = 13X, precursor= Ni-Cit, Impregnation= EIM.

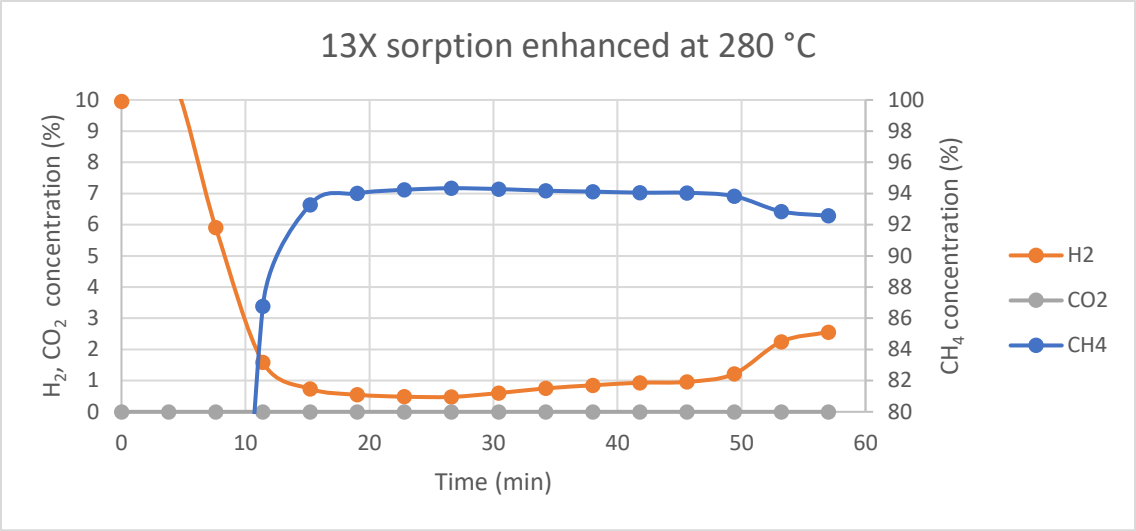

H.1. 3: Sorption enhanced methanation illustrating the breakthrough curve by the GC-measurements. Adsorption condition: 280 °C, atmospheric pressure, total material mass: 8.4 gram, Support = 13X, precursor= Ni-Cit, Impregnation= EIM.

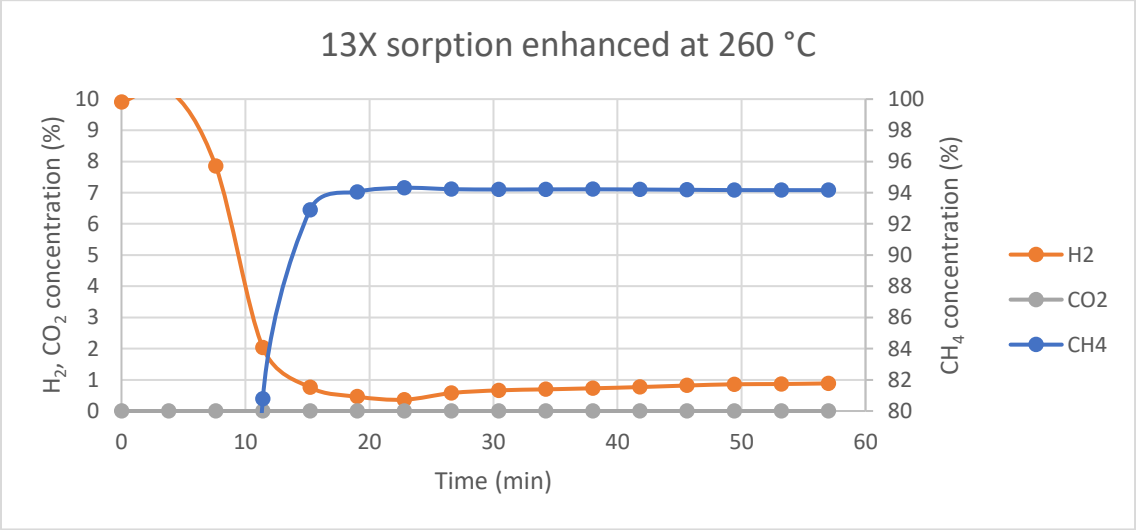

H.1. 4: Sorption enhanced methanation illustrating the breakthrough curve by the GC-measurements. Adsorption condition: 260 °C, atmospheric pressure, total material mass: 8.4 gram, Support = 13X, precursor= Ni-Cit, Impregnation= EIM.

H.2. Zeolite L

All sorption enhancement with the zeolite L show the following:

- An Insignificant level of sorption enhancement is measured after introducing the reaction mixture.
- The CO_2 breakthrough seems to occur later, but it is caused by the CO_2 concentration which is below the lower limit of the GC-measurement.

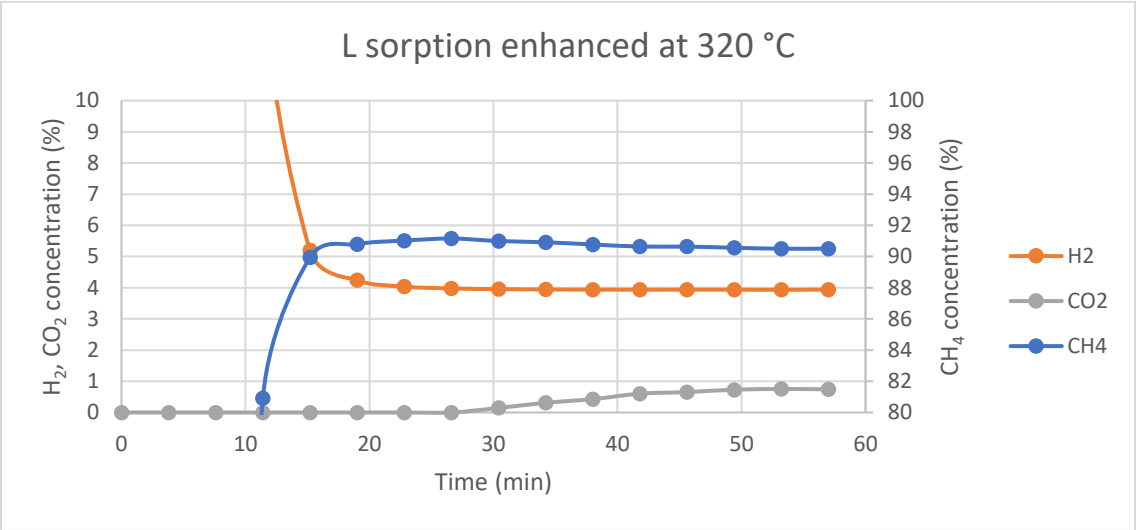

H.2. 1: Sorption enhanced methanation illustrating the breakthrough curve by the GC-measurements. Adsorption condition: 320 °C, atmospheric pressure, total material mass: 8.4 gram, Support = L, precursor= Ni-Cit, Impregnation= EIM.

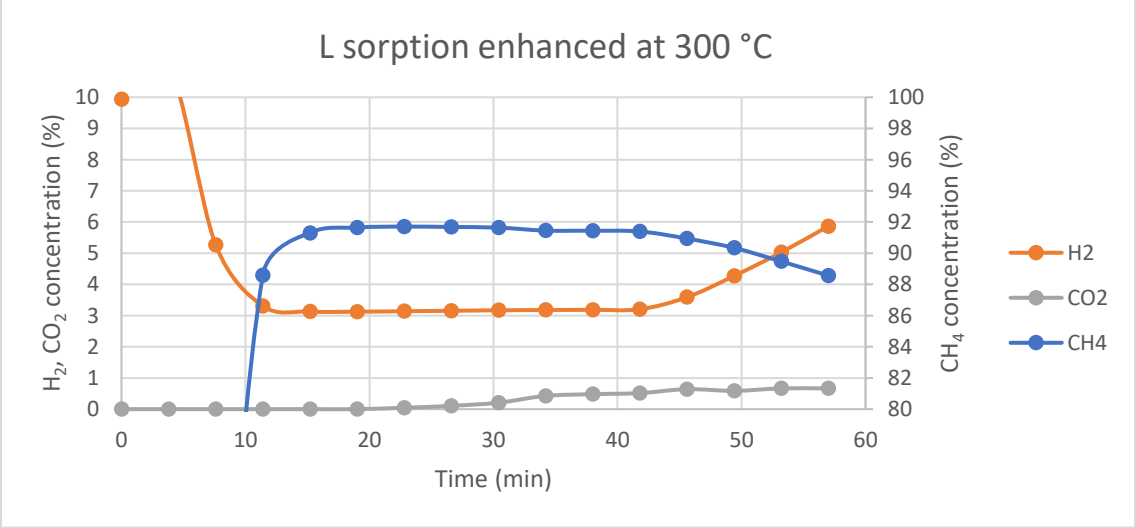

H.2. 2: Sorption enhanced methanation illustrating the breakthrough curve by the GC-measurements. Adsorption condition: 300 °C, atmospheric pressure, total material mass: 8.4 gram, Support = L, precursor= Ni-Cit, Impregnation= EIM.

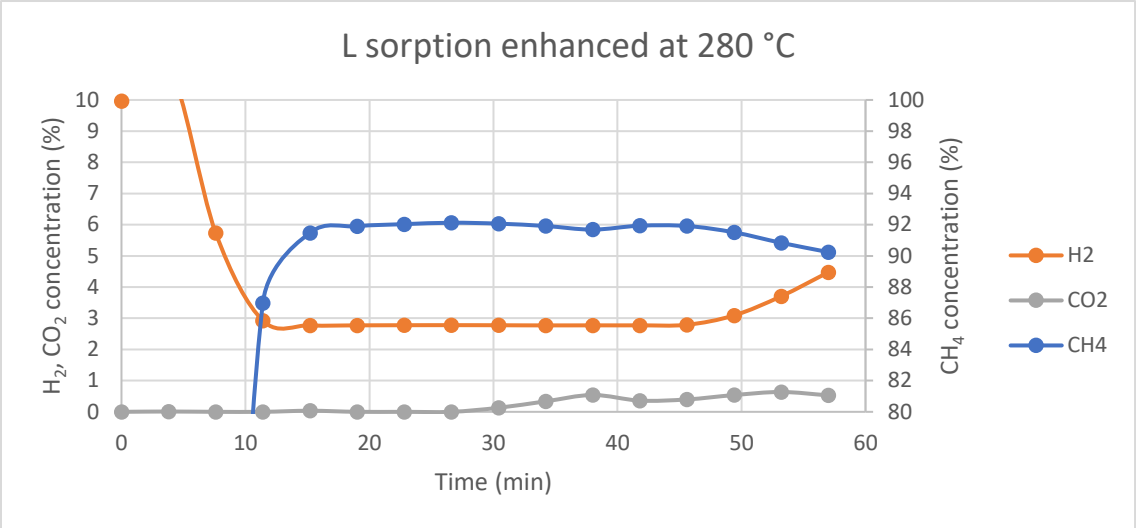

H.2. 3: Sorption enhanced methanation illustrating the breakthrough curve by the GC-measurements. Adsorption condition: 280 °C, atmospheric pressure, total material mass: 8.4 gram, Support = L, precursor= Ni-Cit, Impregnation= EIM.

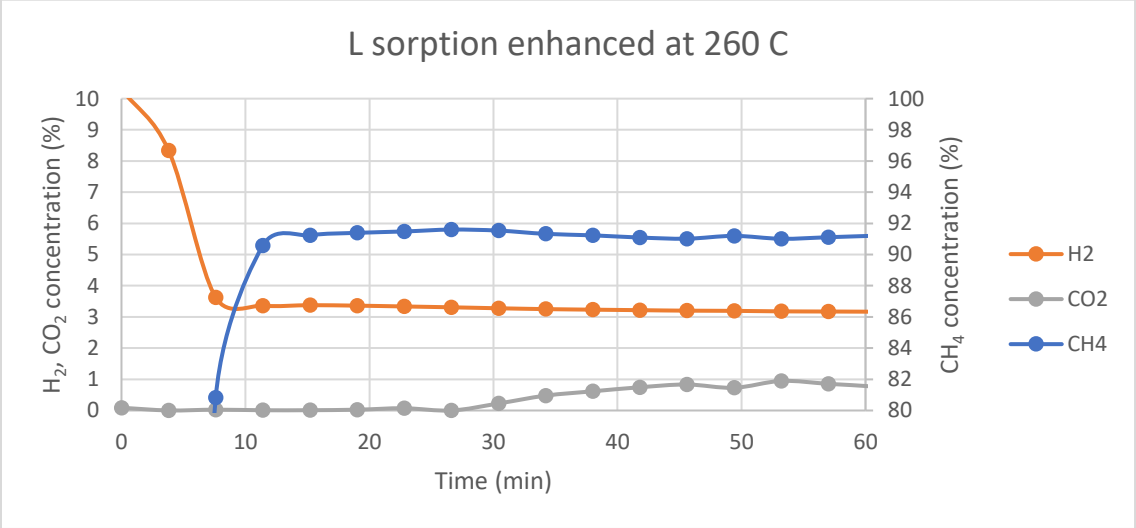

H.2. 4: Sorption enhanced methanation illustrating the breakthrough curve by the GC-measurements. Adsorption condition: 260 °C, atmospheric pressure, total material mass: 8.4 gram, Support = L, precursor= Ni-Cit, Impregnation= EIM.

H.3. Zeolite 5A

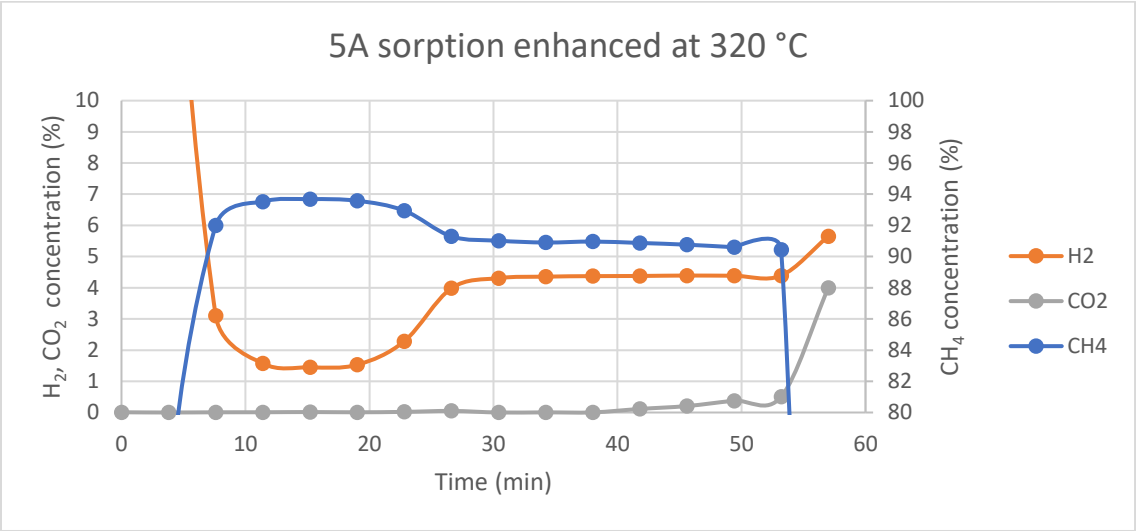

H.3. 1: Sorption enhanced methanation illustrating the breakthrough curve by the GC-measurements. Adsorption condition: 320 °C, atmospheric pressure, total material mass: 8.4 gram, Support = L, precursor= Ni-Cit, Impregnation= EIM.

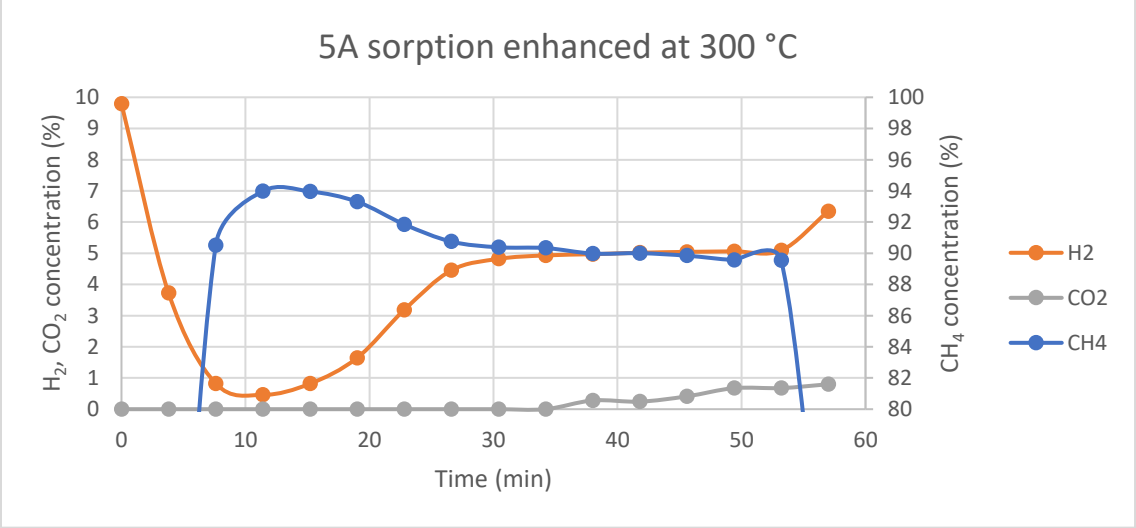

H.3. 2: Sorption enhanced methanation illustrating the breakthrough curve by the GC-measurements. Adsorption condition: 300 °C, atmospheric pressure, total material mass: 8.4 gram, Support = L, precursor= Ni-Cit, Impregnation= EIM.

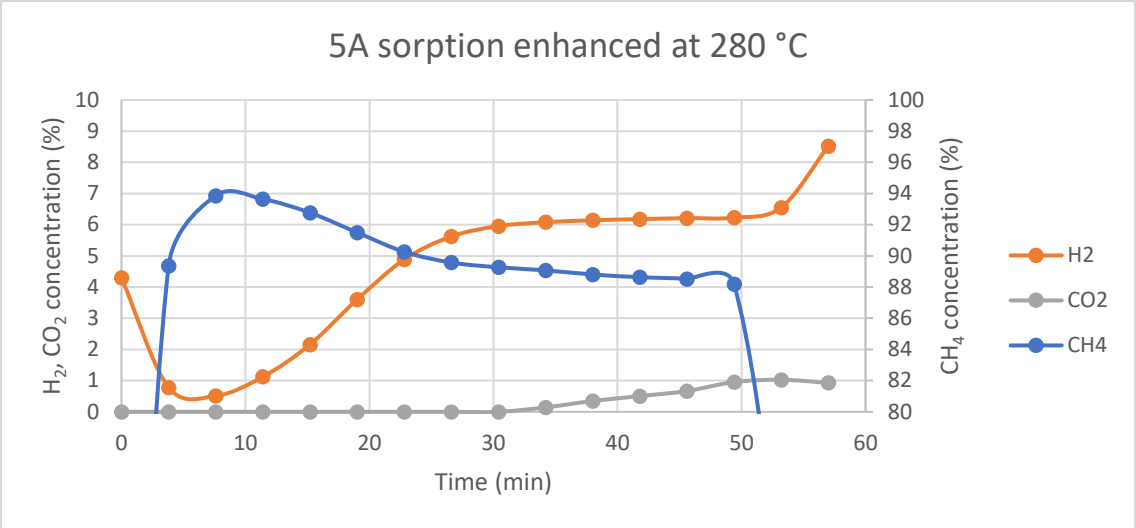

H.3. 3: Sorption enhanced methanation illustrating the breakthrough curve by the GC-measurements. Adsorption condition: 280 °C, atmospheric pressure, total material mass: 8.4 gram, Support = L, precursor= Ni-Cit, Impregnation= EIM.

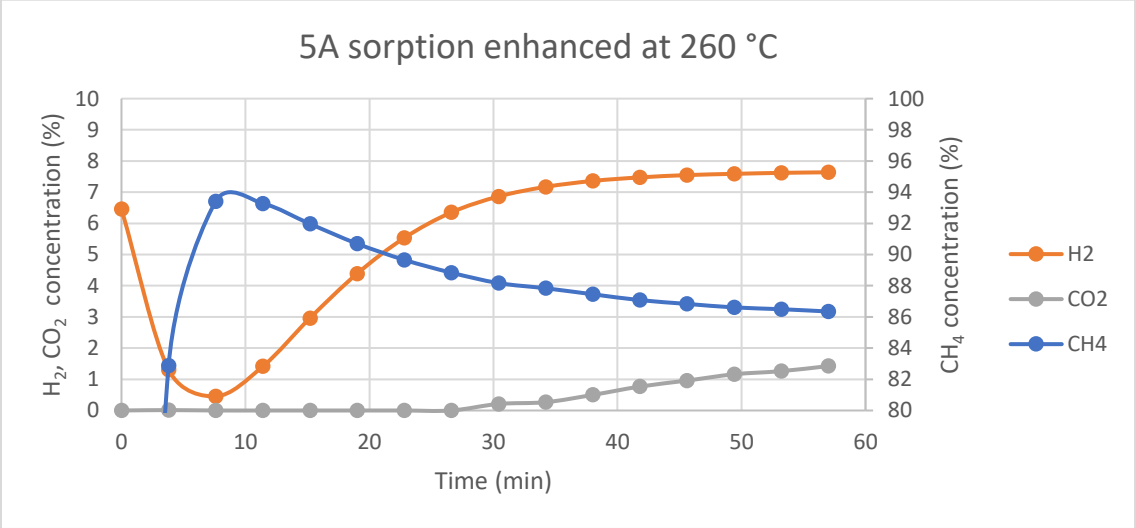

H.3. 4: Sorption enhanced methanation illustrating the breakthrough curve by the GC-measurements. Adsorption condition: 260 °C, atmospheric pressure, total material mass: 8.4 gram, Support = L, precursor= Ni-Cit, Impregnation= EIM.

I. Mass balance

Input GC				
compound	Concentration (Normalized to 100%)	flow (ml/min)	mass flow (g/min)	Mol flow (mol/min)
Hydrogen	10.46	12.0	9.9E-04	5.0E-04
Nitrogen	5.22	6.0	6.9E-03	2.5E-04
Carbon monoxide	0.00	0.0	0.0E+00	0.0E+00
Methane	81.92	94.2	6.2E-02	3.9E-03
Carbon dioxide	2.40	2.8	5.0E-03	1.1E-04
H_2O	-	0.0	0	0

Table I. 1: GC measurement via the bypass of the input flow.

Output GC				
compound	Concentration (Normalized to 100%)	flow (ml/min)	mass flow (g/min)	Mol flow (mol/min)
Hydrogen	3.985	1.78	1.5E-04	7.4E-05
Nitrogen	4.773	6.00	6.9E-03	2.5E-04
Carbon monoxide	0	0.00	0.0E+00	0.0E+00
Methane	91.242	112.30	7.4E-02	4.6E-03
Carbon dioxide	0	0.06	1.0E-04	2.4E-06
H_2O				3.7E-05

Table I. 2: GC-measurement during the activity test of 5%Ni/13X/Cit/EIM at 320 °C.

	In	Out	Absolute difference	Relative difference
C	4.0E-03	4.6E-03	-6E-04	-14%
N	4.9E-04	4.9E-04	0	0%
H	1.6E-02	1.9E-02	-2E-03	-12%
O	2.3E-04	9.2E-03	1E-04	-98%

Table I. 3: The Atomic mass balance with mismatches. The CO_2 concentration is measured near the lower limit of the GC-measurement, creating large errors between the in- and output. The carbon and oxygen balance are affected directly since both atoms are present in the CO_2 molecule. The Mismatch of the hydrogen balance is indirectly caused by the oxygen balance through the H_2O molecule.